OPTIMIZATION OF PEROVSKITE SOLAR CELLS THROUGH INTERFACIAL, ARCHITECTURAL, AND SOLUTION-BASED MODIFICATIONS

A Dissertation
Presented to
The Academic Faculty

by

Giovanni DeLuca

In Partial Fulfillment
of the Requirements for the Degree
of Doctor of Philosophy in the
School of Chemistry & Biochemistry

Georgia Institute of Technology
May 2019

OPTIMIZATION OF PEROVSKITE SOLAR CELLS THROUGH INTERFACIAL, ARCHITECTURAL, AND SOLUTION-BASED MODIFICATIONS

Approved by:

Dr. Elsa Reichmanis, Advisor
School of Chemical and Biomolecular Engineering
Georgia Institute of Technology

Dr. Mostafa El-Sayed
School of Chemistry & Biochemistry
Georgia Institute of Technology

Dr. Angus Wilkinson, Advisor
School of Chemistry & Biochemistry
Georgia Institute of Technology

Dr. Paul H. Wine
School of Chemistry & Biochemistry
Georgia Institute of Technology

Dr. Phillip N. First
School of Physics
Georgia Institute of Technology

Date Approved: November 30, 2018

Посвящается моей Птичке

ACKNOWLEDGEMENTS

Most people don't know this about me, but when I was a teenager I was homeless for 6 months. Every day was a struggle to find a place to sleep and food to eat. Homelessness and hunger were constant themes in my life – even the beginning of my PhD experience consisted of me living in my car. The difficulties and challenges I faced throughout my life would have incapacitated me if it weren't for so many wonderful people. If I were to thank every individual that has helped me along the way, I would fill an entire chapter of this dissertation, so to that I leave you with this:

If you ever gave me a place to stay for the night, if you ever gave me food when I was hungry, if you ever gave me your friendship, if you ever offered me encouraging words, if you ever gave me your support even though the odds were so greatly stacked against me, know that I still think of those moments every day, and I am truly grateful. Know that you were a catalyst for me paying it forward every chance I get with young individuals fighting an uphill battle. Know that I will mentor children living in poverty and plant a seed that they too have the potential to reach heights that they never thought possible. Know that your kind deeds will continue to give for many generations to come.

.

TABLE OF CONTENTS

ACKNOWLEDGEMENTS **iv**

LIST OF TABLES **vii**

LIST OF FIGURES **viii**

LIST OF SYMBOLS AND ABBREVIATIONS **xii**

SUMMARY **xiv**

CHAPTER 1. INTRODUCTION **1**
1.1 Energy and society **1**
1.2 Solar cells **1**
1.2.1 Solar cell operation 2
1.2.2 Different technologies 4
1.3 Perovskite solar cells **6**
1.4 Weaknesses of perovskite solar cells **12**
1.5 Thesis organization **18**

CHAPTER 2. SOLVENT VAPOR ANNEALING OF ORIENTED PbI_2 FILMS FOR IMPROVED CRYSTALLIZATION OF PEROVSKITE FILMS FOR AIR-STABLE SOLAR CELLS **20**
2.1 Introduction **20**
2.2 Experimental section **22**
2.2.1 Materials and reagents 22
2.2.2 $CH_3NH_3PbI_3$ film fabrication 22
2.2.3 Device fabrication 23
2.2.4 Characterization 24
2.3 Results and discussion **25**
2.3.1 Perovskite film characterization 25
2.3.2 Photovoltaic performance of perovskite solar cells 35
2.4 Conclusion **41**

CHAPTER 3. MODIFYING PEROVSKITE FILMS WITH POLYVINYLPYRROLIDONE FOR AMBIENT-AIR-STABLE HIGHLY BENDABLE SOLAR CELLS **42**
3.1 Introduction **42**
3.2 Experimental section **44**
3.2.1 Materials and reagents 44
3.2.2 Perovskite device fabrication 44
3.2.3 Characterization 45
3.3 Results and discussion **46**
3.3.1 PVP-Perovskite film formation 46
3.3.2 Device fabrication and characterization 59
3.3.3 Flexibility and bendability testing 64

3.4 Conclusion 68

CHAPTER 4. TRANSPARENT QUASI INTERDIGITATED ELECTRODES FOR PEROVSKITE BACK-CONTACT SOLAR CELLS 70
4.1 Introduction 70
4.2 Experimental section 72
4.2.1 Materials and reagents 72
4.2.2 Transparent quasi-interdigitated electrode fabrication 72
4.2.3 Deposition of CuSCN layer 73
4.2.4 Device fabrication 74
4.2.5 Characterization 75
4.2.6 Computational modelling 76
4.3 Results and discussion 78
4.3.1 ITO characterization 78
4.3.2 Perovskite characterization 84
4.3.3 Photovoltaic performance of transparent back-contact perovskite solar cells 87
4.4 Conclusion 95

CHAPTER 5. DOPED-ITO FOR PEROVSKITE SOLAR CELLS 96
5.1 Introduction 96
5.2 Experimental section 97
5.2.1 Doped ITO preparation 97
5.2.2 Characterization 98
5.3 Results and discussion 99
5.3.1 ITO characterization 99
5.4 Conclusion and future direction 102
5.4.1 Future direction 103

CHAPTER 6. CONCLUDING REMARKS AND FUTURE WORK 104
6.1 Future direction 107
6.1.1 Introduction 107
6.1.2 Experimental section 108
6.1.3 Results and discussion 109
6.1.4 Conclusion and future direction 115

REFERENCES 116

LIST OF TABLES

Table 2-1. Atomic percentages in the perovskite film. 34
Table 2-2. Parameters of best devices..... 36
Table 3-1. Bandgap values calculated from UV-Vis and ultraviolet photoelectron spectroscopy data. 53
Table 3-2. The optimized Photovoltaic performance parameters of the devices under standard AM 1.5G illumination (100 mW cm−2). 63
Table 3-3. Photovoltaic performance parameters of flexible devices before bending and after bending 1000 times under standard AM 1.5G illumination (100 mW cm−2). 68
Table 4-1. Physical parameters used in simulations. 77
Table 4-2. PESA data for five independent ITO thin annealed for 3 min at 300 °C. 79
Table 4-3. UV-Vis-NIR transmission data for the various layers throughout the device and ITO thin film on glass. 83
Table 4-4. Major photovoltaic parameters of back-contact PSCs with t-QIDEs.[a] 89
Table 4-5. Simulated PCE and AVT data for t-QIDEs-based back-contact PSCs. 93
Table 5-1. Ionization potential of the undoped and doped ITO. 100
Table 5-2. Lattice parameter for the ITO and doped ITO phase. 101
Table 6-1. Variables to the recipe for this work, including varying loading times. 108

LIST OF FIGURES

Figure 1-1. Structure of single junction n-i-p (left) and p-i-n (right) solar cells. 3
Figure 1-2. The ideal short circuit flow of electrons and holes in a n-i-p solar cell. 3
Figure 1-3. The band diagram illustrating the electron and hole transport within a photovoltaic device. 4
Figure 1-4. Best Research-Cell Efficiencies (republished with permission).[16] 6
Figure 1-5. Crystal structure of perovskite with the chemical formula AMX_3 (republished with permission).[18] 7
Figure 1-6. Fabrication techniques used for the perovskite crystal in perovskite solar cells (republished with permission).[24] 9
Figure 1-7. One-step (top) and two-step (bottom) spin-coating technique (republished with permission).[25] 9
Figure 1-8. Mesoscopic nano-structured (left) and planar structured (right) perovskite solar cells (republished with permission).[26] 11
Figure 1-9. Energy diagram of a perovskite solar cell fabricated in Chapter 6 of this work (republished with permission).[27] 11
Figure 1-10. Perovskite degradation with time (republished with permission).[29] 13
Figure 1-11. Degradation rate at varying relative humidity (republished with permission).[29] 13
Figure 1-12. Energy misalignment and alignment with TiO_2 and SnO_2 respectively (republished with permission).[31] 15
Figure 1-13. Demonstration of significant hysteresis effect improvement using SnO_2 compared to TiO_2 (republished with permission).[31] 15
Figure 1-14. Alignment of the modified polymer hole transport layer with the perovskite valence band (republished with permission).[32] 16
Figure 1-15. Alignment if TiO_2 with the adjacent layers by modifying ITO and TiO_2 (republished with permission).[37] 17
Figure 1-16. FTO XRD patterns before (below) and after (above) annealing (republished with permission).[40, 41] 18
Figure 2-1. Schematic diagram for the preparation of the three types of PbI2 films and corresponding optical photographs. 26
Figure 2-2. Surface (left column) and Cross-sectional (right column) FE-SEM image of PbI2 films (top row) sample 1(a)(b), sample 2(c)(d) and sample 3(e)(f). 27
Figure 2-3. Pore size distribution for d-PbI2 (a), a-PbI2 (b) and m-PbI2 (c). 28
Figure 2-4. Surface (left column) and Cross-sectional (right column) FE-SEM image of perovskite films sample 1(a)(b), sample 2(c)(d) and sample 3(e)(f). 29
Figure 2-5. Two-dimensional WAXD pattern (covered from $2\theta=5°$ to $2\theta=20°$) of PbI2 from sample 1 (a), sample 2 (b), sample 3 (c) and corresponding perovskite films (d-f). 30
Figure 2-6. One dimensional XRD spectra of PbI2 films and corresponding perovskite films integrated from Two WAXD pattern (a)(b), measured from One WAXD pattern(c)(d). 32
Figure 2-7. UV-visible absorption spectra of PbI2 films (a) and corresponding perovskite films (b) on FTO glass. 33

Figure 2-8. (a) Photoluminescence of perovskite samples on FTO glass. (b) TRPL data for perovskite sample. 35
Figure 2-9. J-V curves under both (black line) forward and (red line) reverse scans for best devices. (a) sample 1 (b) sample 2 (c) sample 3. 38
Figure 2-10. AFM images of perovskite films from sample 1 (a), 2(b) and 3 (c). 39
Figure 2-11. (a) IPCE spectra of the devices with different perovskite films. (b) The steady-state current measured at the maximum power point for sample 1 (0.68 V), sample 2 (0.73 V) and sample 3 (0.82 V). 40
Figure 2-12. Statistical data for efficiency (a), Voc (b), Jsc (c) and FF (d) of three types of devices. 41
Figure 3-1. Surface and Cross-sectional FE-SEM image of perovskite films without PVP (a, i) and with PVP at 4 wt% (b, j), 8 wt% (c, k), and 12 wt% (d, l) concentrations. Particle size and distribution for corresponding images (e-h). 49
Figure 3-2. AFM images of 0 wt% (a), 4 wt% PVP (b), 8 wt% (c) and 12 wt% (d) PVP-perovskite films. 50
Figure 3-3. (a) XRD patterns of PVP-perovskite films. The diffraction peaks originating from the perovskite phase, non-perovskite phase, unreacted PbI2 and the FTO substrate are marked by α, δ, ω, and * respectively. (b) FT-IR spectra of PVP-perovskite films, and pure PVP (green); (c) UV-Vis absorbance data of 0 PVP-perovskite films; and (d) Tauc plots of 0 wt% (black), 4 wt% (red), 8 wt% (blue), and 12 wt% (magenta) PVP-perovskite films. 51
Figure 3-4. Valence band spectra of perovskite films with 0 wt% (black), 4 wt% (red), 8 wt% (blue) and 12 wt% (magenta) PVP on silica wafer. 54
Figure 3-5. Survey XPS spectra of 0 wt% (black), 4 wt% (red), 8 wt% (blue), and 12 wt% (magenta) PVP-Perovskite samples. 55
Figure 3-6. Core-level XPS spectra for 0 wt% (black), 4 wt% (red), 8 wt% (blue), and 12 wt% (magenta) PVP-perovskite films: (a) I3d, (b) O1s, (c) N1s, (d) C1s, (e) Pb4f and (f) Br3d. (g) Schematics of the variation of perovskite crystals with PVP concentration increasing. 56
Figure 3-7. (a) Photoluminescence of PVP-Perovskite samples on the glass. (b) Time Resolved Photoluminescence (TRPL) data for 0 wt% (black), 4 wt% (red), 8 wt% (blue), and 12 wt% (magenta) PVP- Perovskite samples. 58
Figure 3-8. (a) Schematic energy level diagrams of the SnO2 nanoparticles, 0 wt%, 4 wt%, 8 wt%, 12 wt% PVP doped perovskite and spiro-MeOTAD; (b) J−V curves of the typical devices under AM 1.5G illumination. (c) Corresponding EQE responses (left axis) and integrated current densities (right axis) of the devices containing the perovskite films with and without PVP. (d) Normalized efficiency as a factor of time; (e) Photograph of perovskite solar cell stability with varying concentrations of PVP in ambient conditions. From left to right 0 wt%, 4 wt%, 8 wt%, and 12 wt% PVP-perovskite devices. 60
Figure 3-9. Statistical data 0 wt% (black), 4 wt% (red), 8 wt% (blue), and 12 wt% (magenta) for (a) Voc, (b) Jsc, (c) FF, and (d) PCE. 63
Figure 3-10. (a-d) Top-view SEM images of (a,b) 0 wt% PVP and (c.d) 8wt % PVP-perovskite grown on PET/ITO before and after 200 bending times with bending radius of 0.5 cm; the inset shows a photograph of the bending tests. (e)(f) Steady-state PL spectra of the corresponding pristine and PVP containing perovskite films. 65

Figure 3-11. (a) Photograph of the bending tests for flexible devices; (b) Mechanical stability of corresponding flexible devices; (c) J−V curves of 0 wt% and 8 wt% PVP-perovskite flexible devices under AM 1.5G illumination at the initial stage. 67
Figure 4-1. (a) The structure of a QIDEs. (b) Light transmission, absorption and reflection in QIDEs with Al/NiCo electrodes (left) or transparent electrodes (right). 72
Figure 4-2. Comparison of the UV-Vis-NIR transmission spectra of ITO thin films on glass substrates annealed at 300 °C for 0 (black), 1 (red) or 3 min (blue) with the solar spectrum (green). 79
Figure 4-3. XRD patterns of an as-deposited ITO thin film on glass (black), and ITO thin films annealed at 300 °C for 1 (red) or 3 min (blue). 80
Figure 4-4. Visible light microscope image of ITO on Al2O3 fingers after polymer resist lift-off. Removal of the photoresist did not cause damage to the ITO fingers. 81
Figure 4-5. (a) Photograph of t-QIDEs before (left) and after annealing at 300 °C (right). (b) UV-Vis-NIR transmission spectra of the t-QIDEs at various stages of fabrication, and for QIDEs with a gold top electrode. 82
Figure 4-6. UV-Vis-NIR spectroscopy measurements in transmission and reflection modes for a CuSCN-modified t-QIDEs measured from the front (electrode) and rear (glass) side. 84
Figure 4-7. PESA measurement of the CuSCN and perovskite thin films deposited on t-QIDEs. 85
Figure 4-8. Band diagram for an n-i-p lateral PSC device with a t-QIDEs employing TiO_2 and CuSCN as charge selective layers. Valence band edge for perovskite and CuSCN as well as the work function of ITO were derived from PESA measurements (Table 4.2 and Figure 4.7). 85
Figure 4-9. (a) Cross-sectional SEM image of the back-contact PSC based on the $Cs_{0.05}FA_{0.79}MA_{0.16}PbI_{2.49}Br_{0.51}$ photoabsorber and t-QIDE, (b) high magnification cross-sectional SEM image of the device (area enclosed with red rectangle in Figure 4.9a), (c) back-scattered SEM cross-sectional image of a finger of the device (area enclosed with red rectangle in Figure 4.9a). 86
Figure 4-10. High magnification back-scattered electron cross sectional image of a back-contact PSC with t-QIDEs showing the thickness of its functional layers. 87
Figure 4-11. (a) J–V characteristics (scan rate 0.2 V s−1) of a BC-PSC based on the $Cs_{0.05}FA_{0.79}MA_{0.16}PbI_{2.49}Br_{0.51}$ light-absorber and a t-QIDE measured under 1 sun illumination from the front (perovskite) side and rear (glass) side, and in the dark. (b) Evolution of photocurrent and power density of the same BC-PSC at maximum power point under 1 sun irradiation from the rear side. 88
Figure 4-12. J-V curves of the BC-PSC devices with CuSCN (red and blue) and without CuSCN (pink and purple) when illuminated from the glass (rear) or perovskite (front) side of the device. Note the Voc, Jsc and FF of the device made with CuSCN are lower than the values reported for the champion device as they were made under non-optimized conditions. However, for comparison the device without CuSCN was made under the same conditions and originated from the same ITO batch. 90
Figure 4-13. Simulated performance of a BC-PSC under front and rear illumination. (a) PCS and AVT as a function of perovskite thickness (the perovskite thickness cannot be below the thickness of the back-contact electrode, viz. 250 nm). (b) External quantum efficiency (EQE) at the optimum thickness of the perovskite layer (750 and 650 nm for

front- and rear-illumination, respectively). (c) Charge generation rate of the perovskite layer in between the two back-contact electrodes. The generation rate is averaged over the thickness of the perovskite and leveled to the total thickness of the electrodes. The apparent interference fringes are due to optical modes created by the multi layered structure evolved. Simulations were based on AM 1.5 spectrum and a 500 nm minority-carrier diffusion length for the perovskite. 92
Figure 4-14. Simulated power-conversion-efficiency (PCE) map of the t-QIDEs-based back-contact PSCs as a function of back-contact width and gap size between the two back-contacts for (a) infinitely long and (b) 500 nm minority carrier diffusion length within the perovskite layer. The maps were constructed by simulating a pitch size of 0.25, 0.5, 1, 2, 3 and 5 μm, while simultaneously varying the contact width of 0.25, 0.5, 1 and 2 μm. The data between these input parameter values were calculated by linear interpolation. Note that the origin point of these two plots is at (0.25, 0.25). 95
Figure 5-1. Diffraction pattern of undoped ITO and Ni-doped ITO..... 100
Figure 5-2. Transmittance of glass, undoped ITO, and Ni doped ITO..... 101
Figure 5-3. Hole-transport-layer-free device (republished with permission).[180] 102
Figure 5-4. Interfacial hole transfer dynamics. Schematic illustrations of hole transfer at the ITO/$MAPbI_3$ and ITO/F4TCNQ-doped $MAPbI_3$ interface (republished with permission).[180]..... 103
Figure 6-1. UV-visible absorption spectra of perovskite films on FTO glass made with varying loading times (30s, 60s, and 90s) of the MAI/IPA precursor solution. 110
Figure 6-2. Diffraction pattern of perovskite films on FTO glass made with varying loading times (30s, 60s, and 90s) of the MAI/IPA precursor solution. 111
Figure 6-3. Photoluminescence study of perovskite films on FTO glass made with varying loading times (30s, 60s, and 90s) of the MAI/IPA precursor solution. 112
Figure 6-4. Photograph of perovskite films on FTO with varying amounts of additive in the MAI/IPA precursor solution. 112
Figure 6-5 . Diffraction pattern of perovskite films on FTO with varying amounts of additive and a 90 second load time. (a) 0 μL DMF, (a) 0 μL DMF, (a) 0 μL DMF, and (a) 0 μL DMF. Black 0 μL 1M HCl, Red 10 μL 1M HCl, Blue 20 μL 1M HCl, and Green 50 μL 1M HCl..... 113
Figure 6-6. UV-Vis absorption spectra of perovskite films on FTO with varying amounts of additive and a 90 second load time. (a) 0 μL DMF, (a) 0 μL DMF, (a) 0 μL DMF, and (a) 0 μL DMF. Green 0 μL 1M HCl, Blue 10 μL 1M HCl, Red 20 μL 1M HCl, and Black 50 μL 1M HCl..... 114

LIST OF SYMBOLS AND ABBREVIATIONS

AFM	Atomic force microscopy
AM 1.5 G	Air mass of 1.5 atmosphere and solar zenith angel of 48.2 °
Ag	Silver
Au	Gold
CB	Conduction band
C60	Fullerene
DMF	N,N-Dimethylformamide
DMSO	Dimethyl sulfoxide
EA	Electron affinity
EL	Electroluminescent
E_g	Bandgap
EQE	External quantum efficiency
ETL	Electron transport layer
F4TCNQ	2,3,5,6-Tetrafluoro-7,7,8,8-tetracyanoquinodimethane
FF	Fill factor
FTO	Fluorine-doped tin oxide
HOMO	Highest occupied molecular orbital
HTL	Hole transport layer
HTM	Hole transporting material
IE	Ionization Energy
ITO	Indium tin oxide
I_{SC}	Short circuit current, V=0
IV-curve	Current voltage curve
J_{SC}	Short circuit density, V=0
LUMO	Lowest unoccupied molecular orbital
M	Molarity
MAI	Methylammonium iodide
MAPbI3	Methylammonium lead iodide
MPP	Maximum power point
P3HT	Poly(3-hexylthiophene-2,5-diyl)
PCBM	[6,6]-Phenyl-C61-Butyric-acid-Methyl ester
PCE	Power conversion efficiency
PEDOT:PSS	Poly(ethylenedioxythiophene):poly(styrene sulfonic acid)
PES	Photon emission spectroscopy
PL	Photoluminescence
PSC	Perovskite solar cell
PV	Photovoltaic

RMS	Root mean square
R_S	Series resistance
R_{SH}	Shunt resistance
SAM	Self-assembled monolayer
SEM	Scanning electron microscopy
spiro-MeOTAD	2,2',7,7'-Tetrakis[N,N-di(4-methoxyphenyl)amino]-9,9'-spirobifluorene
TEM	Transmission electron microscope
TiO_2	Titanium dioxide
TRPL	Time-resolved photoluminescence
UPS	Ultraviolet photoelectron spectroscopy
VB	Valence band
V_{OC}	Open circuit voltage, I=0
WF	Work function
XPS	X-ray photoelectron spectroscopy
ZnO	Zinc Oxide

SUMMARY

The photovoltaic performance of perovskite solar cells is extremely dependent on the crystallization, morphology and interfacial characteristics of the thin films utilized in the device, which are affected by a multitude of factors. In this work, I explore routes to optimize device performance through optimizing the perovskite crystallization and morphology *via* doping and processing, tailoring the architecture, or optimizing interfaces in the perovskite devices. In addition, one major drawback that prevents the large-scale practical implementation of perovskites is their susceptibility to performance degradation in humid environments. This work will also explore the improvement made to moisture stability. Lastly, this work will explore the various applications of the modified perovskite devices.

Chapter 2 discusses work where we demonstrate a simple approach to form a microporous PbI_2 film, with subsequent conversion to a compact, highly crystalline perovskite film. The PbI_2 and corresponding perovskite films were further probed by two-dimensional X-ray diffraction. The resultant perovskite exhibited improved photovoltaic performance under ambient conditions with about 50% humidity. The PbI_2 microporous structure was formed by exchanging residual DMSO with DMF vapor in the PbI_2 film, which facilitated contact with the methylammonium iodide (MAI) solution. The process resulted in the formation of compact, smooth, pinhole-free perovskite films having no residual PbI_2. Solar cells fabricated using this methodology exhibited power conversion efficiencies over 16% with negligible photocurrent hysteresis.

Chapter 3 discusses work where we achieved uniform, stable perovskite films within a polyvinylpyrrolidone (PVP) polymer frame *via* mild solution processing in ambient air with over 60% relative humidity. In addition to facilitating film formation, the hydrophobic PVP served to protect the perovskite grains from atmospheric moisture. Use of PVP, coupled with optimization of the deposition parameters, provided for compact, smooth, pinhole-free perovskite films that when incorporated into a photovoltaic device exhibited highly reproducible efficiencies in the range of up to 17%. In the absence of encapsulation, the devices exhibited stable performance characteristics during exposure to humid ambient air for 600 hours. Furthermore, on flexible substrates, the 8 wt% PVP-perovskite samples provided for device efficiencies of *ca.* 15%. The devices retained *ca.* 73% of their efficiency after bending 1000 times with a bending radius of 0.5 cm.

Transparent quasi-interdigitated electrodes (t-QIDEs) were produced by replacing the opaque components of existing QIDEs with indium tin oxide (ITO). Chapter 4 discusses our work where we demonstrate t-QIDEs application in the first semi-transparent back-contact perovskite solar cell. A device with a V_{OC} of 0.88 V and a J_{SC} of 5.6 mA cm^{-2} produced a modest 1.7% efficiency. The use of ITO allows for illumination of the device from front- and rear-sides, resembling a bifacial solar cell, both of which yield comparable efficiencies. Coupled optoelectronic simulations reveal this architecture may achieve power conversion efficiencies of up to 11.5%, and 13.3% when illuminated from front- and rear-side, respectively, using a realistic quality of perovskite material.

Chapter 5 explores the work function tunability of the transparent electrode, indium-tin-oxide (ITO), used in perovskite solar cells. In this work, ITO with resistances ranging from 9-19 Ω square^{-1}, and transmittances greater than 80% in the visible region were produced. Through doping, the work function was tuned up to 5.56 eV, to align well with the perovskite valence band. Doping with nickel demonstrated no change to the transmittance in the visible region, however there was a significant improvement to the transmittance in the IR region. This chapter discusses the future directions of this work in the context of perovskite solar cells.

Lastly, in an attempt to produce large area devices, a modified two-step procedure currently being optimized is discussed. This work, discussed in Chapter 6, currently demonstrates the importance of the loading time of the MAI/IPA precursor solution. Max absorption and highest conversion to the perovskite crystal was observed for the 90 second loading time. Using the 90 second loading time to explore the additive effects, the film with the best conversion from the PbI_2 film to perovskite film and highest absorption was the solution that employed 10 µL of DMF and 50 µL of 1M HCl. The films did not require a post-annealing step or an anti-solvent step, which is ideal for large-scale development.

CHAPTER 1. INTRODUCTION

1.1 Energy and society

With the growing population and improved standard-of-living comes an increased need for energy, specifically in the form of electricity.[1] However, the complex infrastructure, imperfect markets and dependence on fossil fuel associated with grid power create many problems.[1-8] Additionally, dependence on grid power fails to provide power for over a billion individuals, whether due to location, natural disasters, financial reasons, etc.[6,9] Of all the reasons to move away from grid power as currently provided, the number one driver is its effect on our planet from the retrieval and usage of fossil fuels.[3-5]

Any alternative technology will need to alleviate all these concerns, while at the same time being a safe, grid-independent replacement. Solar energy is one very attractive option. The energy that is naturally available from the sun is 35,000 times greater than the world energy consumption per year. The Sun delivers 1.2×10^5 TW of power onto the Earth, surpassing any other energy source by capacity and availability.[10]

1.2 Solar cells

Harnessing the sun's energy represents a simple and elegant alternative to fossil fuels. This can be made possible by using solar cells, which can convert solar energy into electrical energy. Solar cells do not require moving parts and they can alleviate issues associated with noise and pollution, making them clean, reliable and long-lasting sources of energy.

1.2.1 Solar cell operation

The basic structures of the solar cells used in this work are shown in Figure 1.1. As shown in Figure 1.2a, photons enter the solar cell through the transparent conducting oxide (TCO) and make their way to the absorption layer, generating an electron/hole pair.[11] However, the electron/hole pair will only be generated provided that the incident photon has an energy greater than the band gap of the absorption layer. The pair separates, and the resultant charge carriers are collected by films strategically chosen based upon their electronic structure. Specifically, the carriers are separated by the action of the electric field existing at the p-n junction. However, if the carrier recombines, then the electron/hole pair is lost and no current or power will be generated. Figure 1.2b demonstrates the electrons being collected at the n-doped film, and the holes collected at the p-doped film, which for the nature of this work will be called the electron transport layer (ETL) and hole transport layer (HTL), respectively. Figure 1.2c goes on to show that the collected carriers give rise to the current in the external circuit from the electron passing through the load. The band diagram in Fig. 1.3 illustrates the electron and hole transport within the device. During this process, photons are absorbed by the active layer, and the generated excitons dissociate to produce free charges. The work function difference between the electrodes drives the holes along the valence band of the active layer, to the anode. On the other hand, electrons from the conduction band are transported towards the cathode. The ELT and HTL can act as a hole and electron blocking layer respectively, when their bandgap is a large enough (exaggerated in Figure 1.3), which discourages recombination.

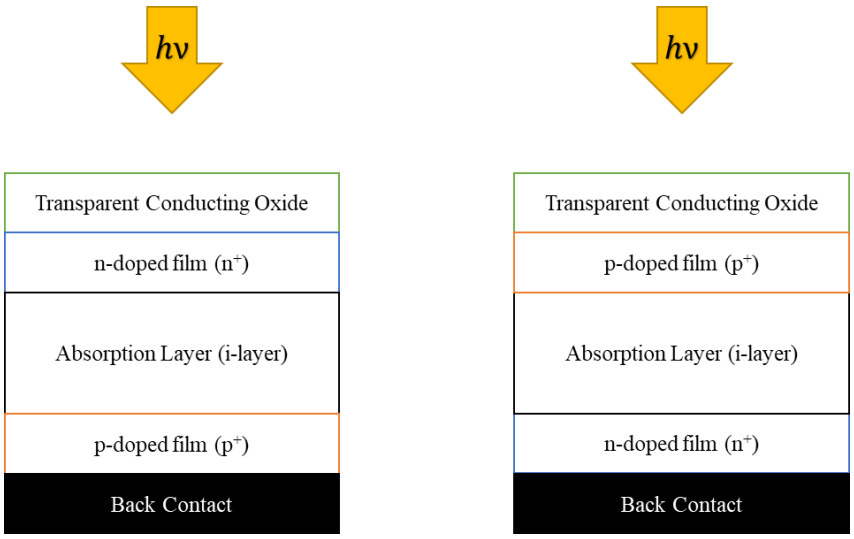

Figure 1-1. Structure of single junction n-i-p (left) and p-i-n (right) solar cells.

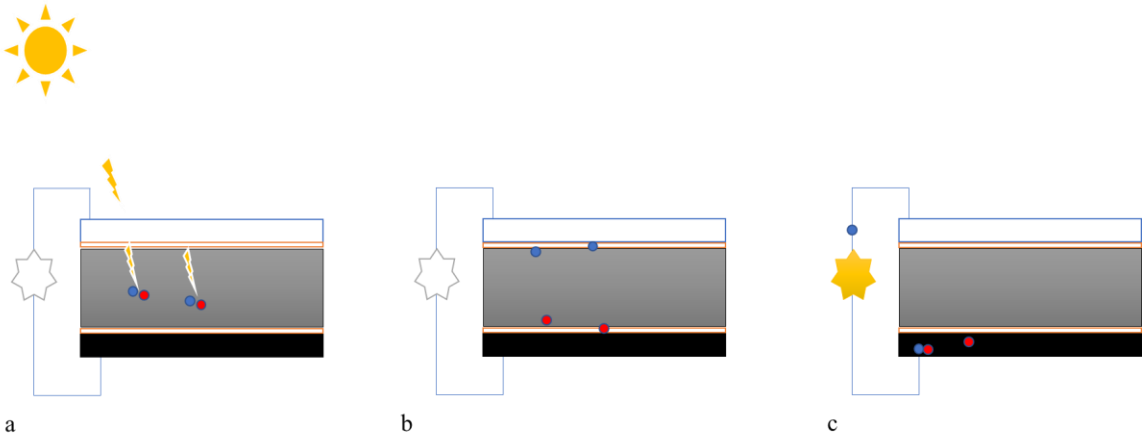

Figure 1-2. The ideal short circuit flow of electrons and holes in a n-i-p solar cell.

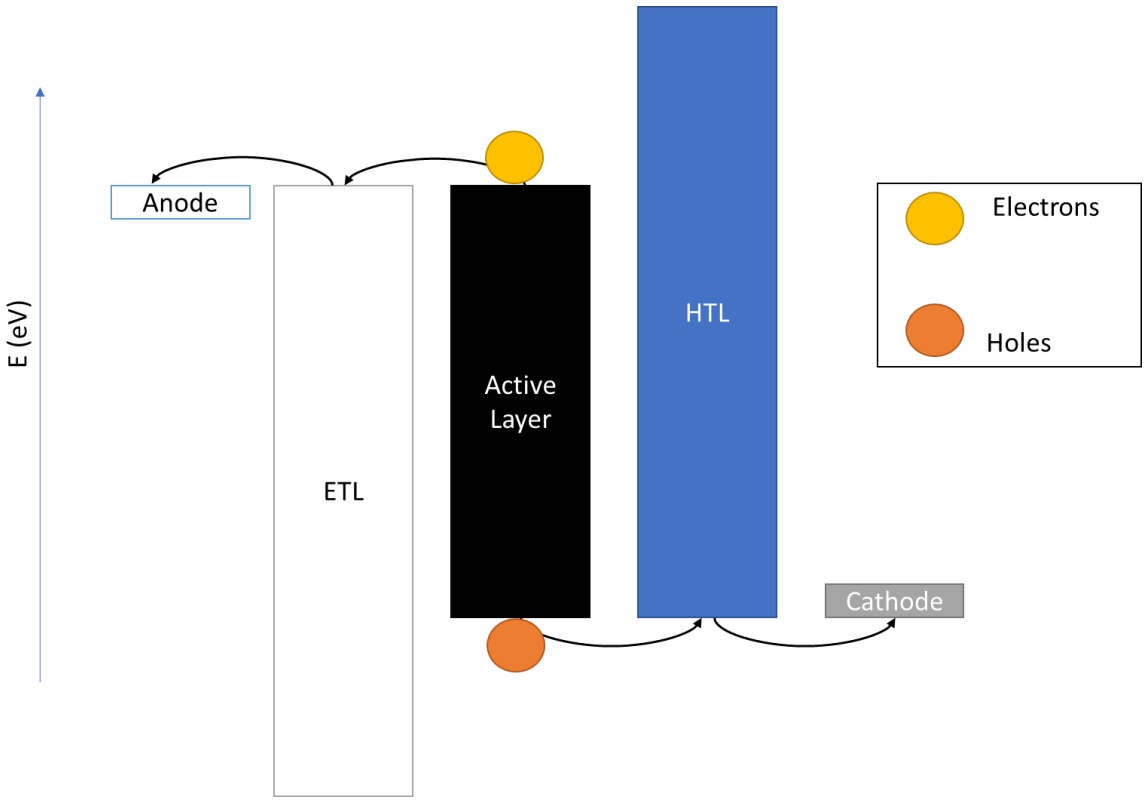

Figure 1-3. The band diagram illustrating the electron and hole transport within a photovoltaic device.

1.2.2 Different technologies

A variety of materials and processes can potentially satisfy the requirements for photovoltaic energy conversion. Among the different photovoltaic technologies, the industry leader is crystalline silicon and will continue being so for the foreseeable future. However, silicon's record efficiency has increased only marginally, from 25.0% to 25.6%, in the past 15 years; and is approaching its theoretical efficiency potential.[12] Polman *et. al.* reported that the global PV market is dominated by wafer-based crystalline Si solar modules, making up over 90% of the total market share. They discussed the origins of losses in silicon cells, highlighting that they are different from other technologies due to their different design and mode of operation. Specifically, they attributed their Auger

recombination, their low open-circuit voltage, and their high material cost, to the indirect band gap of silicon.

GaAs and other III-V compound semiconductors have achieved efficiencies of over 20%, with record efficiency for a single-junction solar cell achieved using GaAs (28.8%).[12] However, due to small area fabrication from a relatively energy-intensive process, this technology is typically found in a niche market. Also, the use of arsenic requires strict encapsulation and recycling protocols. Newer technologies have been developed such as CdTe and copper-indium-gallium-selenide (CIGS) thin film solar cells, with the goal to reduce costs and enhance versatility. These technologies may have the potential to reach cost-effective photovoltaic-generated electricity.[13] However, these technologies also require a complex growth, sputtering, or evaporation technique.[12] Noufi *et. al.*[13] also listed long-term stability and the availability of the required materials as additional challenges.

In addition, there is the so-called "emerging technologies", such as dye-sensitized solar cells (DSSCs)[14], which provide a technically and economically alternative concept to p–n junction photovoltaic devices. A technology that offers a cheap and easy method to photovoltaic-generated electricity is organic solar cells[15], but their efficiency long term reliability must be improved to be competitive. With both of these technologies, and micro/nanocrystalline and amorphous Si, $Cu(Zn,Sn)(Se,S)_2$ (CZTS) and quantum dot solar cells, light management and carrier management are major problems that must be addressed.

The most recent and arguably very promising photovoltaic devices are the so-called perovskite solar cells (PSCs), that in less than ten years have already achieved power conversion efficiency values as high as 23.3% (Figure 1.4).[16] These all solid-state, thin-film devices have arisen from the field of dye-sensitized solar cells[17] with the innovation of inclusion of the organic–inorganic hybrid lead halide perovskite as the absorber material.

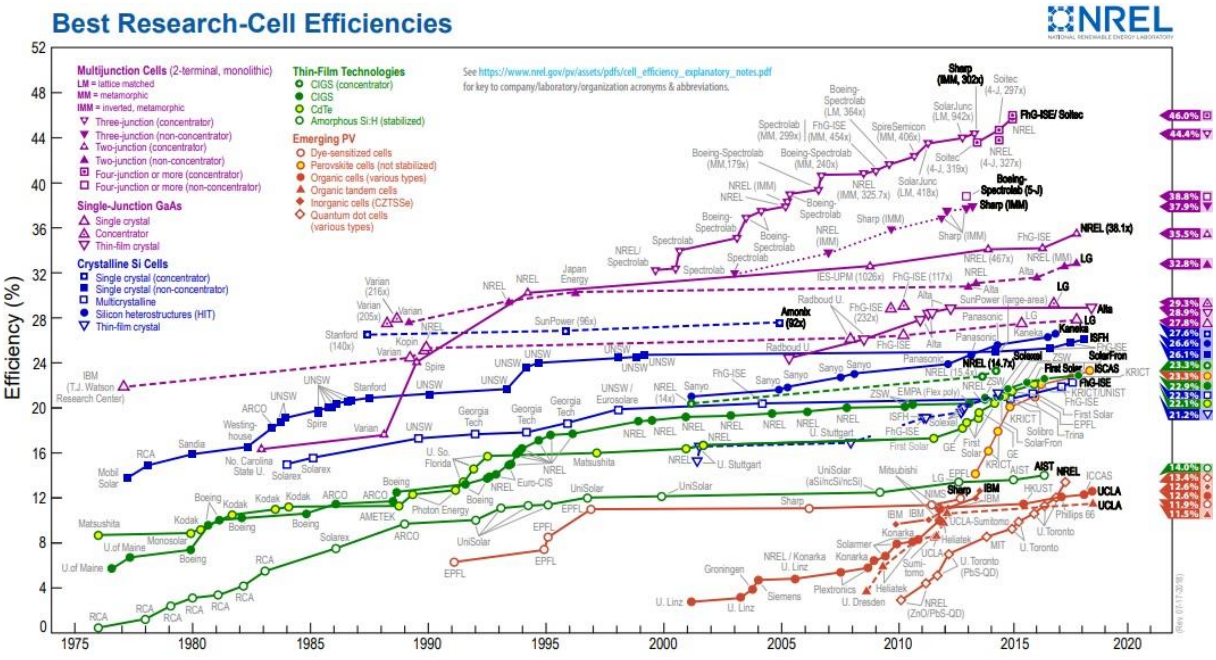

Figure 1-4. Best Research-Cell Efficiencies (republished with permission).[16]

1.3 Perovskite solar cells

Throughout this dissertation, a detailed introduction necessary to the chapter is offered. The performance of perovskite solar cells has improved significantly, starting with power conversion efficiencies of 3.9% in 2009 to 23.3% in 2018[16]. Perovskite crystals have

an AMX_3 structure (Figure 1.5)[18], where A is an organic or inorganic cation, M is a metal cation, and X is an anion which binds to both cations. For the nature of this work, A= caesium (Cs), methylammonium (CH_3NH_3 - MA), and/or formamidinium (CH_2NHCH_2 - FA); M= lead (Pb); and X=chlorine (Cl), bromine (Br), and/or iodine (I).

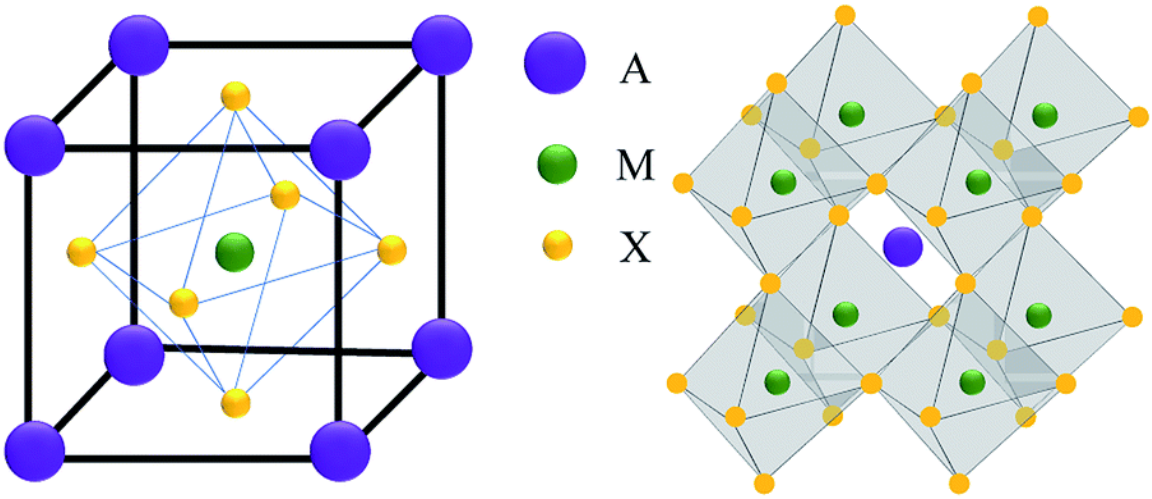

Figure 1-5. Crystal structure of perovskite with the chemical formula AMX_3 (republished with permission).[18]

Every individual component in the AMX_3 lead perovskites plays a role in their very impressive properties. The polar organic moiety (A) has been implicated in the materials' high dielectric constant, the formation of ferroelectric domains[19] and in a nanoscale charge localization in the valence band maximum and conduction band minimum,[20] which may play a role in the observed long carrier lifetimes. The halides (X) allow for the band gap of the perovskites to be changed dramatically when mixed in different ratios.[21, 22] The use of a metal ion with a $6s^2$ or $5s^2$ lone pair is thought to aid with defect tolerance, a high dielectric constant and low electron effective mass.[23] The material's properties were

recently dissected by Brandt *et. al.*,[23] where they attributed many of the impressive properties of perovskites to the dielectric constant and carrier effective mass. They discussed how a high dielectric constant could decrease the carrier capture cross-section, which increases τ, the low-injection electron and hole lifetimes. They also outlined how the low carrier effective mass and high dielectric constant could increase mobility. Using first principles calculations, Brandt *et. al* screened the Materials Project database, containing ~ 27,000 materials, and identified several promising alternatives to the choice of materials for use in perovskite solar cells.

In addition to varying the materials used to fabricate the perovskite crystal, the fabrication conditions can also be used to optimize device performance. Perovskites solar cells can be fabricated by various techniques, including solution processing techniques (Figure 1.6).[24] However, this work utilized the one-step and two-step spin-coating process (Figure 1.7)[25], due to its ease and reproducibility. Im *et. al.*[25] systematically evaluated the property-morphology relation from the diverse deposition methodologies of perovskite $CH_3NH_3PbI_3$. Their work demonstrated that both, the one-step and two-step spin-coating methods, resulted in reproducible photovoltaic performance, which is ideal for the current state of the work discussed in this dissertation. Spin coating starts with a complex solution involving various precursor components, solvents, additives, and antisolvents. The processing is carried out in an inert-gas glovebox that controls temperature and atmospheric conditions.

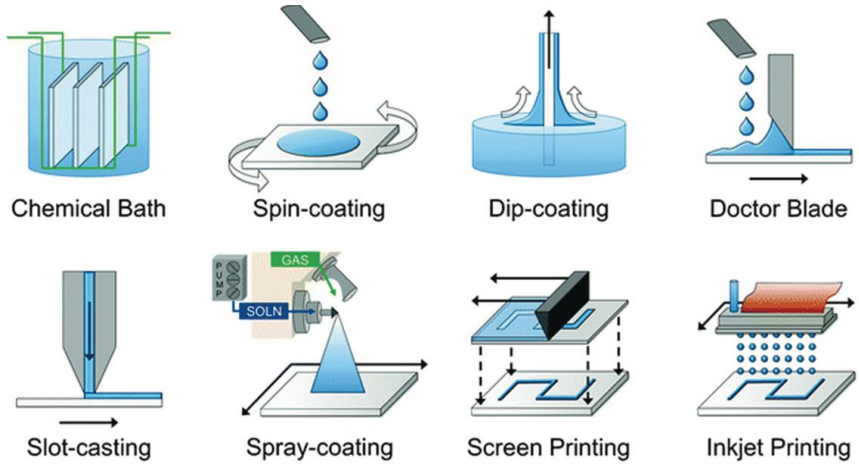

Figure 1-6. Fabrication techniques used for the perovskite crystal in perovskite solar cells (republished with permission).[24]

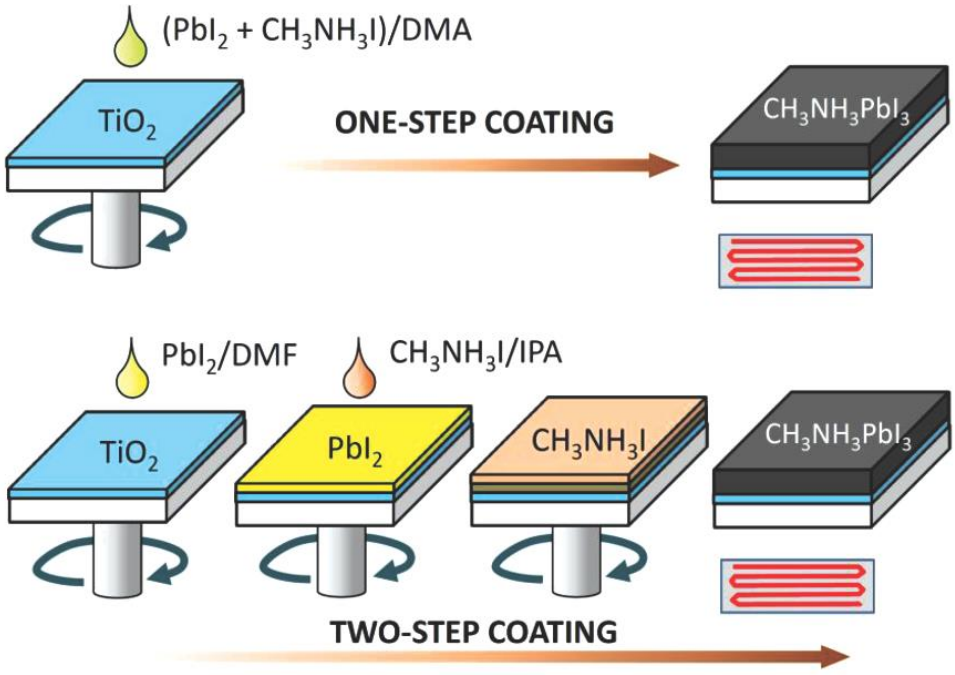

Figure 1-7. One-step (top) and two-step (bottom) spin-coating technique (republished with permission).[25]

The one-step spin-coating technique (Figure 1.7 (top)) combines all components needed to produce the perovskite crystal in a single solvent. The precursor solution is then spun onto the substrate, and then annealed, typically in an inert gas atmosphere. In the two-step spin-coating process (Figure 1.7 (bottom)), there are now two precursor solutions. The first precursor solution only contains the lead halide. The precursor solution is spun onto the substrate and then annealed to produce a PbX_2 crystalline film. A second precursor solution is made containing the materials from A and X. These materials are dissolved in a solvent that will not redissolve the PbX_2 film. This precursor solution is "loaded" onto the PbX_2 crystalline film. After the desired loading time is achieved, the precursor solution is spun onto the PbX_2 film surface and then annealed to produce the perovskite crystal. Throughout this work, I explore various precursors, additives, loading times and processing procedures.

Two of the most common perovskite device structures are shown in Figure 1.8. They are the mesoscopic nano-structured (left) and planar structured (right) perovskite solar cells.[26] The device structure, related materials, and interfacial modification are crucial factors in optimal device performance. For instance, the layers on each side of the perovskite layer can encourage or discourage electrons and holes from travelling in a certain direction, preventing recombination. The most common material for an electron transport layer is TiO_2 due to its large band gap and alignment with the perovskite conduction band (Figure 1.9). An organic material is typically used for the hole transport layer due to temperature restrictions on the underlaying perovskite layer. In addition, the material deposited onto the perovskite layer must also be available in a solvent that will not redissolve the perovskite film. However, in Chapter 4, a novel architecture is utilized

that allows for CuSCN to be used as the hole transport layer, which aligns well with the valence band of the perovskite material (Figure 1.9).

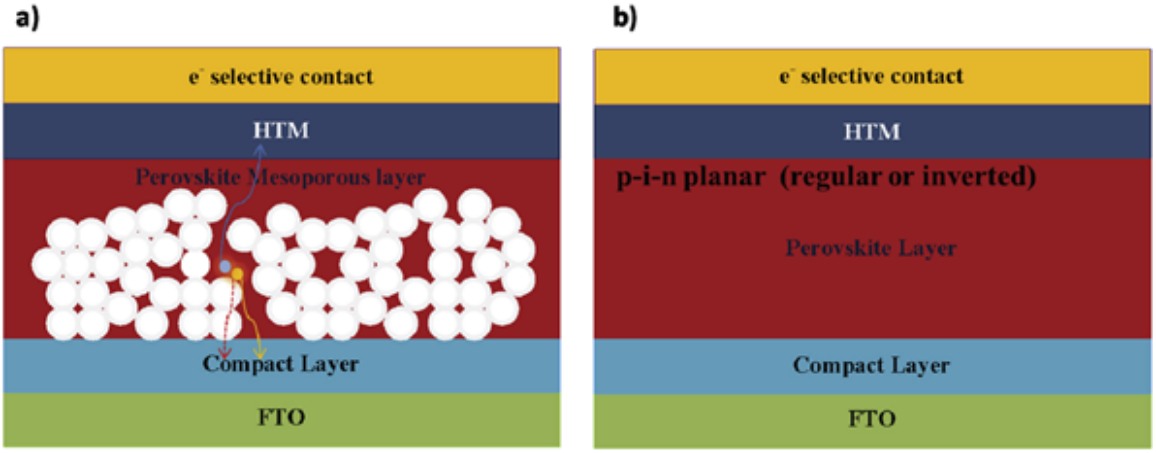

Figure 1-8. Mesoscopic nano-structured (left) and planar structured (right) perovskite solar cells (republished with permission).[26]

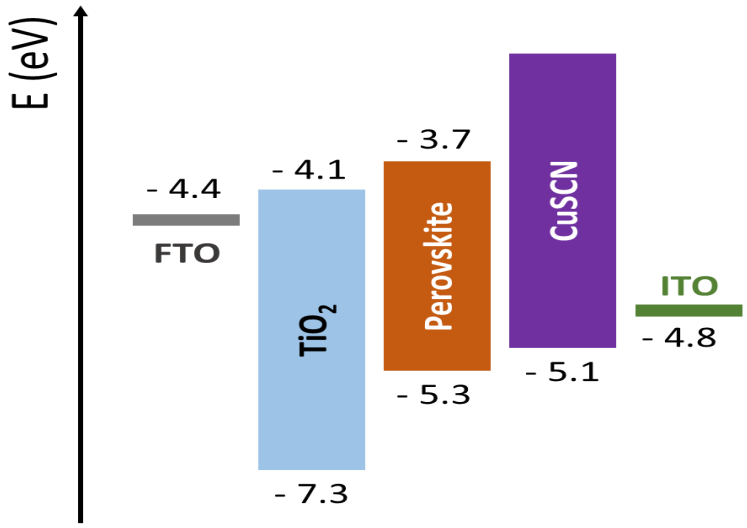

Figure 1-9. Energy diagram of a perovskite solar cell fabricated in Chapter 6 of this work (republished with permission).[27]

1.4 Weaknesses of perovskite solar cells

Safety concerns from the lead-based material aren't the only downfall of the perovskite solar cells. Liu *et. al*.[28] used first-principle calculations to explore the effect of water on the structure and properties of the organo-lead-iodide perovskite. Their work demonstrated that water can easily penetrate the large interspace of the AMX_3 perovskite, which can corrode the entire structure over time. Kelly *et. al*.[29] demonstrated with empirical studies the effect of humid environments on the perovskite active layer. Using *in-situ* absorption spectroscopy, they were able to demonstrate the effect of increased humidity on the extent of perovskite degradation (Figure 1.10). Focusing on the 410 nm wavelength as a function of time for perovskite films exposed to various relative humidity, they were able to determine how quickly the degradation occurs (Figure 1.11). In this preliminary work, they postulated the following equation to represent the decomposition of the MAPbI3 perovskite crystal:

$$4CH_3NH_3PbI_3 + 2\,H_2O = (CH_3NH_3NH_3)_4PbI_6 * 2H_2O + 3PbI_2$$

Their ex situ pXRD data went on to further demonstrate decomposition of CH_3NH_3I to CH_3NH_2 and HI, ultimately leaving PbI_2 as the only byproduct of the reaction. In this work, they also demonstrated that an adequate transport layer can have a dramatic impact on the stability of the material. In Chapters 2, 3, and in our current work, we look at new processing methods and dopants to protect the perovskite crystal from moisture exposure.

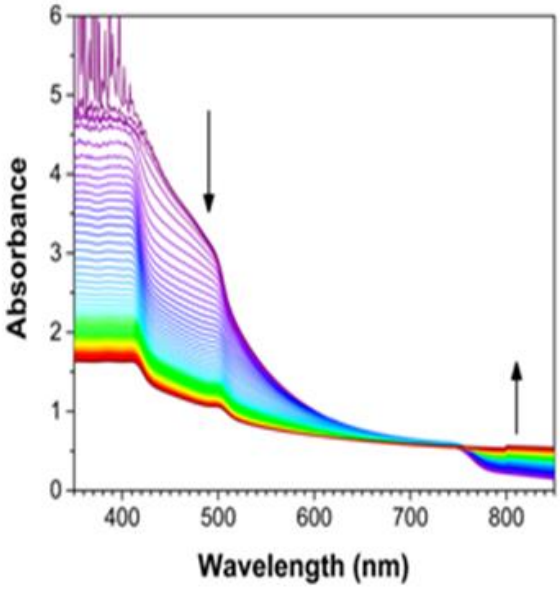

Figure 1-10. Perovskite degradation with time (republished with permission).[29]

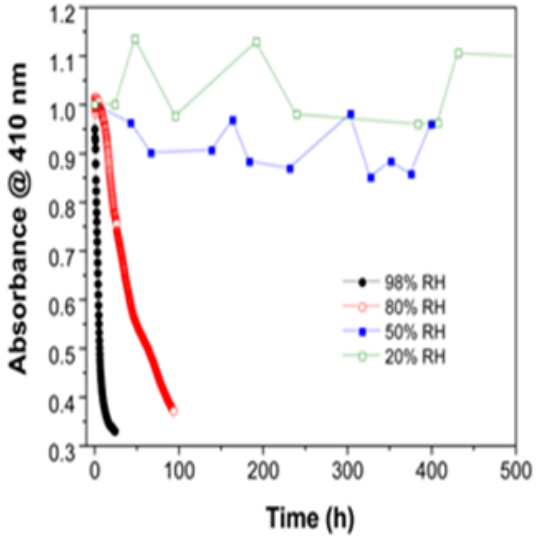

Figure 1-11. Degradation rate at varying relative humidity (republished with permission).[29]

In addition, perovskite solar cells tend to have issues with reproducibility and display hysteresis.[30] Hysteresis is an effect observed in the current-voltage measurements where the power conversion efficiency values are highly dependent on scan rate, scan direction, scan history, and light exposure. Recently, a significant amount of work has gone into perovskite solar cell band alignment engineering, through applications of various materials (Figure 1.12), to increase efficiency and decrease hysteresis (Figure 1.13).[31-37] Alignment with the perovskite conduction and valence band has been shown to benefit the device. Specifically, reports have demonstrated that reducing the mismatch between the energy levels of the perovskite active layer and transporting materials promotes the transfer of charge carriers and increases the output voltage.[31, 32]

Hagfeldt *et. al*.[31] recently carried out work varying the electron transport layer between TiO_2 and SnO_2. TiO_2 exhibits a band misalignment with the $MAPbI_3$ perovskite, which they claimed leads to strong hysteresis and scan rate dependent current densities (Figure 1.12). This is typically representative of capacitive effects at the interface. SnO_2, however, achieved a barrier-free energetic configuration, obtaining practically hysteresis-free power conversion efficiencies of over 18% with record high voltages of up to 1.19 V (Figure 1.13). This work demonstrated that engineering the alignment of the perovskite conduction band with the electron transport layer can result in planar, high performance perovskite solar cells with high voltages and remarkably good stability over time.

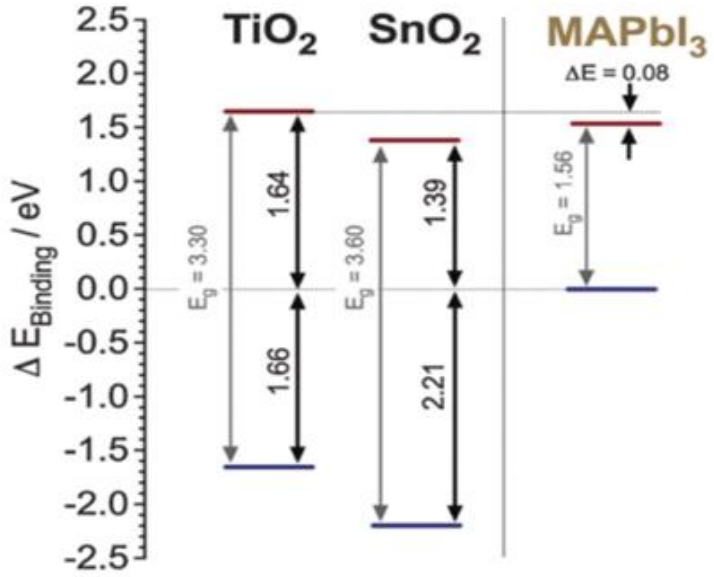

Figure 1-12. Energy misalignment and alignment with TiO_2 and SnO_2 respectively (republished with permission).[31]

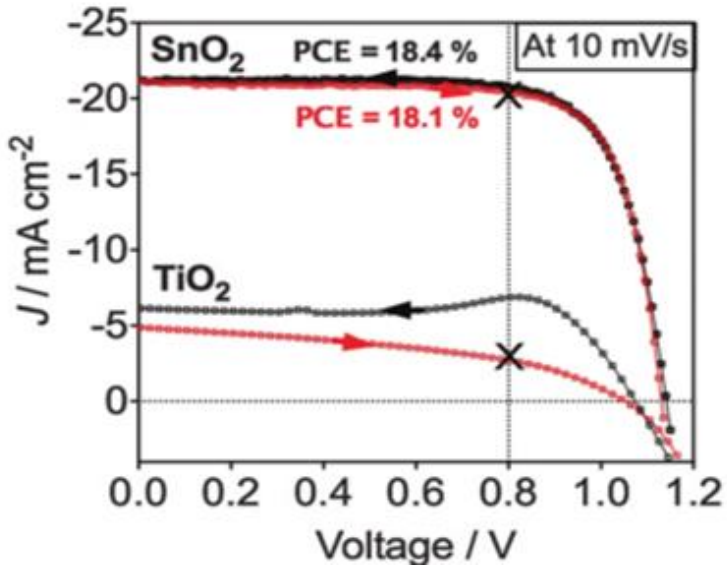

Figure 1-13. Demonstration of significant hysteresis effect improvement using SnO_2 compared to TiO_2 (republished with permission).[31]

Lee *et. al*.[32] demonstrated that alignment with the perovskite valence band also has its advantages. A high power conversion efficiency was achieved by enriching poly(3,4-ethylenedioxythiophene) polystyrene sulfonate (PEDOT:PSS) with perfluorinated ionomers resulting in a self-organizing hole transport material (also referred to as self-organized hole extracting layer, SOHEL) that aligned well with the valence band of the perovskite (Figure 1.14). Their material achieved excellent energy level alignment with the valence band of the perovskite, which increased the built-in potential. Due to the increased built in potential, the device's open circuit voltage, fill factor, and short circuit current were increased.

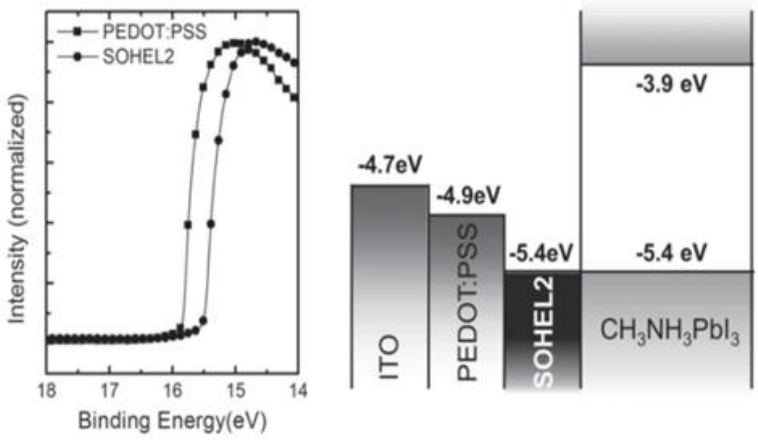

Figure 1-14. Alignment of the modified polymer hole transport layer with the perovskite valence band (republished with permission).[32]

The effects of band alignment with the transparent electrode layer were also investigated. Yang *et. al*.[37] attempted to align the electron transport layer with the modified electrode layer. They also modified the TiO_2 to align better with the perovskite layer (Figure 1.15). In this work, they were able to achieve significantly enhanced performance,

which they claimed was due to a narrower depletion region. They proposed that this lowers the contact resistance and facilitates charge extraction at both interfaces adjacent to the modified TiO_2. In the work discussed in this thesis, we investigate how any modifications improve or impede the hysteresis of the device to expand on the fundamental investigation of hysteresis. In addition, Chapter 5 looks at methods for work function modification of ITO through a sputtering co-deposition process.

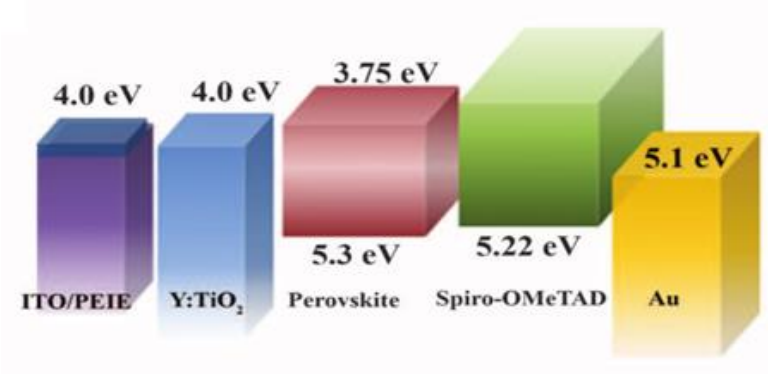

Figure 1-15. Alignment if TiO_2 with the adjacent layers by modifying ITO and TiO_2 (republished with permission).[37]

Lastly, a concern not directly related to the perovskite itself, but related to the current technology for the electron transport layer, is the use of TiO_2. TiO_2 commonly requires sintering temperatures greater than 500°C.[38] This limits the architecture of the device, forcing an inverted geometry, and restricts the range of substrate materials that it can be deposited on. The typical transparent electrode for photovoltaic work is indium tin oxide, but temperatures greater than 300°C have been shown to increase the resistance of the indium tin oxide by over a factor of 4.[39] Fluorine doped tin oxide is a decent electrode replacement for indium tin oxide, but recent work looking at the crystal structure of various

electrodes vs. temperature demonstrated that even at 500°C the fluorine doped tin oxide was degraded, as indicated by changes in its diffraction pattern (Figure 1.16).[40, 41] This thesis will finish with exploring the doping of indium tin oxide, and how it may lead to a viable alternative to the commercial standard ITO as an electron/hole transport layer free electrode.

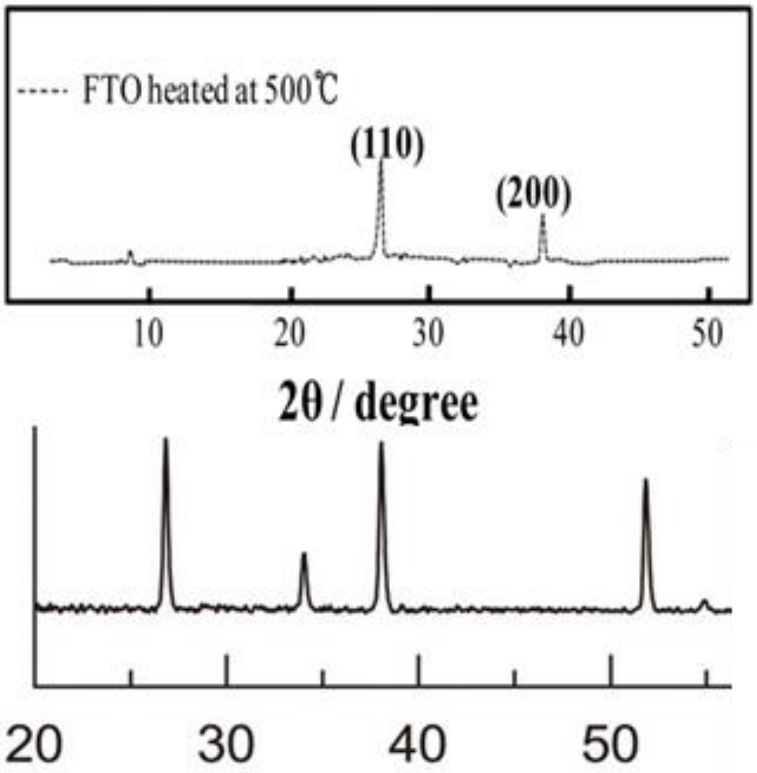

Figure 1-16. FTO XRD patterns before (below) and after (above) annealing (republished with permission).[40, 41]

1.5 Thesis organization

The remaining chapters of the Thesis are organized as follows. Chapter 2 will introduce the reader to a new processing step for the two-step procedure that produced a

very uniform $CH_3NH_3PbI_3$ film in ambient conditions. This work demonstrated the importance of morphology control in the PbI_2 phase for high-performance PSCs fabricated under ambient conditions. However, this procedure required a post-annealing technique, which is not ideal for large-scale fabrication of perovskite solar cells. Our current and future work will build on this work to make it more practical for role-to-role production. Chapter 3 will explore incorporation of polyvinylpyrrolidone into the one-step precursor solution, which was shown to protect the active material against degradation under humid ambient conditions. In Chapter 3, investigation of the materials' mechanical flexibility and integrity was also performed. The flexible solar cells produced an efficiency of ca. 15%, whereby the efficiencies were stable over several bending cycles. Chapter 4 focuses on a new architecture to reduce parasitic absorption by the top contact. This new class of devices offers straightforward strategies for optimization that could significantly increase the efficiency. Simulations showed that if these improvements can be achieved, they will offer a pathway to efficient, semitransparent photovoltaic devices. Chapter 5 explores a new processing procedure for ITO to tune the work function to align better with the valence band of the perovskite active layer. Chapter 6 will provide concluding remarks for the performed work and future work will be discussed and suggested.

CHAPTER 2. SOLVENT VAPOR ANNEALING OF ORIENTED PbI_2 FILMS FOR IMPROVED CRYSTALLIZATION OF PEROVSKITE FILMS FOR AIR-STABLE SOLAR CELLS[1]

2.1 Introduction

Organic-inorganic halide perovskite solar cells (PSCs) are now a top candidate for high-performance and low-cost thin film photovoltaics, owing to their excellent optical and electronic properties including high absorption coefficient,[42-44] high electron-hole diffusion length,[45, 46] and superior power conversion efficiency (PCE).[47, 48] Methylammonium lead halide ($CH_3NH_3PbX_3$, $MAPbX_3$) is the most commonly used perovskite for PSC applications.[49, 50] The first PSCs fabricated using $MAPbI_3$ and $MAPbBr_3$ as a sensitizer in a liquid-electrolyte-based dye-sensitized solar cells delivered a modest PCE of 3.8%.[51] During the time of the present investigation, the record PCE was 22.1%, certified by the National Renewable Energy Laboratory.[52] This efficiency surpasses many other photovoltaic technology candidates.[53, 54]

The crystallinity and morphology of perovskite films are known to be crucial factors in the fabrication of high-efficiency devices.[55] Significant research efforts have been devoted to the design and processing of perovskite active layers, including approaches such as one-step solution spin-coating,[56] vacuum vapor deposition,[49] and two-step sequential deposition processing.[57] The goal of all these methods is to prepare compact, smooth

[1] Xiong, Hao, Giovanni DeLuca, Yichuan Rui, Yaogang Li, Elsa Reichmanis, Qinghong Zhang, and Hongzhi Wang. "Solvent vapor annealing of oriented PbI2 films for improved crystallization of perovskite films in the air." Solar Energy Materials and Solar Cells 166 (2017): 167-175.

perovskite films with large crystalline grains. Whichever method is used, it is evident that optimizing the crystallization and grain growth conditions is critical to enhance device performance.

Park et al. reported an efficient method for preparing high efficiency perovskite solar cells under high relative humidity.[55] In their research, both substrate and PbI_2 temperature were key factors that controlled perovskite film morphology, which determined the final efficiency of the device. Precise control of temperature and humidity is difficult, but in the absence of requisite control, resultant perovskite films were not smooth, leading to interface defects between the perovskite and hole transport layers. Kelly[58] and his coworkers explored the effect of relative humidity on crystal growth and found that perovskite crystallite size increased with increasing humidity; however, the perovskite films prepared under varying humidity conditions were neither uniform nor compact.

To improve the perovskite grain size, many researchers post-modified perovskite films by solvent annealing in a controlled environment.[59, 60] Lau et al. optimized a solvent annealing method to improve crystallization of perovskite films and obtained an efficiency of over 13%.[61] Though post-solvent annealing can increase perovskite crystallinity, excessive residual solvent is harmful to device performance. To avoid the problem mentioned above, several researchers modified the morphology of PbI_2, immediately obtaining uniform perovskite films. For instance, Han et al. first prepared compact amorphous PbI_2 for dipping deposition, however, the compact perovskite films were comprised of grains that were only around 200 nm in size.[62] Zhang et al. pretreated PbI_2 with hexamethylphosphoric triamide (HMPA), further reducing the interfacial contact

between the perovskite film and TiO_2 layer.[63] Gong and his collaborators designed a mesoporous PbI_2 scaffold for high performance planar perovskite solar cells, thereby obtaining a highly-crystalline perovskite film.[64] Though these results are ideal, preparation of large grain-size crystalline perovskite films in the ambient environment is still under exploration.

Inspired by solvent post-annealing, we demonstrate a straightforward method to form a high quality, oriented, crystallized PbI_2 film using a vapor post-annealing approach. The PbI_2 film subsequently affords a compact, large grain size, pinhole-free $CH_3NH_3PbI_3$ film under humid ambient conditions. It was found that the highly-crystalline perovskite films can significantly improve device performance and stability under humid ambient conditions.

2.2 Experimental section

2.2.1 Materials and reagents

Unless stated otherwise, all materials were purchased from Sinopharm Chemical Reagent Co., Ltd. and used as received. CH_3NH_3I and Spiro-MeOTAD (2,2',7,7'-tetrakis(N,N-di(4-methoxyphenyl)amine)−9, 9'-spiro-bifluorene, purity ≥99.5%) were purchased from Xi'an Polymer Light Technology Corp. The TiO_2 paste (NJU-SR) was purchased from Kunshan Sunlaite New Energy Co., Ltd. FTO glass (14 Ω/□) was purchased from Nippon Sheet Glass Co., Ltd.

2.2.2 $CH_3NH_3PbI_3$ film fabrication

The perovskite films were fabricated using a sequential deposition process. PbI_2 (462 mg) was dissolved in anhydrous DMF or DMSO at 70 °C, to form a 1 M PbI_2/DMF or PbI_2/DMSO solution. The PbI_2/ DMF solution was deposited onto a FTO glass substrate by spin coating at 3000 rpm for 30 s, and the resultant film was then annealed for 10 min at 70 °C in the ambient to afford dense PbI_2 (d-PbI_2). The PbI_2/ DMSO solutions were spin-coated onto the substrates at a spin speed of 3000 rpm for 30 s, followed by annealing for 10 min at 70 °C. The PbI_2/DMSO based substrates were divided into two groups. One group formed amorphous PbI_2 (a-PbI_2). The other group was left on top of the hot plate at 70 °C for 10 min and covered by a glass petri dish. DMF solvent (20 μL) was introduced to the edge of the petri dish during the thermal-annealing process. This allowed the DMF vapor to diffuse under the edge of the petri dish and into the surrounding space above the PbI_2 coated substrate and contact the PbI_2 film. The DMF vapor was expected to be able to penetrate the compact amorphous PbI_2 film and promote the growth of PbI_2 crystals, forming microporous PbI_2 (m-PbI_2).

CH_3NH_3I dissolved in 2-propanol (10 mg/mL) at 80 °C was loaded onto d-PbI_2 coated, a-PbI_2 coated and m-PbI_2 coated substrate where it remained undisturbed for 20 s (loading time). The substrate was then spun at 4000 rpm for 30 s and annealed at 110 °C for 10 min, forming the dark perovskite layer. The operation was carried out under humid ambient conditions.

2.2.3 Device fabrication

Solar cells having a mesoporous structure were prepared.[48] The FTO glass substrates (2.5 cm×2.5 cm) were sequentially washed through an ultrasonic treatment in

detergent, acetone, ethanol and deionized water, and treated in O_2 plasma (DT-01, Suzhou Omega Machinery Electronic Technology Co., Ltd.). A thin layer of compact anatase TiO_2 was formed through spin-coating using a mixed solution of titanium source on the clean substrates at 2000 rpm for 30 s, followed by a sintering process at 500 °C for 2 h. The mixed solution of titanium source was prepared as follows. Tetrabutyltitanate (850 μL) and diethanolamine (210 μL) were dissolved in ethanol (2.625 mL) under vigorous stirring for 1 h. Then 1.25 mL ethanol and 45 μL deionized water were added into the solution under vigorous stirring for 24 h. The mesoporous TiO_2 layer was deposited by spin coating an unfiltered (2:7) TiO_2 paste: ethanol solution at 4000 rpm for 30 s and annealed at 500 °C for 30 min. After the perovskite films formed, a volume of 25 μL of spiroOMeTAD solution (80 mg/mL in chlorobenzene) was spin-coated onto the prepared perovskite film at 4000 rpm for 30 s. Finally, the devices were coated with a gold electrode 80 nm in thickness by evaporation through an aperture mask in a vacuum chamber. The active area of perovskite device is 0.16 cm^2.

2.2.4 Characterization

The perovskite film was identified by one-dimensional X-ray diffraction (1D XRD) (Model D/max 2550 V, Rigaku Co. Tokyo, Japan) by using Cu Kα (λ=1.5406 Å) radiation. Two-dimensional wide-angle X-ray diffraction (WAXD) analysis was conducted using a Bruker D8 Discover GADDS X-ray Diffractometer operating at 40 kV and 40 mA, Cu Kα radiation. The morphology of the resultant perovskite film was observed by using field-emission scanning electron microscopy (FESEM, Model S-4800, Hitachi, Japan). Tapping mode atomic force microscopy (AFM) imaging was carried out using a Multimode NanoScope IV system (Veeco, Santa Barbara, CA) at a scanning range of 2 μm and a

scanning speed of 3.001 Hz. Steady-state photoluminescence (PL) spectra were acquired with a FLS920 transient optical spectrometer (Edinburgh Instruments, UK). The photocurrent density-voltage (J-V) curves of the PSCs were performed by a Keithley model 2400 source measure unit. A solar simulator (Model 96160 Newport Co., USA) equipped with a 300 W xenon lamp was used as a light source, where the light intensity was adjusted using an NREL-calibrated Si solar cell with KG-1 filter for approximating the AM 1.5 G one sun light intensity. The cell performance parameters, including short-circuit current density (J_{sc}), open-circuit voltage (V_{oc}), fill factor ($FF=P_{max}/(J_{sc}V_{oc})$), and photoelectron conversion efficiency ($h\ (\%) = J_{sc}*V_{oc}*FF/\text{total incident energy}\times100$), were measured and calculated from the J-V characteristics. The incident-photon-to-current conversion efficiency (IPCE) spectra were measured as a function of the wavelength from 350 to 800 nm using a specially designed IPCE system (Newport Co., USA). Solar cell characterization and storage were carried out in ambient room conditions without encapsulation.

2.3 Results and discussion

2.3.1 Perovskite film characterization

High-quality perovskite films with no voids in the active layer is a key requirement for making high efficiency perovskite solar cells. However, perovskite films prepared in ambient conditions are poor, especially using a solvent method when the humidity is greater than 40%,[57] which derives from the propensity of traditional PbI_2 structures to absorb water molecules. We optimized the preparation conditions of PbI_2 films, and further prepared compact, pinhole-free perovskite films in ambient conditions.

Based on detailed investigations of perovskite film growth, a model shown schematically in Figure 2.1 was proposed. As the films were placed in a closed space, the solvent vapor could condense on the PbI_2 film surface. Simultaneously, the high substrate temperature could lead to solvent re-evaporation, where a simple dynamic near-equilibrium may exist.[61] It is well known that a rapidly crystalized, layered and dense PbI_2 film can be obtained under DMF vapor using the traditional method. Alternatively, using DMSO as the solvent for the PbI_2 precursor solution, an amorphous PbI_2/DMSO intermediate is expected to form. Through annealing at 70 °C for several minutes, DMF molecules can infiltrate the layer and thereby substitute residual DMSO in the film, leading to PbI_2 recrystallization. The exchange between DMF and DMSO forms small pores in the PbI_2 films. PbI_2 film morphology and composition will be discussed later.

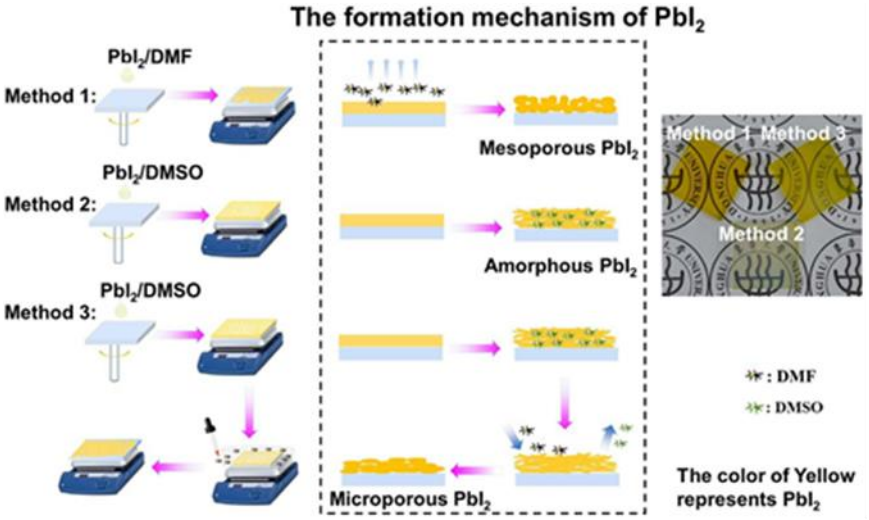

Figure 2-1. Schematic diagram for the preparation of the three types of PbI2 films and corresponding optical photographs.

Figure 2.2a-2.2f depicts FE-SEM images of d-PbI_2, a-PbI_2 and m-PbI_2. Under ambient conditions, d-PbI_2 formed a dense layer (Figure 2.2a), while a-PbI_2 presented a

compact, amorphous surface due to the formation of the PbI_2•DMSO intermediate (Figure 2.2b) and m-PbI_2 exhibited a microporous structure. Figure 2.3 shows the pore size distribution for d-PbI_2, a-PbI_2 and m-PbI_2 film, which are calculated from the FE-SEM images. The pore sizes of the m-PbI_2 film are bigger than the two other films. Notably, the pore sizes of the d-PbI_2 film are negligible.

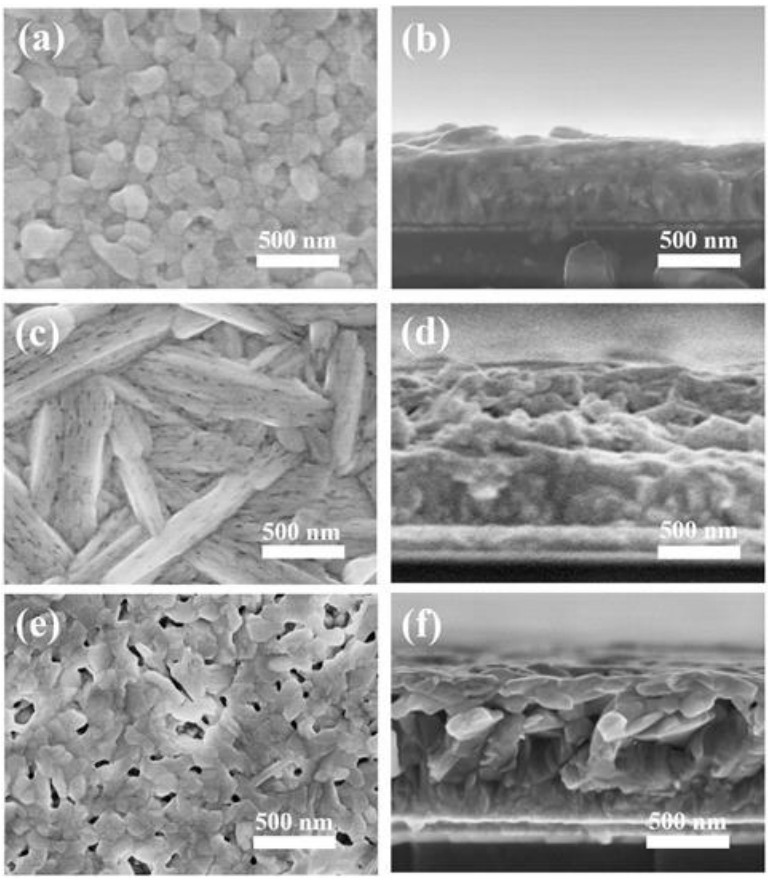

Figure 2-2. Surface (left column) and Cross-sectional (right column) FE-SEM image of PbI2 films (top row) sample 1(a)(b), sample 2(c)(d) and sample 3(e)(f).

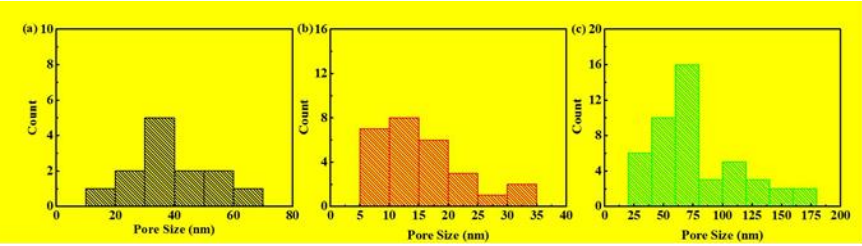

Figure 2-3. Pore size distribution for d-PbI2 (a), a-PbI2 (b) and m-PbI2 (c).

Though d-PbI_2 can easily interact with CH_3NH_3I solution via the dipping method,[65] the perovskite film that formed contained residual PbI_2. On the other hand, d-PbI_2 films can react with CH_3NH_3I efficiently, only requiring the infiltration of CH_3NH_3I into the interstices. However, the dense structure readily absorbs moisture. The absorbed water molecules would redissolve CH_3NH_3I, resulting in a decrease in CH_3NH_3I solution concentration, leading to formation of perovskite cuboids (Figure 2.4a).[66] Perovskite crystals are also generated from a-PbI_2 films due to the stronger binding capacity of CH_3NH_3I vs. DMSO molecules with Pb^{2+}, resulting in homogeneous, perovskite films comprised of small crystals (Figure 2.4c).[67] The m-PbI_2 combines the favorable features of d-PbI_2 and a-PbI_2 films, resulting in formation of compact highly-crystalline perovskite films in ambient conditions (Figure 2.4e). The mechanism of crystal growth can be explained by the nucleation growth of perovskite crystals.[68] During DMF solvent annealing, oriented PbI_2 crystals reformed, and then became the nucleating point upon contact with CH_3NH_3I solution.

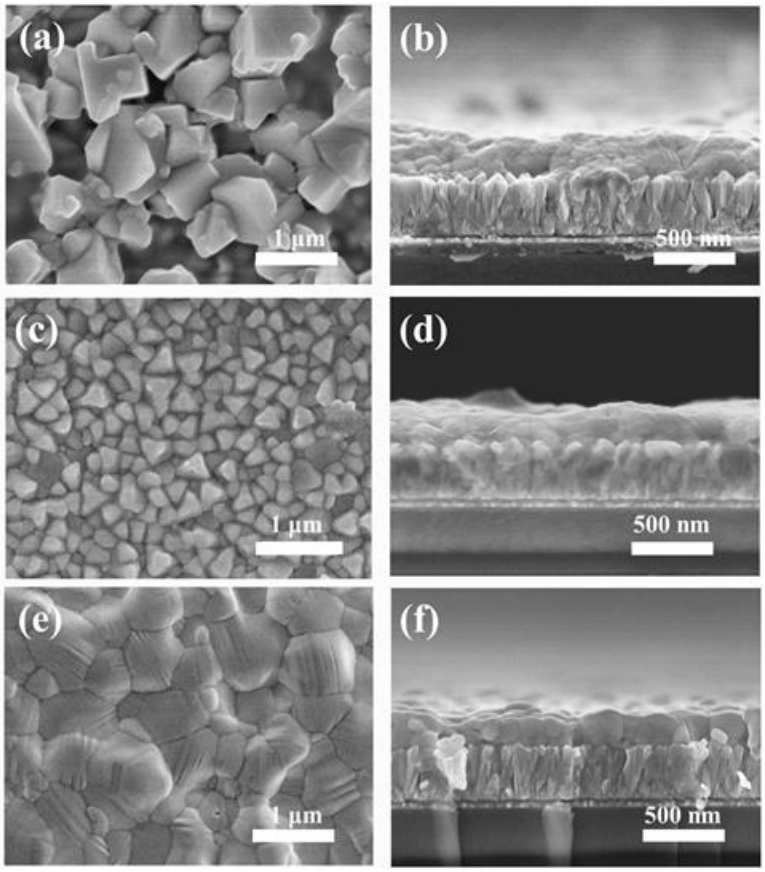

Figure 2-4. Surface (left column) and Cross-sectional (right column) FE-SEM image of perovskite films sample 1(a)(b), sample 2(c)(d) and sample 3(e)(f).

Two-dimensional wide-angle X-ray diffraction (2D WAXD) is widely used for analysis of the structure of solid materials, such as polymer crystals, polymer fibers, thin-film materials, bulk materials, etc.[69-72] The fractions of crystalline, mesomorphic and amorphous phases, as well as other structure parameters can be obtained directly from analysis of the images that obtain. Through 2D WAXD image analysis, oriented, disordered or amorphous phase can be determined by spots, circles or nothing in the images, respectively. The brightness in the images represents the crystallinity of film. The continuity of circles represents the reduced crystallographic orientation. Figure 2.5 shows 2D WAXD patterns for PbI_2 and the corresponding perovskite films prepared from the

three methods. There are strong diffraction arcs (or spots) at Bragg angles 2θ =12.6° observed for d-PbI_2 and m-PbI_2, which is attributed to the (001) lattice plane. The arc width of the strongest equatorial reflection provides a strong indication of the degree of orientation within the samples. The rings observed in the WAXD data for sample 1 are indicative of the random orientation of PbI2 crystals. In contrast, the aligned PbI_2 crystals show a distinctive molecular orientation, as detected by the discrete reflections in Figure 2.5c. More importantly, a-PbI_2 exhibited weak diffraction arcs at Bragg angles 2θ =9.9°, which contributed to the $PbI_2(DMSO)_2$ complex.[73] To further elaborate PbI_2 film diffraction data, the one-dimensional X-ray diffraction patterns were both integrated from 2D WAXD and measured by an XRD detector.

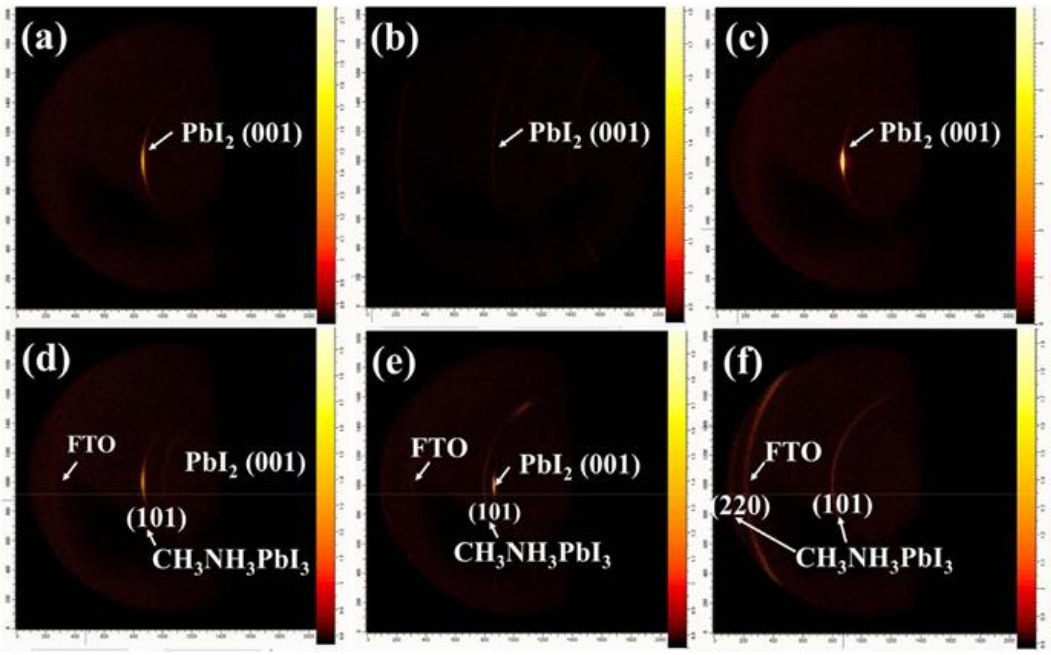

Figure 2-5. Two-dimensional WAXD pattern (covered from 2θ=5° to 2θ=20°) of PbI2 from sample 1 (a), sample 2 (b), sample 3 (c) and corresponding perovskite films (d-f).

Though more information about the PbI_2 films can be obtained from 2D WAXD, such as oriented crystallization and residual stress, the 2D and 1D XRD results are essentially the same. Figure 2.6 shows 1D XRD spectra measured from the 1D detector and integrated from 2D XRD. The a-PbI_2 films shown in Figure 2.6a have a broadened diffraction peak at $2\theta = 9.9°$. The 1D XRD patterns of d-PbI_2 and m-PbI_2 in Figure 2.6 show intense peaks at $2\theta = 12.6°$ (001), 25.5° (002), 38.5° (003) and 52.2° (004) corresponding to the characteristic peaks of the PbI_2 layer.[74] It has been reported that PbI_2 crystals deposited from DMF solvent grow in a preferential orientation along the c axis.[75] For m-PbI_2, we find that the (001) diffraction peaks increase in intensity, suggesting a stronger degree of the PbI_2 oriented crystallinity. The diffraction peaks of the perovskite films resulting from the corresponding PbI_2 films were observed at 2θ values of 14.39° (101), 28.35° (220) and 31.93° (141).[76] In addition, other diffraction peaks at 2θ values of 20.08° (200), 24.60° (220), 40.81° (400) were found in sample 3, which were growth in a manner that conforms to the heterogeneous growth mechanism.[77] The signature peak of PbI_2 at 12.6° was observed in sample 2 (Figure 2.6b and 2.6d), which was a result of the incomplete consumption of PbI_2 in ambient conditions.[78]

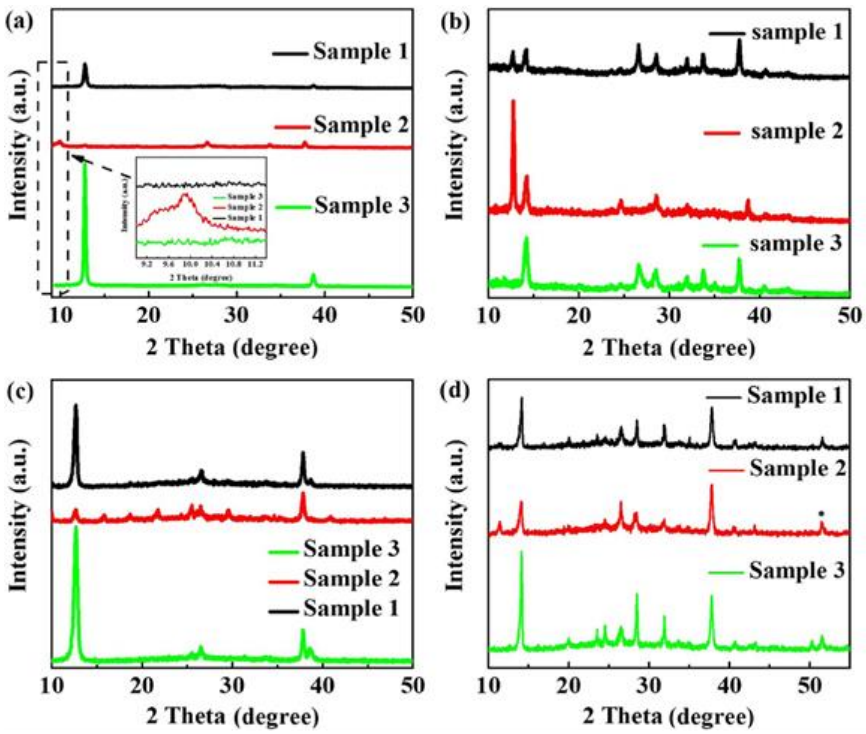

Figure 2-6. One dimensional XRD spectra of PbI2 films and corresponding perovskite films integrated from Two WAXD pattern (a)(b), measured from One WAXD pattern(c)(d).

Figure 2.7a shows the UV–vis absorption spectra of d-PbI_2, a-PbI_2 and m-PbI_2. The highest absorption among the three alternatives is exhibited by d-PbI_2. In Figure 2.7a, m-PbI_2 shows a slight decrease in the absorbance throughout the spectrum, which can be explained by oriented PbI_2 crystal structure. The minimal absorbance observed for a-PbI_2 film is attributed to the amorphous nature of PbI_2, as demonstrated by both FE-SEM images and XRD. Figure 2.7b presents the UV–vis absorption spectra of the resultant perovskite films. The maximum absorption was observed for sample 3 and is attributed to the larger crystallite size and better grain interconnectivity as shown in FE-SEM image (Figure 2.4).

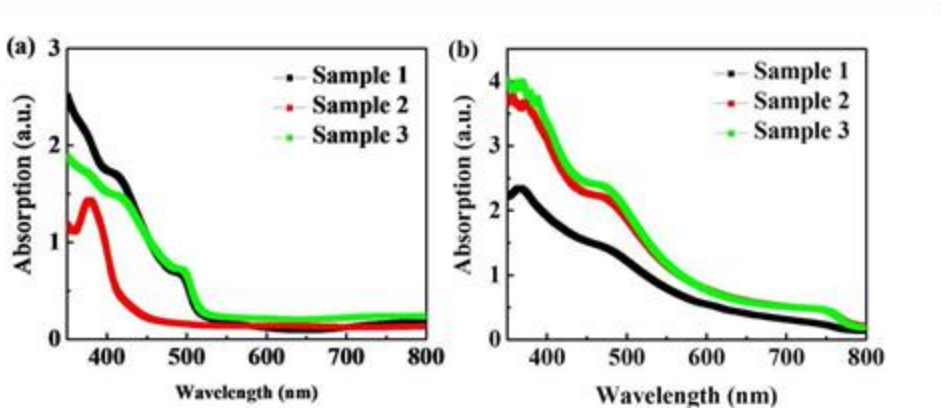

Figure 2-7. UV-visible absorption spectra of PbI2 films (a) and corresponding perovskite films (b) on FTO glass.

Photoluminescence (PL) spectroscopy provides insightful information on the charge carrier extraction properties of solar cells fabricated from the three perovskite samples. $CH_3NH_3PbI_3$ is a highly luminescent material, which means that the quenching of its PL intensity can be used as a measure of the charge extraction ability of the perovskite layer.[79] Figure 2.8a presents the PL spectra of the samples investigated here. The perovskite PL spectra show an intense peak at 770 nm (eV), which is in good agreement with the absorbance spectra. For sample 2, however, a blue-shift to 765 nm was observed. This change in absorbance is believed to be related to the presence of unreacted PbI_2.[80] Additional support for the presence of PbI_2 ID derived from Energy Dispersive Spectrometer data pertaining to the measured Pb/I ratio shown in Table 2.1.

Table 2-1. Atomic percentages in the perovskite film.

Perovskite Film	C	Si	I	Pb	Al	Sn	O	I/Pb
Sample 1	33.04	1.88	20.12	7.20	5.77	14.53	17.45	2.79
Sample 2	36.40	2.46	18.98	7.36	6.34	15.86	12.61	2.57
Sample 3	36.70	1.51	23.94	8.13	4.43	13.31	11.99	2.94

From the data analysis, the elemental Pb content is slightly enriched in the film which supports the UV–vis analysis above. To study the dynamics of electron lifetimes between the devices, time-resolved photoluminescence (TRPL) spectroscopy was also performed. Figure 2.8b illustrates the TRPL spectroscopic analysis of three perovskite films fabricated on FTO glass. Such measurements provide quantitative information associated with light-induced charge separation.[81] Samples 1 and 2 exhibited a time constant of τ_e =16.76 ns, and τ_e =22.60 ns, respectively, whereas sample 3 exhibited a better value of τ_e =32.14 ns. Charge carriers possessing longer lifetimes are expected to have a lower defect concentration.[82] The higher electron lifetime is due to the low recombination rate. The increase in photocurrent density is likely to be in part related to the rapid transport rate, associated with the efficiency of charge collection.

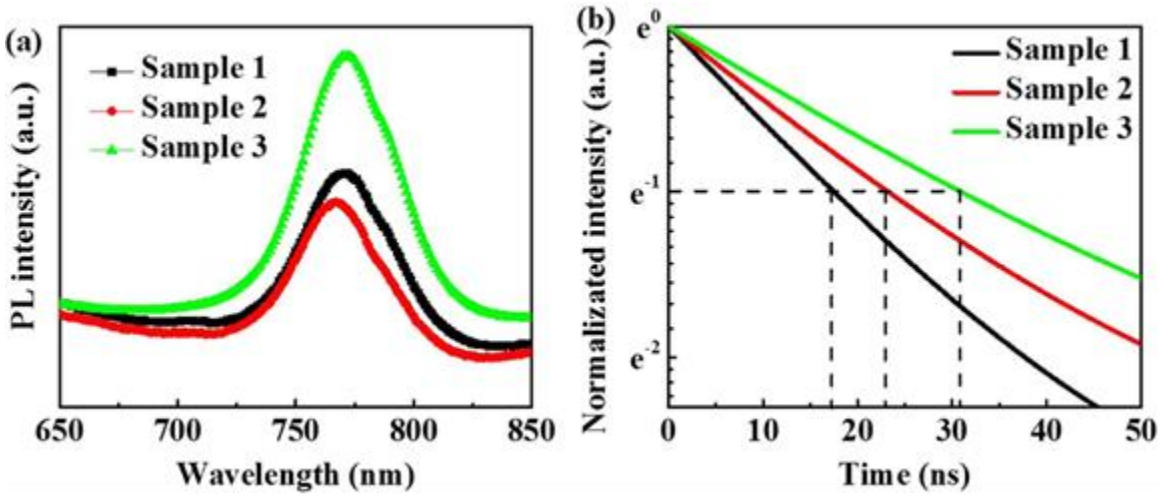

Figure 2-8. (a) Photoluminescence of perovskite samples on FTO glass. (b) TRPL data for perovskite sample.

2.3.2 Photovoltaic performance of perovskite solar cells

After optimizing the compact pinhole free perovskite film in ambient conditions with ~50% humidity, solar cells were fabricated with a device architecture of glass/FTO/compact TiO_2/mesoporous TiO_2/$CH_3NH_3PbI_3$/spiroOMeTAD/Au. To ensure consistency and accuracy, several independent methods were used to investigate photovoltaic performance. Perovskite solar cells often exhibit hysteresis, which relates to the quality of perovskite layer.[83] Poor quality of the perovskite film will result in capacitance between the perovskite and other layers.[84] Power conversion efficiencies were determined by current-voltage characterization by sweeping the voltage from negative to positive (forward scan) and positive to negative values (reverse scan). The J_{sc} of the devices was calibrated against the monochromatic incident photon-to-electron conversion

efficiency. The devices were further tested under maximum power point tracking to investigate the device stability.

Figure 2.9a–2.9c shows the current-voltage curve of the three types of solar cells. Cells fabricated from samples 1 and 2 exhibited significant hysteresis, while little hysteresis was observed from solar cells based on sample 3. A rough, pinhole containing perovskite film leads to capacitance between the perovskite film and other layers, following the charge-discharge taking place at the interface of the perovskite and hole transporting layers.[85] Table 2.2 summarizes the typical device performance based on the above-mentioned structure.

Table 2-2. Parameters of best devices.

Perovskite film	Scan direction	V_{oc} (V)	J_{sc} (mA/cm^2)	FF (%)	PCE_{best} (%)
Sample 1	Forward	0.92	19.01	48.65	8.50
	Reverse	0.92	18.93	57.79	10.06
Sample 2	Forward	0.92	21.30	54.95	10.81
	Reverse	0.96	21.23	62.44	12.77
Sample 3	Forward	1.07	21.06	70.70	15.93
	Reverse	1.08	21.02	70.67	16.01

For the device using sample 1 films, an efficiency of 10.06% was obtained with a V_{oc} of 0.92 V, J_{sc} of 18.93 mA/cm2 and a FF of 57.79 under reverse scan. A poor efficiency of 8.50% with a V_{oc} of 0.92 V, J_{sc} of 19.01 mA/cm2 and FF of 48.65 was achieved under forward scan. The devices show significant photocurrent hysteresis, a noteworthy feature of perovskite trap states, which generate capacitance at the interfaces. Sample 2 device

performance reached a medium level compared to the reference with an efficiency of 10.81% obtained from a V_{oc} of 0.92 V, J_{sc} of 21.30 mA/cm2 and FF of 54.95 under forward scan, while an efficiency of 12.77% with a V_{oc} of 0.96 V, J_{sc} of 21.23 mA/cm2and a FF of 62.44 under reverse scan was achieved. As expected, devices fabricated from sample 3 films exhibited the best performance, namely a champion PCE of 16.01% with V_{oc} of 1.08 V, J_{sc} of 21.02 mA/cm2 and a FF of 70.67 under reverse scan. An efficiency of 15.93% with V_{oc} of 1.07 V, J_{sc} of 21.02 mA/cm2 and a FF of 70.67 under forward scan was achieved. The low FF of solar cells fabricated using sample 1 films can be attributed to the rough nature of the perovskite films. It is widely believed that the FF is the key parameter associated with perovskite device performance, which may be related to carrier recombination at the interface between perovskite films and electron/hole transport layers.[86]

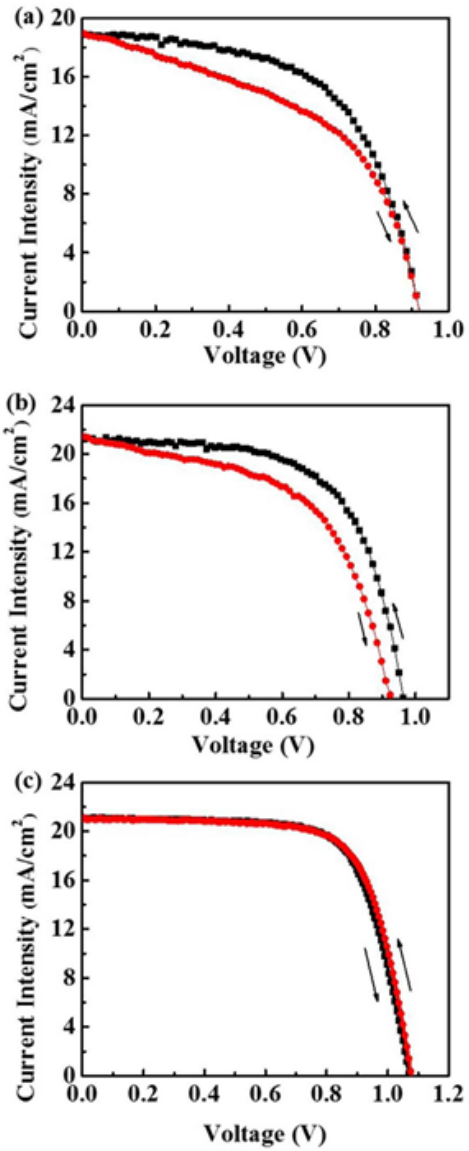

Figure 2-9. J-V curves under both (black line) forward and (red line) reverse scans for best devices. (a) sample 1 (b) sample 2 (c) sample 3.

Figure 2.10 depicts the two-dimensional AFM images which reveal the overall topography of the sample 1, 2, and 3 procedures. The morphology varies significantly with sample preparation procedure and corroborates the FE-SEM results (Figure 2.4). The root mean square (rms) roughness of the three samples are 172 nm, 56.4 nm, and 39.8 nm

respectively. This kind of relative decrease in rms roughness of the perovskite active layer is expected to be advantageous, because it can lead to enhanced V_{oc} as shown by Li et al.[87]

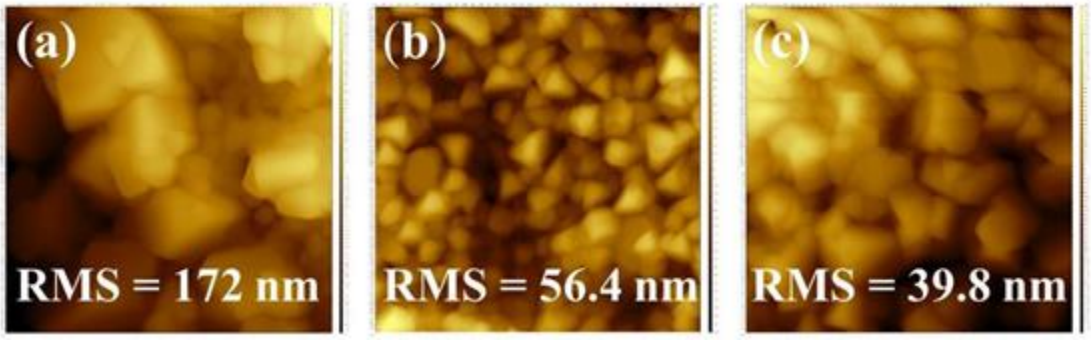

Figure 2-10. AFM images of perovskite films from sample 1 (a), 2(b) and 3 (c).

Figure 2.11a shows IPCE measurement of devices with sample 1 (black line), 2 (red line) and 3 films (green line). The curves start increasing rapidly at around 770 nm, which is related to the optical absorption edge of the perovskite films.[88] Between 450 nm and 800 nm, the absorption profile of devices based on sample 1 is lower than those of sample 2 and sample 3, which may derive from fewer perovskite grains. Between 350 nm and 450 nm, the absorption of the sample 2 device decreased sharply, due to incomplete perovskite grain formation compared to the other two devices. To check the stabilization or saturation point of photocurrent in solar cells with the different perovskite formation protocols, the stabilized power output close to the maximum power point was carried out at the voltage of 0.82 V (sample 3), 0.73 V (sample 2) and 0.68 V (sample 1). The steady-state photocurrent represents the actual power output and is used to accurately characterize the device efficiency. As shown in Figure 2.11b, under simulated AM1.5 G radiation (100 mW/cm^2) and bias voltage at the maximum power point, sample 3 produced a more stable

output current than the other two samples, with the latter showing a diminished current over time.

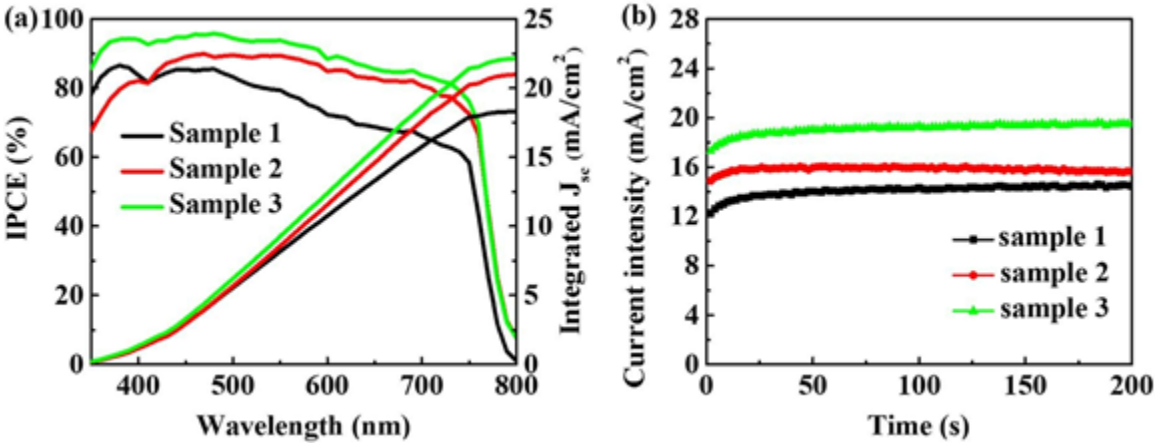

Figure 2-11. (a) IPCE spectra of the devices with different perovskite films. (b) The steady-state current measured at the maximum power point for sample 1 (0.68 V), sample 2 (0.73 V) and sample 3 (0.82 V).

Furthermore, statistical data regarding the photovoltaic parameters for the three solar cell fabrication methods are plotted in Figure 2.12, where the data are obtained from 14 or more cells. Most of the parameters associated with perovskite solar cells fabricated from sample 3 were superior to those obtained from the alternate methodologies, which provides further evidence that better quality perovskite films afforded better device performance.

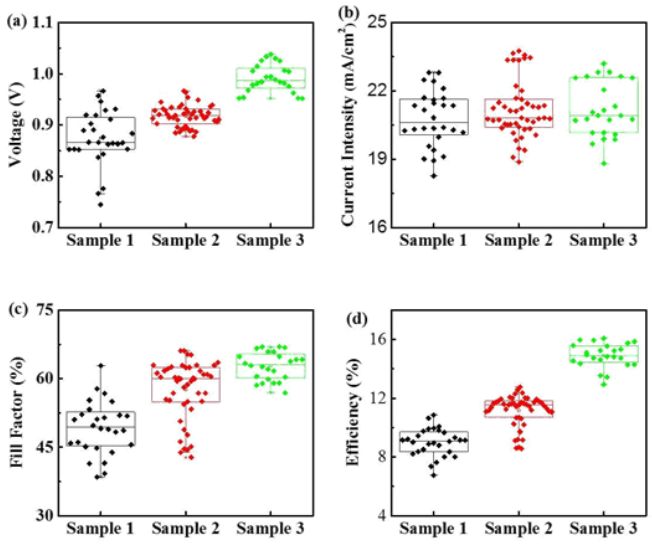

Figure 2-12. Statistical data for efficiency (a), Voc (b), Jsc (c) and FF (d) of three types of devices.

2.4 Conclusion

In summary, a low-cost and simple two-step deposition technique was developed to form microporous PbI_2, based on post-annealed processing in ambient conditions. We investigated the effect of the crystallinity of PbI_2 films on resultant perovskite films and ultimate photovoltaic performance. A power conversion efficiency of 16.01% was achieved with devices fabricated from PbI_2 films having a mesoporous structure. The $CH_3NH_3PbI_3$ film morphology that resulted from the mesoporous precursor was very uniform as confirmed by AFM images. These results demonstrate the importance of morphology control in the PbI_2 phase for high-performance PSCs fabricated under ambient conditions. The simple technique presented here could be used to prepare large area perovskite solar cells in ambient conditions.

CHAPTER 3. MODIFYING PEROVSKITE FILMS WITH POLYVINYLPYRROLIDONE FOR AMBIENT-AIR-STABLE HIGHLY BENDABLE SOLAR CELLS[2]

3.1 Introduction

As certified by the National Renewable Energy Laboratory (NREL), the power conversion efficiency of perovskite solar cells (PSCs) had reached 22.7% when fabricated using an optimized device architecture during the time of this work.[89] The dramatic improvements that led to such high efficiencies were due to the excellent semiconductor properties of AMX_3 perovskite films, such as a high absorption coefficient in the visible region, ambipolar charge transport, and long carrier lifetime.[90-93] The benefits of perovskites are also reflected in their ease of synthesis, that has enabled fabrication of high efficiency devices using various solution deposition techniques, such as spin coating[94], doctor-blade coating[95], slot-die coating[96] or ink-jet printing[97]. Even though solvent[94] and interfacial engineering[98] have led to more homogeneous and relatively defect-free perovskite films, a number of key issues remain. If PSCs are to be technologically and commercially viable, challenges that must be overcome include not only the inherent toxicity of the material due to the presence of lead, but more importantly, limited device life-times associated with susceptibility to ambient air and possible ion migration within the crystal lattice. Thus, for PSCs to be able to generate electricity continuously, long-term

[2] Xiong, Hao, Giovanni DeLuca, Yichuan Rui, Boxin Zhang, Yaogang Li, Qinghong Zhang, Hongzhi Wang, and Elsa Reichmanis. "Modifying Perovskite Films with Polyvinylpyrrolidone for Ambient-Air-Stable Highly Bendable Solar Cells." ACS applied materials & interfaces (2018).

stability is a necessary prerequisite, and further, the crystal structure must be stabilized in order to obtain high efficiency devices with steady output power.[99]

Efforts to address perovskite stability include approaches such as interface modification[100], dopants[101], component selection[102], and encapsulation[103], among others. For instance, Graetzel and coworkers modified the surface of $MAPbI_3$ by spin-coating its precursor solution in the presence of butylphosphonic acid 4-ammonium chloride,[104] while others used a self-assembled hydrophobic fluoroalklsilane coating on the surface of the perovskite films.[105] Very recently, it was reported that the addition of a polymer into the precursor solution, in a one-step deposition process, can tune perovskite morphology thereby enhancing device stability in air. Examples of polymers that have been explored include polyethylene glycol (PEG)[106], phenethylamine[107], polyurethane[108], *etc*. However, incorporation of these polymers into the film had a negative impact on the $MAPbI_3$ perovskite film morphology, because of steric hindrance induced by the polymer used.

Polyvinylpyrrolidone (PVP) is an alternative polymer that has been investigated in efforts to stabilize the active layer, however, the resultant perovskite films continued to have an unacceptably high number of defects.[109-111] PVP is an attractive additive because of its strong polar carbon-oxygen double bond, which is expected to interact with the perovskite precursor components and thereby stabilize the perovskite crystal structure. Here, we demonstrate how commercial PVP, coupled with optimization of the deposition parameters, provides for defect free perovskite films. PVP K-30 (M_w = 40,000 g/mol; K-value of viscosity for a 1% solution ~30) was directly introduced into the perovskite precursor solution, and through optimization of the perovskite precursor to additive ratio, was shown to facilitate formation of highly compact and uniform perovskite films, which

in a device configuration exhibited efficiencies in the range of 16%. The PVP-perovskite system displayed excellent stability upon storage in ambient air (relative humidity ≥ 60%) and further, was shown to provide a platform for flexible perovskite device fabrication.

3.2 Experimental section

3.2.1 Materials and reagents

All materials were purchased from Sinopharm Chemical Reagent Co., Ltd. and used as received, with the exception of the following: $CH(NH_2)_2I$ (FAI), CH_3NH_3Br (MABr), and Spiro-MeOTAD (2, 2', 7, 7'- tetrakis (N, N – di (4 - methoxyphenyl) amine) - 9, 9'-spirobifluorene, purity ≥ 99.5 %) were purchased from Xi'an Polymer Light Technology Corp. Fluorine doped tin oxide (FTO) coated glass (14 Ω square^{-1},) and indium tin oxide (ITO) coated PET (Polyethylene terephthalate) (7 Ω square^{-1}) were purchased from Nippon Sheet Glass Co., Ltd. Polyvinylpyrrolidone (PVP, M_w=40,000 g/mol) was purchased from Sigma-Aldrich.

3.2.2 Perovskite device fabrication

FTO conductive glass was washed through sequential ultrasonic treatment in detergent, acetone, ethanol, and deionized water, and was then treated in an O_2 plasma for 30 min (DT-01, Suzhou Omega Machinery Electronic Technology Co., Ltd.). Low temperature SnO_2 electron transport layers were prepared according to the method described by Chattopadhyay.[112] $SnCl_2 \cdot 2H_2O$ (22.56 mg) was dissolved in 10 ml isopropyl alcohol, and the resulting solution was stirred at reflux temperature (70 °C) for one hour and then aged for 6 h to form the sol. A volume of 50 μl of nanoparticle SnO_2 sol was spin-

coated onto either an FTO glass or ITO/PET substrate, and then sintered on a hotplate at 90 °C for 3 h.

PbI_2 (507 mg, 1.1 mmol), $PbBr_2$ (73.4 mg, 0.2mmol), FAI (172 mg, 1.0 mmol), and CH_3NH_3Br (22.4 mg, 0.2 mmol) with 0-12 wt% PVP were added to 1.0 mL of dimethylformamide and dimethylsulfoxide (4:1, v/v), and the resulting mixture was stirred at 80 °C until all components were dissolved. The resulting hybrid perovskite precursor solution was spin-coated onto SnO_2/FTO or SnO_2/ITO substrates at 3000 rpm for 30 s using a one-step method. During spin-coating, the samples were washed with toluene, a non-polar solvent. The perovskite films were then annealed at 110 °C for 10 min on a hotplate while covered by a petri dish to further remove residual solvents. A spiro-OMeTAD solution (25 μL) was then spin-coated onto the as prepared perovskite film at 4000 rpm for 30 s. All operations were carried out in ambient air without controlling relative humidity.[113] Finally, the devices were coated with an 80 nm gold electrode by evaporation through an aperture mask in a vacuum chamber. The active area of the perovskite device was 0.16 cm^2.

3.2.3 Characterization

The perovskite film was characterized by X-ray diffraction (XRD) (Model D/max 2550V, Rigaku Co. Tokyo, Japan) by using Cu Kα (λ=1.5406 Å) radiation. The morphology of the resultant perovskite film was observed by using field-emission scanning electron microscopy (FESEM, Model S-4800, Hitachi, Japan). Tapping mode atomic force microscopy (AFM) imaging was carried out using a Multimode NanoScope IV system (Veeco, Santa Barbara, CA) at a scanning range and speed of 2μm and 3.001 Hz,

respectively. Steady-state photoluminescence (PL) spectra were acquired with a FLS920 transient optical spectrometer (Edinburgh Instruments, UK). Ultraviolet photoelectron spectroscopy characterization of the PVP-perovskite film was performed using a monochromatic He I light source (21.2 eV) and a VG Scienta R4000 analyzer. The photocurrent density-voltage (J-V) curves of the PSCs were acquired using a Keithley 2400 Source Measuring Unit. A solar simulator (Model 96160 Newport Co., USA) equipped with a 300 W Xenon lamp was used as a light source, where the light intensity was adjusted using an NREL-calibrated Si solar cell with KG-1 filter for approximating the AM 1.5G one sun light intensity. The cell performance parameters, including short-circuit current density (J_{sc}), open-circuit voltage (V_{oc}), fill factor ($FF=Pmax/(J_{sc}V_{oc})$), and photoelectron conversion efficiency ($h\ (\%)=J_{sc}*V_{oc}*FF/\text{total incident energy}\times100$), were measured and calculated from the J-V characteristics. The incident-photon-to-current conversion efficiency (IPCE) spectra were measured as a function of wavelength from 300 to 800 nm using a specially designed IPCE system (Newport Co., USA). Measurement and storage of the devices were performed in ambient conditions and without encapsulation.

3.3 Results and discussion

3.3.1 PVP-Perovskite film formation

While a one-step perovskite deposition method generally leads to films comprised of large, cuboidal grains;[114] upon storage in humid (relative humidity greater than 60%) environments, the perovskite layers decompose rapidly. It was recently postulated that water catalyzes the decomposition of perovskite through the reversible reactions shown below:[115]

$$\left[CH_3NH_3{}^+PbI_3\right]_n + H_2O \rightleftarrows \left[(CH_3NH_3{}^+)_{n-1}(PbI_3)_n\right][H_3O^+] + CH_3NH_2 \quad (1)$$

$$\left[(CH_3NH_3{}^+)_{n-1}(PbI_3)_n\right][H_3O^+] \leftrightarrows HI + PbI_2 + \left[(CH_3NH_3{}^+)(PbI_3)_{n-1} + H_2O\right] \quad (2)$$

Here, we describe the preparation of perovskite films with not only enhanced stability, but also flexibility, under ambient conditions using PVP as an additive, coupled with optimization of the deposition parameters. PVP was selected because of its polar characteristics that derive from the carbon-oxygen double bond (carbonyl group: C=O) present on each monomer unit. The C=O group was expected to interact with other polar species present in the perovskite precursor solution through hydrogen bonding, thereby facilitating incorporation of the polymer into the active material matrix during film deposition. Mechanistically, the long chain PVP was expected to form a framework around the perovskite crystals, thus creating a barrier to moisture penetration into the inorganic lattice. In addition, incorporation of the flexible polymer might allow some latitude in bending devices fabricated on plastic substrates, thereby maintaining performance.

As evidenced by the FE-SEM surface and cross section images (Figure 3.1a-3.1d, Figure 3.1i-3.1l, respectively), perovskite morphology changed dramatically upon incorporation of PVP, and notably, the PVP modified layers appeared more uniform and homogeneous. As presented in Figure 3.1e-3.1h, the particle/grain size changed when PVP was added to the precursor solution; for 0, 4, 8 and 12 wt% PVP-perovskite films, the grain sizes were *ca.* 400 nm, 100 nm, 210 nm, and 350 nm respectively. In addition, in the presence of PVP, the perovskite films exhibited a narrower particle size distribution. While in all cases, inclusion of PVP afforded more homogeneous structures, when the

concentration of PVP exceeded 12 wt%, the film appeared to develop large voids between individual perovskite grains. This is attributed to the transformation of the perovskite crystals derived from inductive effects[116] and the space location-obstruct effect[117] of PVP (*vide infra*). Atomic force microscopy (AFM) analysis (Figure 3.2a-3.2d) provided insight into the surface roughness of as prepared films (Sq, root mean square height). Whereas the parent perovskite presented a Sq value of 19.34 nm (Figure 3.2a), that for 4.0 wt% PVP (Figure 3.2b) was only 7.96 nm, meaning that the surface was much smoother. For comparison, Sq for 8 and 12 wt % PVP-perovskite was 14.32 nm (Figure 3.2c) and 17.39 nm (Figure 3.2d), respectively. The AFM results were consistent with SEM observations.

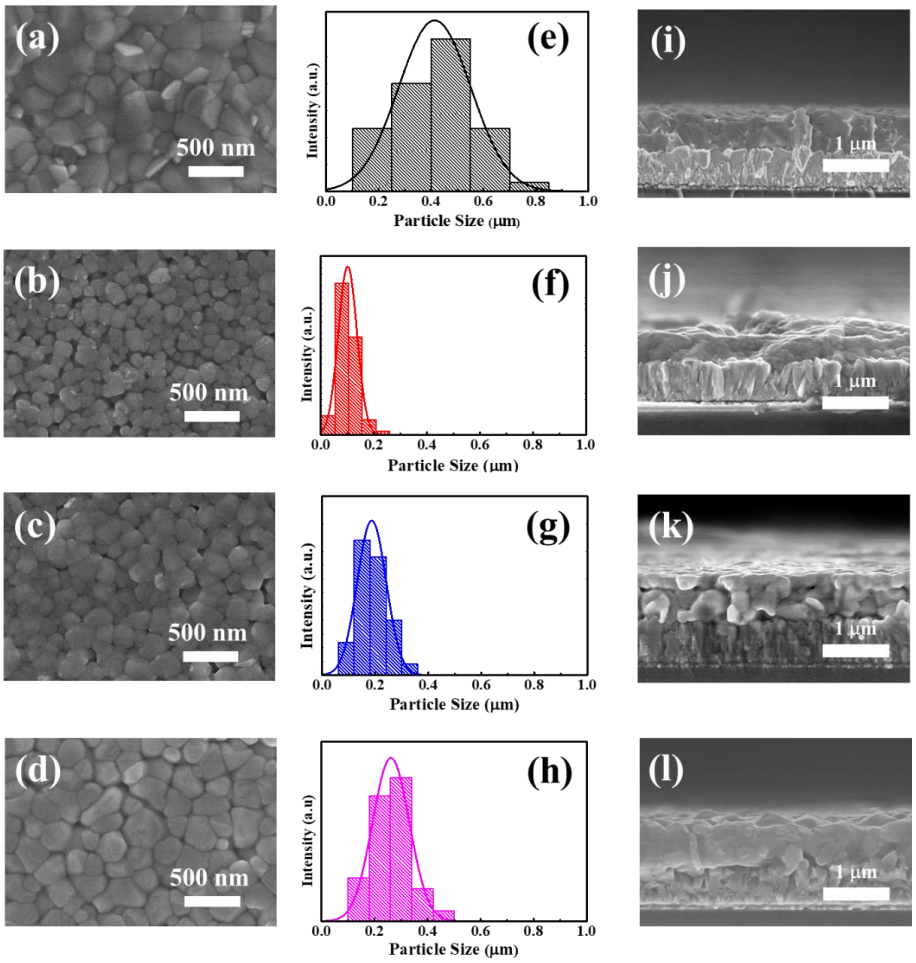

Figure 3-1. Surface and Cross-sectional FE-SEM image of perovskite films without PVP (a, i) and with PVP at 4 wt% (b, j), 8 wt% (c, k), and 12 wt% (d, l) concentrations. Particle size and distribution for corresponding images (e-h).

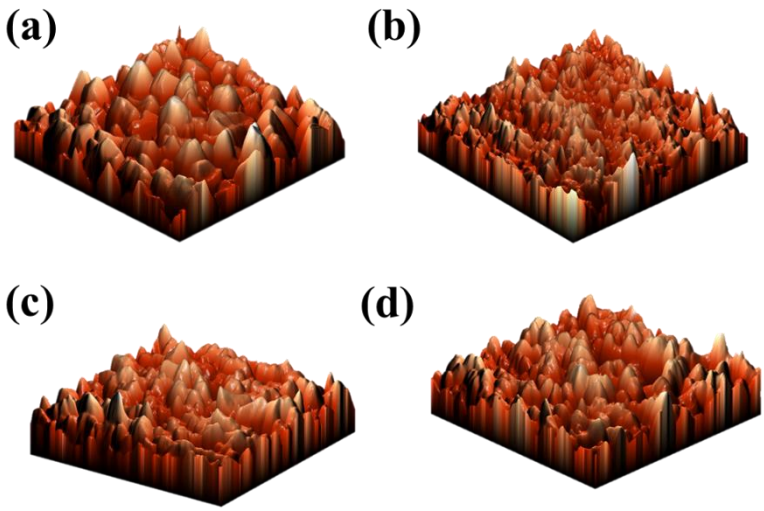

Figure 3-2. AFM images of 0 wt% (a), 4 wt% PVP (b), 8 wt% (c) and 12 wt% (d) PVP-perovskite films.

From examination of the characteristic XRD patterns presented in Figure 3.3a, 0 wt%, 4 wt%, and 8 wt% PVP-perovskite grains on FTO glass were well-crystallized, presenting signature peaks at 2θ = 20.08° (200), 28.35° (220) and 40.81° (400). However, several different peaks were observed in the diffraction patterns owing to the varying PVP content. With increasing PVP concentration, the characteristic 2θ perovskite peak at 14.39º underwent a shift to a slightly lower value, as seen in the upper inset. This shift is indicative of residual stress between PVP and the perovskite crystals, which is a phenomenon found in other materials.[118] At lower PVP concentrations, this stress did not significantly influence overall film morphology. However, for PVP content above 12%, diffraction peaks attributed to residual PbI_2 and stress induced damage to the crystal structure were observed at 2θ ~12.6º (001). Conceivably, the small feature observed at 12.6° originates from the non-perovskite phase of $FAPbI_3$ that begins to form at higher concentrations of

PVP. The XRD analysis is consistent with the morphologies identified by SEM (Figure 3.1): note the lighter, roughened edges of the perovskite grains in Figure 3.1d.

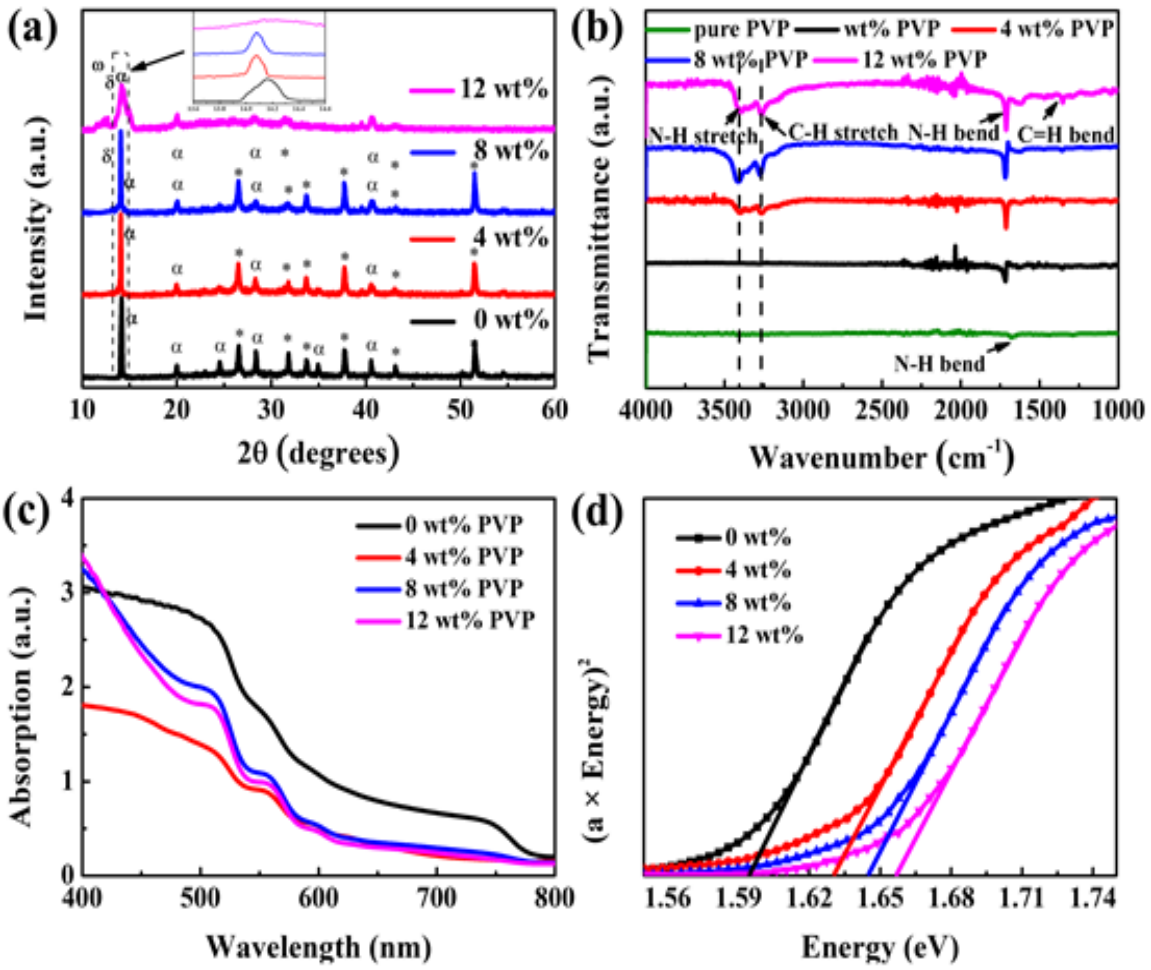

Figure 3-3. (a) XRD patterns of PVP-perovskite films. The diffraction peaks originating from the perovskite phase, non-perovskite phase, unreacted PbI2 and the FTO substrate are marked by α, δ, ω, and * respectively. (b) FT-IR spectra of PVP-perovskite films, and pure PVP (green); (c) UV-Vis absorbance data of 0 PVP-perovskite films; and (d) Tauc plots of 0 wt% (black), 4 wt% (red), 8 wt% (blue), and 12 wt% (magenta) PVP-perovskite films.

FT-IR spectroscopy was used to investigate the presence of chemical interactions between PVP and the perovskite. Spectra within the range of 4000-1000 cm^{-1} for pure PVP,

pristine perovskite and PVP-perovskite films with varying concentrations of PVP are presented in Figure 3.3b. The higher polymer concentration sample was selected for FTIR analysis to enable identification of interactions and band shifts. The main spectral features to be considered in the pure PVP film are the tertiary amine group deformation modes at 1458 cm^{-1} and the carbonyl group vibration at 1676 cm^{-1}.[119] The C-N bending vibration appears at 1716 cm^{-1} in pristine perovskite; however, in the presence of PVP, the C-N band shifts to lower wavenumbers as the PVP concentration is increased. This observed shift may derive from interactions between perovskite C-N and PVP C=O groups. While peaks associated with C-N and N-H stretching are not obvious in the pristine perovskite film; the PVP C-H and N-H vibrational modes appear as intense bands at 3500-3000 cm^{-1} in PVP doped perovskite films. UV-Vis spectral analysis (Figure 3.3c) demonstrated that the incorporation of PVP into the perovskite layer led to a slight decrease in the absorption of visible light, where the parent perovskite exhibited the highest absorbance. The bandgap was calculated by applying Kubelka-Munk (K-M) analysis to the measured diffuse absorption spectra as follows:[120]

$$(\alpha h\nu)^2 = C(h\nu - E_g)$$

Where α represents the absorption coefficient, *h* represents Planck's constant, ν is the frequency of light, E_g is the bandgap of the material, and C is the proportionality constant - not related to E_g. The Tauc plot presented in Figure 3.3d was used to determine the perovskite bandgap as a function of PVP concentration. While the pristine perovskite bandgap was calculated to be 1.60 eV, incorporation of up to 12 wt% PVP led to a gradual increase in bandgap to 1.65 eV (Table 3.1). This change is attributed to the Pb^{2+} 4f core-level peak-shift, which dominates the perovskite bandgap.[121]

Table 3-1. Bandgap values calculated from UV-Vis and ultraviolet photoelectron spectroscopy data.

PVP concentration (wt%)	Bandgap (eV)	Valence band (eV)	Conduction band (eV)
0	1.60	-5.1	-3.5
4 wt%	1.63	-5.2	-3.57
8 wt%	1.645	-5.3	-3.655
12 wt%	1.65	-4.6	-2.95

Ultraviolet photoelectron spectroscopy (UPS) was used to evaluate the effect of PVP on perovskite electronic properties.[122] Notably, incorporation of PVP led to a significant decrease in energy of the valence band (EVB) from -5.1 eV to -5.3 eV, as measured by UPS, using He(I) emission ($h\nu$ =21.2 eV) as the light source (Figure 3.4). The VB edge energy (EVB) values, with reference to the vacuum level, were calculated to be -5.1 eV for the parent perovskite, and -5.2 eV, -5.3 eV and -4.6 eV for the 4, 8 and 12 wt% PVP-perovskites, respectively. The conduction band edge energies (ECB) were then determined from the E_g and EVB values; ECB for the parent was -3.5 eV, a value that is slightly deeper than that of the 4 and 8 wt% PVP-perovskite samples (-3.6 eV, -3.7eV). The incorporation of 12 wt% PVP afforded a material having an ECB value of -2.95 eV, pointing to the existence of a non-perovskite phase. In principle, the deeper perovskite conduction band could be expected to enhance charge transfer from the perovskite to the electron transport layer.[123]

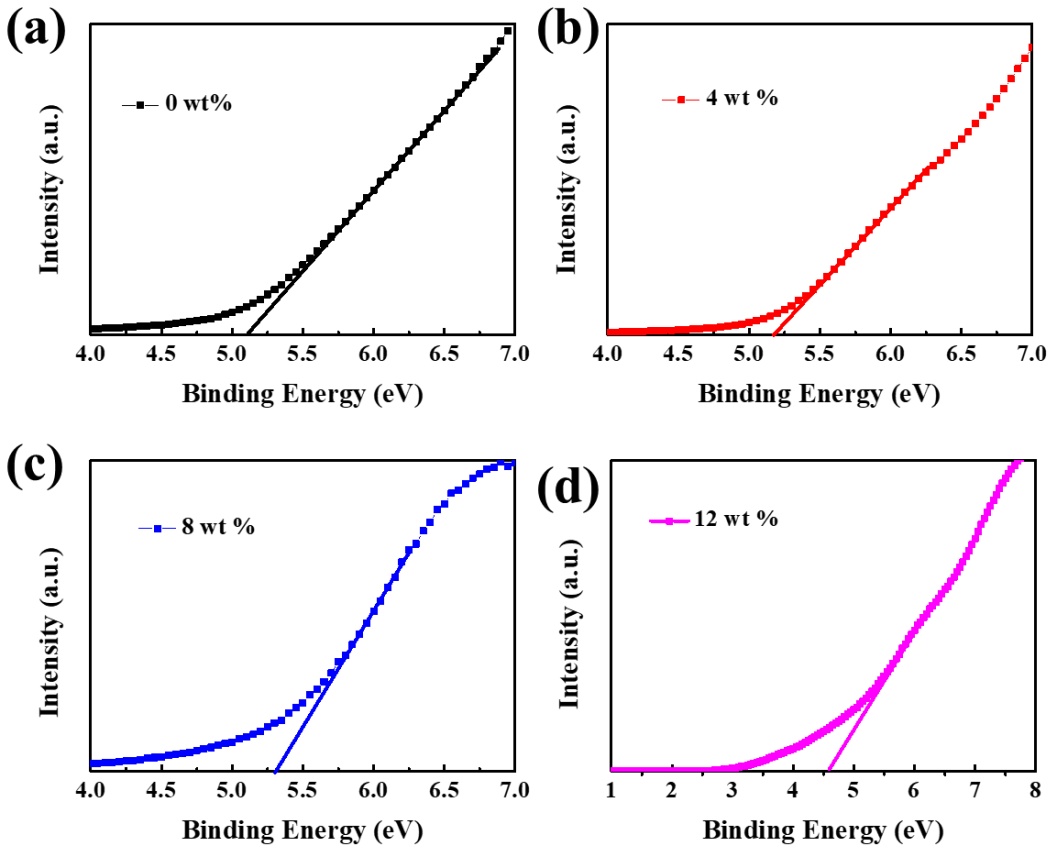

Figure 3-4. Valence band spectra of perovskite films with 0 wt% (black), 4 wt% (red), 8 wt% (blue) and 12 wt% (magenta) PVP on silica wafer.

XPS analysis was used to further investigate the changes in binding energy of the perovskite core level peaks in the presence and absence of PVP. The survey spectra of perovskite prepared with varying PVP concentration is presented in Figure 3.5.

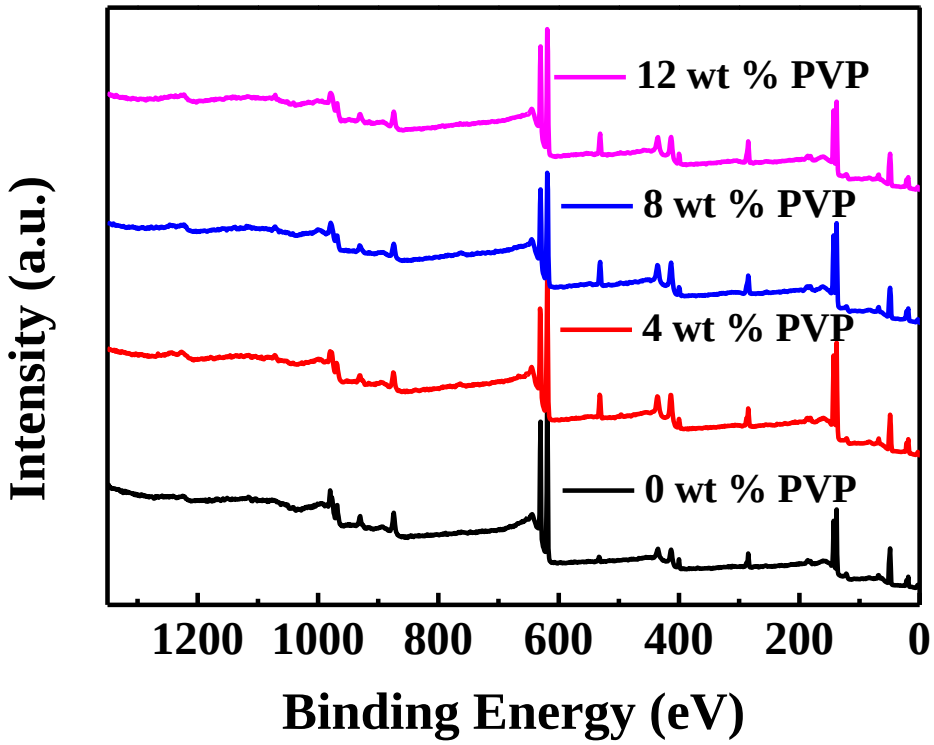

Figure 3-5. Survey XPS spectra of 0 wt% (black), 4 wt% (red), 8 wt% (blue), and 12 wt% (magenta) PVP-Perovskite samples.

All of the samples were prepared on silicon substrates. All the fabricated films show nearly the same XPS peaks and intensities, indicating that the components present in all of the films are the same. The iodine, oxygen, nitrogen, carbon, lead and bromide atom binding energies are shown in Figure 3.6a-3.6f. The spin-orbit split components of $I3_{d3/2}$ and $I3_{d5/2}$ are shifted slightly to lower energy (Figure 3.6a). The peak height of the $I3_d$ peaks (arising from the PbI_6 octahedra) decreases slightly with increasing PVP content. Abnormal deviations can also be observed in the split components of $O1_s$, $N1_s$, $C1_s$, $Pb4_f$ and $Br3_d$ (Figure 3.6b-3.6f), all of which support the premise that the PbI_6 octahedra were disrupted by PVP chains and is consistent with XRD analysis.

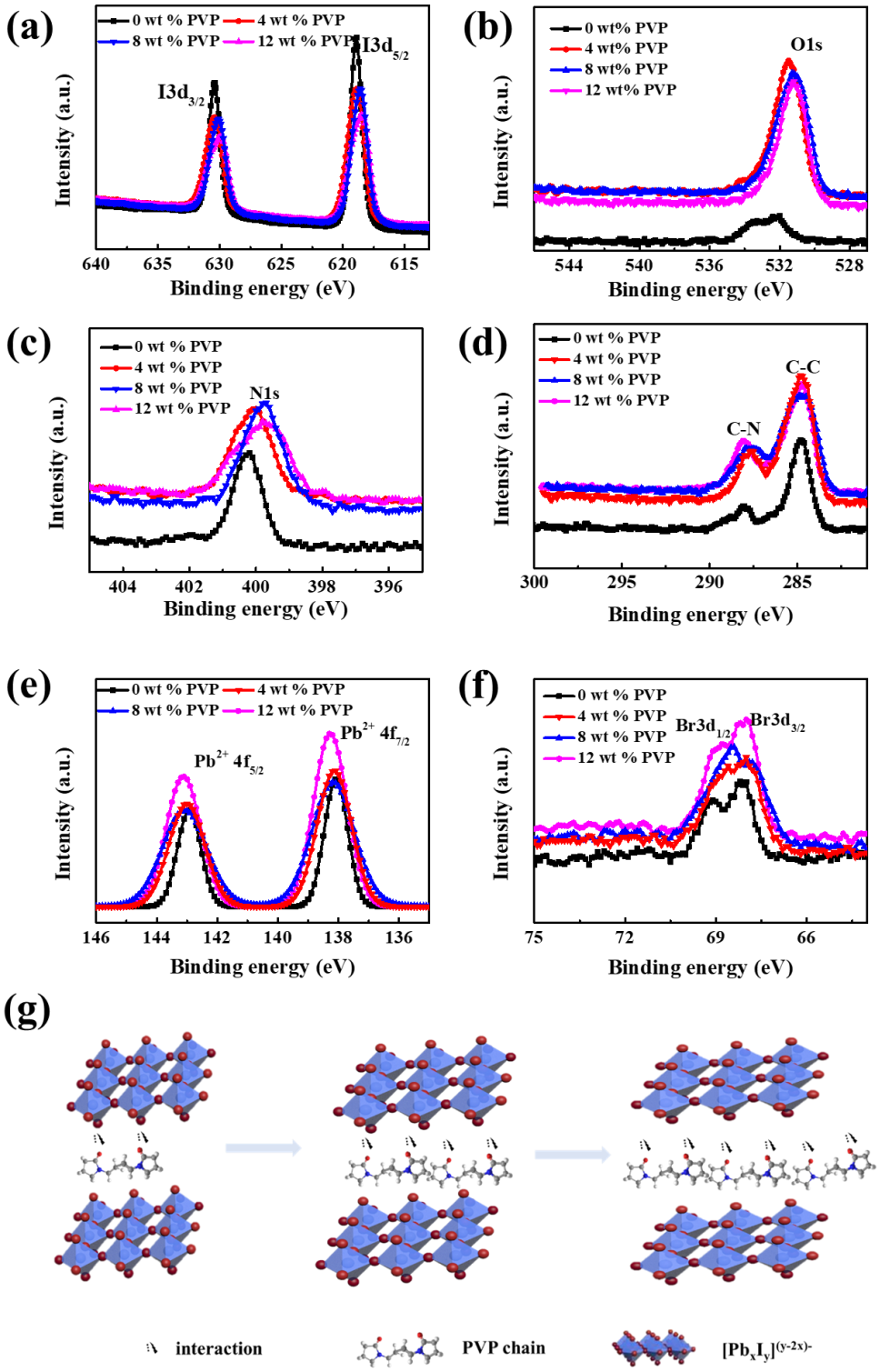

Figure 3-6. Core-level XPS spectra for 0 wt% (black), 4 wt% (red), 8 wt% (blue), and 12 wt% (magenta) PVP-perovskite films: (a) I3d, (b) O1s, (c) N1s, (d) C1s, (e) Pb4f and (f) Br3d. (g) Schematics of the variation of perovskite crystals with PVP concentration increasing.

Even more remarkably, the spin-orbit split components of pristine perovskite show low strengths at 533.3 eV and 532 eV for $O1s_{2/2}$ and $O1s_{1/2}$, respectively. The peak at 533.3 eV corresponds to adsorbed molecular water.[124] With PVP doping, the peak at 533.3 eV is no longer present, which suggests that PVP serves as a barrier to protect the perovskite film from adventitious water. At the same time, the intensity of the peak near 532 eV corresponding to the C=O group has increased. Slightly shifted peaks were observed in the doped perovskite, which may derive from hydrogen bonding interactions between PVP and perovskite.[120] The experimental $Pb4_f$ signal is presented in Figure 3.6e. The spin-orbit splitting between the $Pb4_{f7/2}$ and $Pb4_{f5/2}$ lines of pristine perovskite appeared at 138.1 eV and 143 eV, respectively. However, the Pb^{2+} lines of the doped perovskite shifted to higher binding energies. The shift of the $Pb4_f$ levels can be attributed to decreased electron cloud overlap between the lead and iodide atoms, which may help account for the observed slight increase in bandgap (*vide infra*).[121]

To further explain the phenomenon, a schematic of the interactions between perovskite crystals and the PVP long chain is presented in Figure 3.6g. With increased PVP concentration, the PbI_6 octahedra become stretched. Up to a PVP concentration of about 8 wt%, the $[Pb_3I_8]^{2-}$ octahedra can tolerate the distortions. However, as PVP content continued to increase, the $[Pb_3I_8]^{2-}$ crystal lattice rearranged to form octahedral $[PbI_6]^{4-}$, resulting in the formation of a non-perovskite phase. The presence of $[PbI_6]^{4-}$ also impacts the absorption edge of the samples, as discussed below.[125]

Photoluminescence (PL) spectroscopy provided insightful information on the charge carrier extraction properties of solar cells fabricated from pure and PVP-containing perovskite samples. An obvious change in PL intensity was observed for PVP-perovskite

films vs. the parent (Figure 3.7a). Specifically, the higher PL intensity for the 4 wt% and 8 wt% PVP-perovskite samples suggests that these films possess fewer defects. The decreased photoluminescence intensity obtained for the 12 wt% counterpart points to an increase in defect density as PVP content is increased above 8 wt%. Time-resolved PL (TRPL) spectra demonstrated that PVP content impacts photoluminescence life-time, where the 8 wt% sample exhibited a notably longer lifetime than any of the alternatives (Figure 3.7b). Combined, the PL and TRPL results suggest that at low levels (below about 8 wt%), the incorporation of PVP into the perovskite crystal structure can facilitate formation of more uniform films having fewer defects.

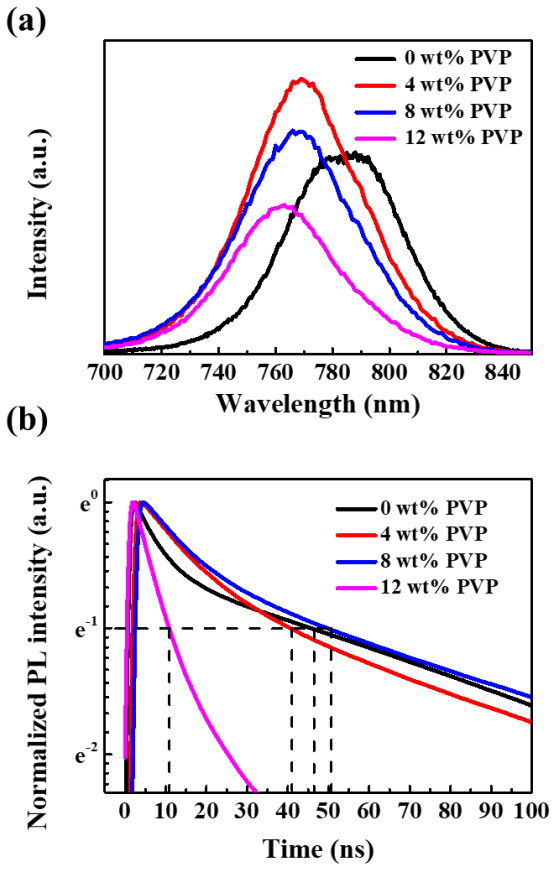

Figure 3-7. (a) Photoluminescence of PVP-Perovskite samples on the glass. (b) Time Resolved Photoluminescence (TRPL) data for 0 wt% (black), 4 wt% (red), 8 wt% (blue), and 12 wt% (magenta) PVP- Perovskite samples.

3.3.2 Device fabrication and characterization

Perovskite-based solar cells were fabricated using optimized process conditions under ambient conditions. The device architecture was comprised of either glass/FTO/compact SnO_2/perovskite/spiro-OMeTAD/Au, or PET/ITO/compact SnO_2/perovskite/spiro-OMeTAD/Au. Figure 3.8a presents a sketch of the band alignment scheme for a photovoltaic device fabricated using the hybrid active material. To avoid hysteresis, which is in part a function of the quality of the interface between the perovskite and electron transport layers, SnO_2 nanoparticles were used as the electron transport layer.[126-128] Since typically the SnO_2 nanoparticle deposition temperature is *ca.* 200 °C, a sol-gel method was developed to enable process temperatures below 185 °C in order to fabricate an SnO_2 electron transport layer suitable for plastic substrates.

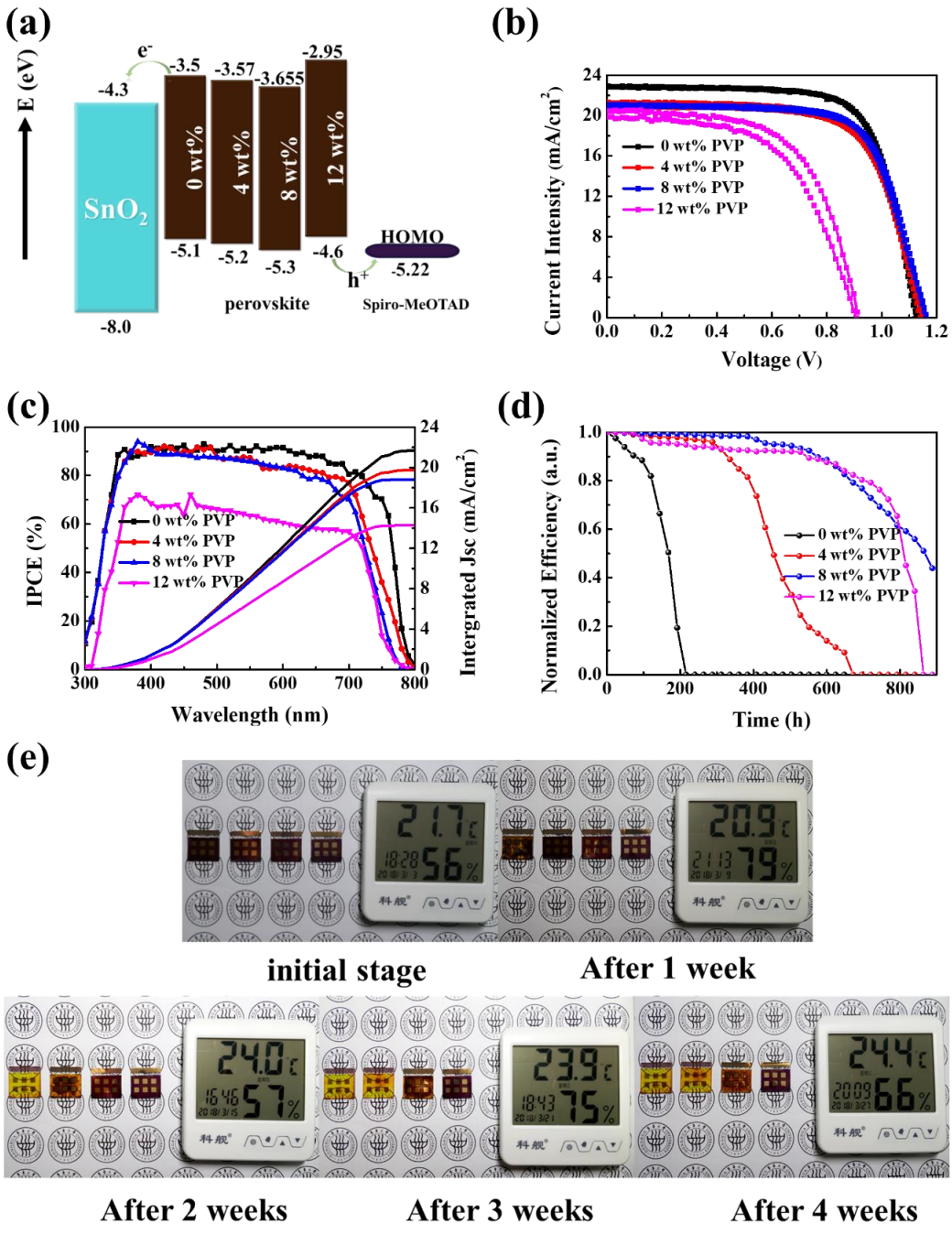

Figure 3-8. (a) Schematic energy level diagrams of the SnO2 nanoparticles, 0 wt%, 4 wt%, 8 wt%, 12 wt% PVP doped perovskite and spiro-MeOTAD; (b) J−V curves of the typical devices under AM 1.5G illumination. (c) Corresponding EQE responses (left axis) and integrated current densities (right axis) of the devices containing the perovskite films with and without PVP. (d) Normalized efficiency as a factor of time; (e) Photograph of perovskite solar cell stability with varying concentrations of PVP in ambient conditions. From left to right 0 wt%, 4 wt%, 8 wt%, and 12 wt% PVP-perovskite devices.

Figure 3.8b presents the current-voltage curves of the pristine and PVP containing perovskite solar cells, and the data are tabulated in Table 3.2. Furthermore, statistical data regarding the photovoltaic parameters are plotted in Figure 3.9. Cells fabricated from the 0 wt%, 4 wt%, and 8 wt% PVP-perovskites exhibited little hysteresis, while significant hysteresis was observed for cells fabricated with 12 wt% PVP-perovskite. The pristine device exhibited efficiencies of 18.42 % and 18.38%, under reverse and forward scans, respectively; with corresponding V_{oc} of 1.127 V and 1.124 V, J_{sc} of 22.8 mA/cm^2 and 22.9 mA/cm^2 and FF of 71.43 % and 71.7 %. Upon incorporation of 4 wt% PVP, device efficiency in the forward and reverse directions decreased slightly to 16.7% and 16.41%, while the corresponding V_{oc}, J_{sc}, and FF values were 1.152 V and 1.141 V, 21.2 mA/cm^2 and 20.9 mA/cm^2, and 68.73 % and 68.07 %. The 8 wt% PVP-perovskite device exhibited negligible hysteresis, with an efficiency of 17.04% and 17.06%, with a V_{oc} of 1.16 V and 1.162 V, J_{sc} of 21 mA/cm^2 and 21.05 MA/cm^2, FF of 70.01 % and 69.69 % under reverse scan and forward scan, respectively. The excellent performance can be ascribed to the matched bandgap and defect-free crystals, which is in accord with the structural analysis above.

As expected from the materials characterization results, devices fabricated from 12 wt% PVP-perovskite films exhibited a significant decline in performance, namely a PCE of only 11.31 % under reverse scan and 10.18% under forward scan. V_{oc}, J_{sc} and FF were similarly negatively affected. Presumably, the low FF of 56.84 obtained for the 12 wt% PVP containing cells can be attributed to the rough perovskite morphology. It is widely believed that the key parameter associated with perovskite device performance is the FF,

which may be negatively affected by carrier recombination at the interface between the perovskite and the electron/hole transport layers due to perovskite crystal degradation.[129]

Figure 3.8c presents the IPCE data for the devices studied here. The wavelength at which the IPCE curves experience a rapid rise is consistent with the absorption edge data discussed above: for the parent perovskite, the increase appears at around 780 nm, while for cells fabricated with 4, 8 and 12 wt% PVP-perovskite, IPCE begins to increase at about 770 nm, 760 nm and 750 nm, respectively. Between 450 nm and 700 nm, the absorption profile of devices based on pristine perovskite is higher than those of the doped perovskites, which may derive from perovskite grain size.[130] Between 350 nm and 450 nm, the absorption of the 12 wt% device decreased sharply, likely due to incomplete perovskite grain formation compared to the other three devices.[131]

Data associated with the moisture sensitivity of the perovskite devices investigated here are presented in Figure 3.8d-3.8e. The parent perovskite underwent a steady decrease in efficiency from 18 % to ~1 % within 200 hours. Notably, the devices fabricated with the PVP-modified perovskite film exhibited enhanced resistance to moisture present in the ambient conditions. Incorporation of 8 wt% PVP into the perovskite layer allowed fabrication of devices that retained 80% of their original efficiency for over 600 hours under ambient conditions with 60% relative humidity. Although the initial efficiency of the 12 wt% PVP-perovskite devices is lower than the other analogs, the normalized efficiency is more stable in a humid environment, which is presumed to be directly related to protection of the perovskite by PVP.

Table 3-2. The optimized Photovoltaic performance parameters of the devices under standard AM 1.5G illumination (100 mW cm−2).

Device		V_{oc} (V)	J_{sc} (mA/cm^2)	FF %	PCE %
0 wt%	Forward	1.124	22.9	71.43	18.38
	Reverse	1.127	22.8	71.7	18.42
4 wt%	Forward	1.141	20.9	68.73	16.41
	Reverse	1.15	21.2	68.07	16.7
8 wt%	Forward	1.16	21	70.01	17.06
	Reverse	1.162	21.05	69.69	17.05
12 wt%	Forward	0.903	19.83	56.84	10.18
	Reverse	0.914	20.50	60.34	11.31

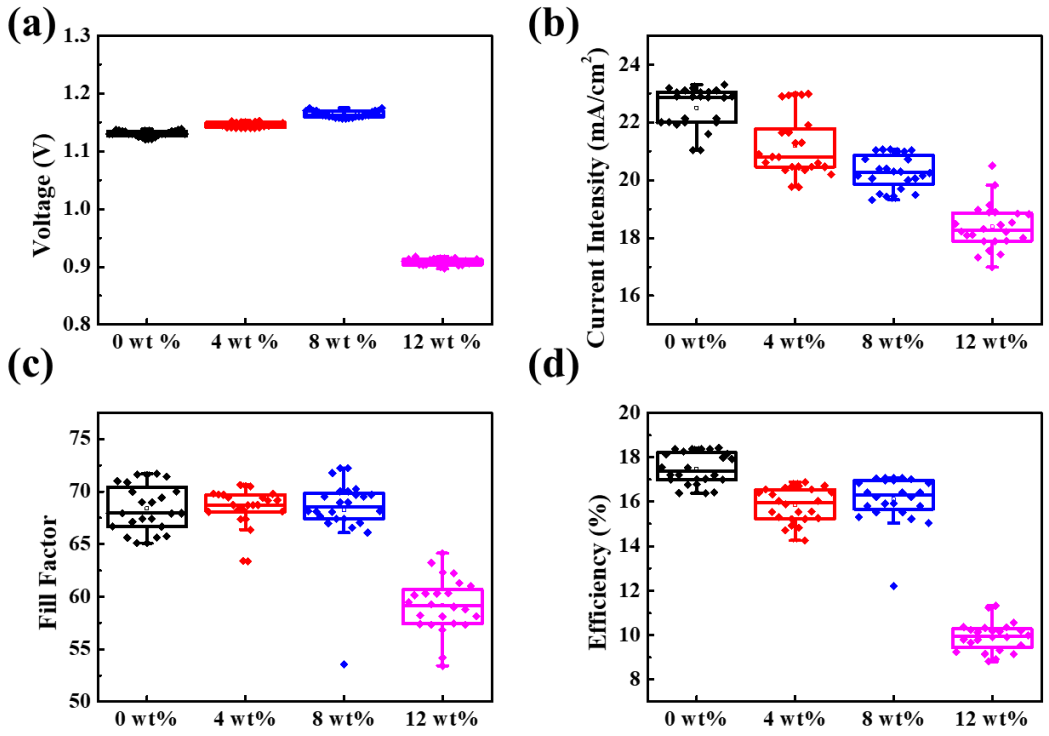

Figure 3-9. Statistical data 0 wt% (black), 4 wt% (red), 8 wt% (blue), and 12 wt% (magenta) for (a) Voc, (b) Jsc, (c) FF, and (d) PCE.

3.3.3 Flexibility and bendability testing

Given the superior performance of the perovskite comprising 8 wt% PVP, that composition was used to explore the impact of the incorporation of PVP into the perovskite lattice on the flexibility of the active layer. The top-view SEM images of the parent and PVP-perovskite films fabricated on an ITO/PET substrate and subjected to mechanical bending (200 times with bending radius of 0.5 cm) are presented in Figure 3.10. The parent perovskite film (Figure 3.10a) exhibited evidence of fracturing at the grain boundaries upon bending 200 times (Figure 3.10b). In contrast, the 8 wt% PVP-perovskite films (Figure 3.10c) displayed a uniform morphology that did not appear to be compromised (Figure 3.10d). Conceivably, the incorporation of PVP into the crystalline film forms a polymer network, effectively improving the mechanical properties of the device.[108] Furthermore, steady-state PL spectra (Figure 3.10e and 3.10f) of the corresponding perovskite films on PET/ITO before and after bending 200 times were also analyzed. The PL intensity of the 8 wt% PVP-perovskite film (Figure 3.10f) prepared on PET/ITO was similar to that of pristine material (Figure 3.10e) prior to mechanical bending. After bending 200 times, the PVP-perovskite maintained its PL intensity, while that of the pristine film decreased. These results strongly suggest that the incorporation of PVP serves to reduce surface defects and importantly, for envisioned flexible PSC applications, instills the films with improved mechanical performance attributes.

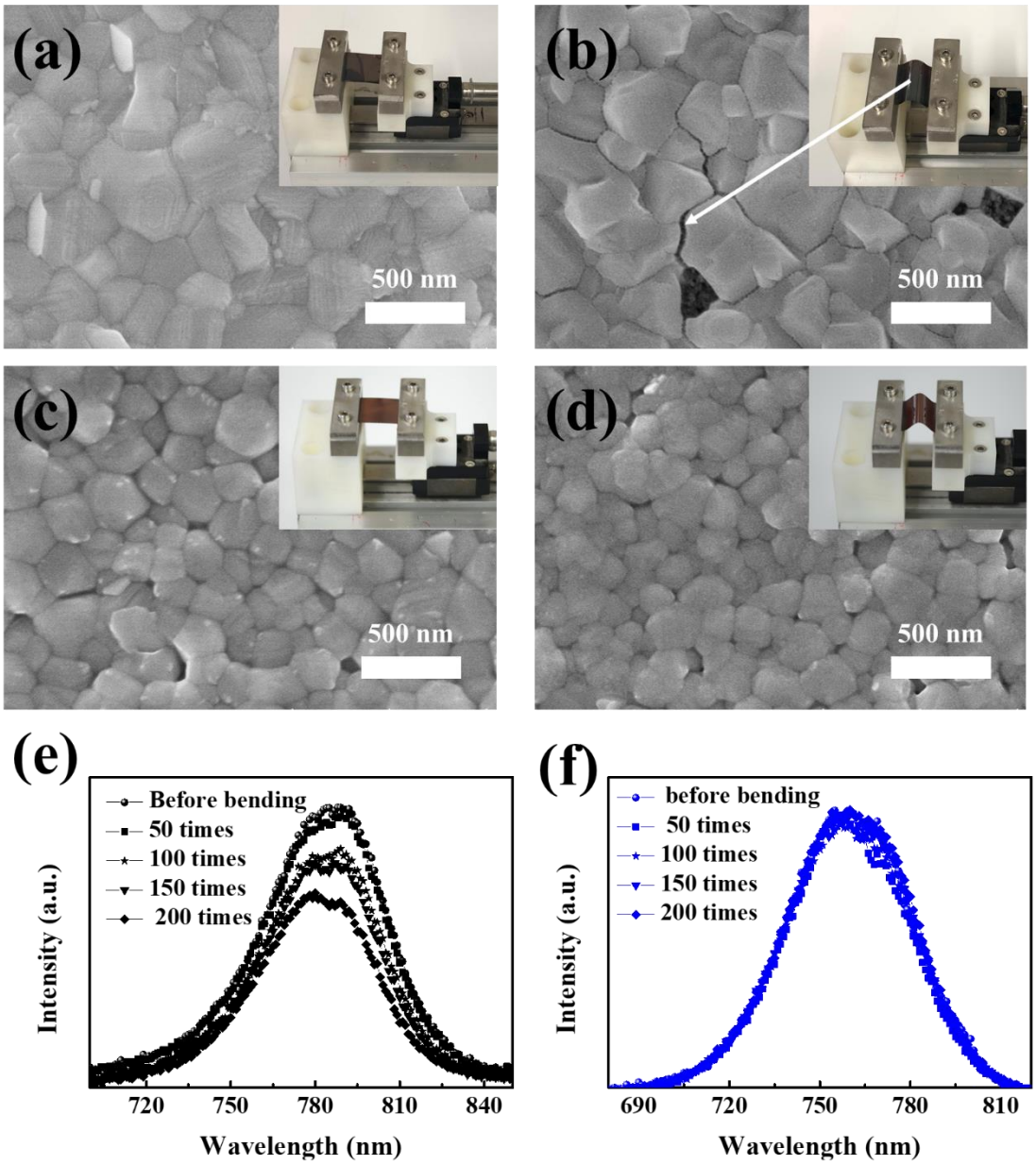

Figure 3-10. (a-d) Top-view SEM images of (a,b) 0 wt% PVP and (c.d) 8wt % PVP-perovskite grown on PET/ITO before and after 200 bending times with bending radius of 0.5 cm; the inset shows a photograph of the bending tests. (e)(f) Steady-state PL spectra of the corresponding pristine and PVP containing perovskite films.

To further investigate the impact of PVP on the performance of the perovskite films under bending induced stress, PET/ITO/SnO_2/perovskite/spiro-MeOTAD/Au devices were

fabricated and subjected to multiple bending cycles where the curvature was 5 mm for each cycle, as shown in Figure 3.11. Before bending, the PCE of PET/ITO based devices fabricated with perovskite active layers having 0 wt% and 8 wt% PVP was *ca.* 17% and *ca.* 15%, respectively. After 1000 bending cycles, the device fabricated using 8 wt% PVP-perovskite retained more than 70% of its original efficiency, whereas the pristine device exhibited less than 10% retention of its PCE. Complete data (before and after bending 1000 times) associated with flexible solar cell performance is presented in Table 3.3. Note that the V_{oc} slightly decreased in both cases; while short-circuit current decreased only slightly for the PVP containing active layer vs. the sharp decline observed when solar cell fabricated with pristine perovskite were bent 1000 times. Presumably, the decreased values of V_{oc} and J_{sc} are due to the inorganic SnO_2 film which is known to have poor flexibility.[132] The device results demonstrate that incorporation of PVP into the perovskite lattice can positively impact the mechanical properties of the hybrid active layer, allowing for the design and development of flexible devices.

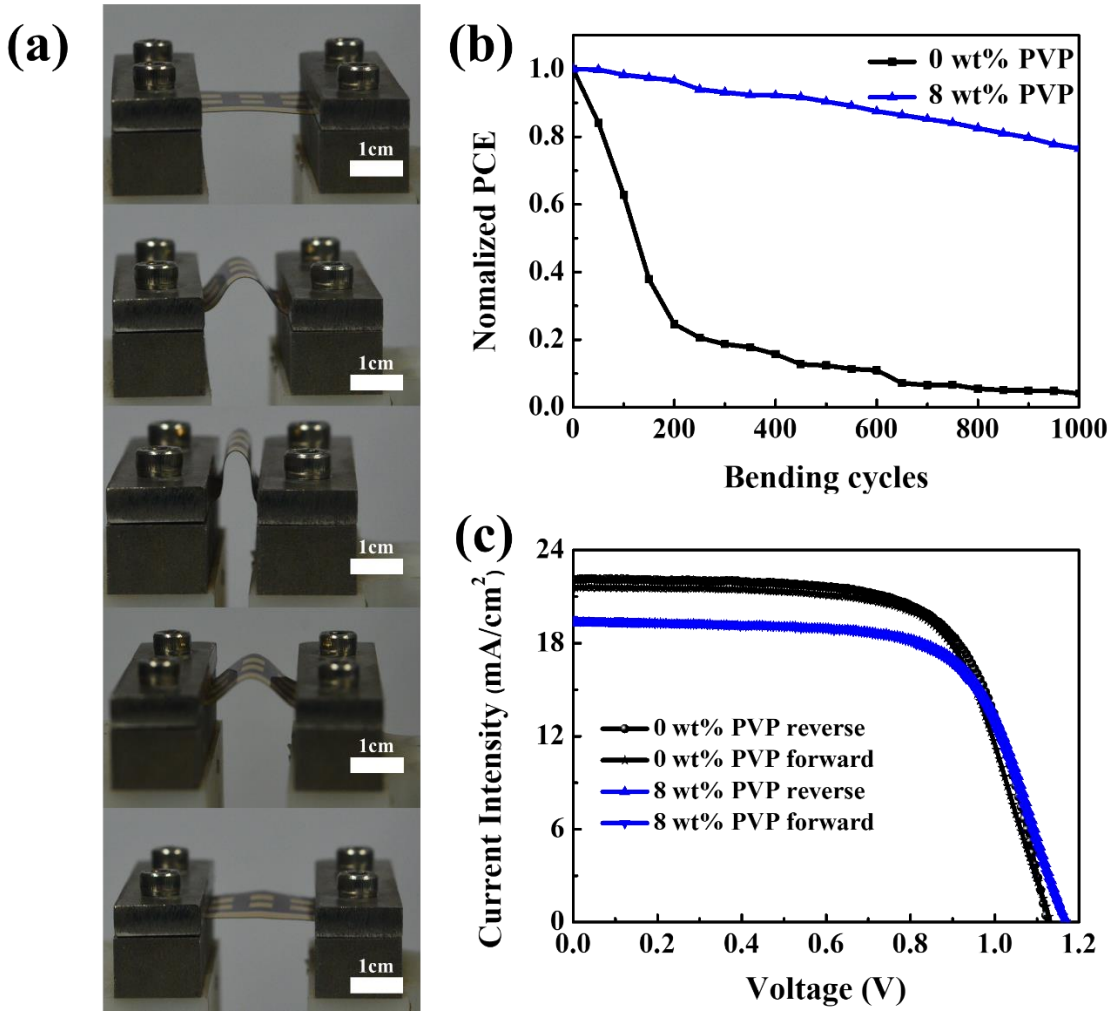

Figure 3-11. (a) Photograph of the bending tests for flexible devices; (b) Mechanical stability of corresponding flexible devices; (c) J−V curves of 0 wt% and 8 wt% PVP-perovskite flexible devices under AM 1.5G illumination at the initial stage.

Table 3-3. Photovoltaic performance parameters of flexible devices before bending and after bending 1000 times under standard AM 1.5G illumination (100 mW cm−2).

Device	**Before bending**	V_{oc} (V)	J_{sc} (mA/cm^2)	FF %	PCE %
0 wt%	Reverse	1.124	22.13	67.41	16.77
	Forward	1.132	21.60	67.12	16.41
8 wt%	Reverse	1.169	19.48	67.67	15.3
	Forward	1.167	19.37	66.12	15.10
	After bending 1000 times	V_{oc} (V)	J_{sc} (mA/cm^2)	FF %	PCE %
0 wt%	Reverse	1.03	1.41	45.33	0.66
	Forward	1.02	1.98	48.04	0.97
8 wt %	Reverse	1.08	18.41	58.83	11.71
	Forward	1.09	18.06	56.93	11.22

3.4 Conclusion

In summary, polyvinylpyrrolidone was introduced into a perovskite precursor solution, and effectively integrated into the resultant perovskite film. Incorporation of the polymer was shown to both protect the active material against degradation under humid ambient conditions and impart mechanical flexibility. Mechanistically, it is believed that PVP interacts with the perovskite *via* hydrogen bonding facilitated by the presence C=O bonds along the polymer chain. The results demonstrated that with an increased proportion of PVP, perovskite crystal size increased while XRD peaks shifted slightly, which confirmed the presence of interactions between the two components. PVP-perovskite based

solar cells comprising 8 wt% polymer additive exhibited a power conversion efficiency of 17%. The device efficiency remained above 15% for a duration of more than 600 hours under ambient conditions (> 60% humidity). Moreover, incorporation of PVP into the active layer facilitated fabrication of flexible solar cells, with an efficiency of *ca.* 15%, whereby the efficiencies were stable over several bending cycles. The results presented here demonstrate that polymer additives, such as PVP, that can effectively interact with the inorganic perovskite crystal can lead to environmentally stable and flexible perovskite solar cells. Modification of the perovskite through incorporation of a polymer additive is expected to enable the low-cost, large-scale fabrication of perovskite based solar cells.

CHAPTER 4. TRANSPARENT QUASI INTERDIGITATED ELECTRODES FOR PEROVSKITE BACK-CONTACT SOLAR CELLS[3]

4.1 Introduction

While back-contact electrodes (BCEs) are incorporated into the highest efficiency silicon solar cells,[135] they are yet to be adopted by researchers fabricating organometal halide perovskite analogues. The fabrication of back-contact perovskite solar cells (BC-PSCs) will eliminate parasitic absorption by the top contact, and leave the perovskite surface exposed, allowing for improvements through light-trapping, the application of an anti-reflective coating, new post-annealing techniques, surface passivation, and photoluminescence out-coupling.[136, 137] Furthermore, the architecture offers several functional advantages during fabrication, including the elimination of shorting due to pinholes, and avoiding damage to the perovskite layer during the deposition of subsequent layers.[138] However, the electrode spacing in the BCEs currently used in Si solar cells is too large for perovskites which have shorter carrier diffusion lengths. Also, the processes used to fabricate commercial BCEs are not compatible with perovskite thin films,[139] thus prohibiting the direct transfer of existing technology to this new class of photoabsorber material.

[3] DeLuca, Giovanni, et al. "Transparent Quasi-Interdigitated Electrodes for Semitransparent Perovskite Back-Contact Solar Cells." ACS Applied Energy Materials 1.9 (2018): 4473-4478.

The realization of operational BC-PSCs therefore necessitated the development of a new device architecture, namely quasi-interdigitated electrodes (QIDEs) (Figure 4.1a). This back-contact architecture places a finger-shaped cathode onto a continuous thin-film anode, with an insulating layer separating the electrodes. This avoids formation of the short-circuit pathways that occur in conventional co-planar interdigitated electrodes when a defect in one electrode finger causes contact with an adjacent electrode, a problem that increases in frequency as the electrode features are miniaturized to the dimensions required for the charge carrier diffusion lengths of perovskites.[138]

Although QIDEs present a robust architecture for BC-PSCs, a key design element limits their potential application. The top contacts are currently comprised of opaque Al/NiCo fingers, which are strong absorbers/reflectors of incident light (Figure 4.1b), preventing their use in semitransparent PSCs or as the top electrode in tandem perovskite-silicon solar cells. Therefore, for QIDEs to reach their full potential, the top electrode must be replaced with a transparent conductor. To this end, we introduce herein the first transparent quasi-interdigitated electrode (t-QIDEs) based on indium tin oxide (ITO), which has a high carrier concentration, low sheet resistance, and, most importantly, higher optical transmittance (>85% in visible wavelengths) than Al/NiCo.[140] Furthermore, we demonstrate the first operational semi-transparent back-contact perovskite solar cell. Optoelectronic theoretical simulations[136] also show the realistically achievable power conversion efficiencies (PCEs) and average visible transmissions (%AVT) with varying perovskite film thicknesses.

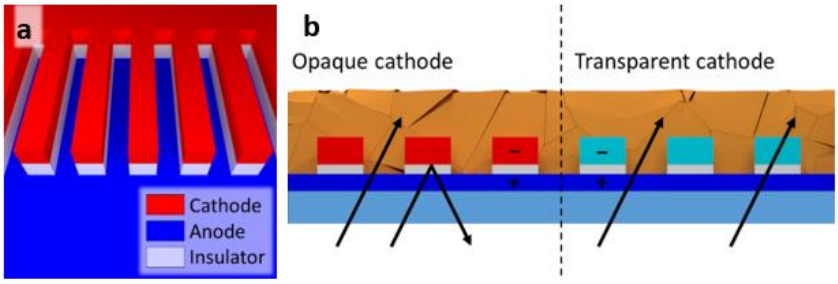

Figure 4-1. (a) The structure of a QIDEs. (b) Light transmission, absorption and reflection in QIDEs with Al/NiCo electrodes (left) or transparent electrodes (right).

4.2 Experimental section

4.2.1 Materials and reagents

Unless otherwise specified, all materials were purchased from either Alfa Aesar or Sigma-Aldrich and used as received. Fluorine doped tin oxide (FTO) coated glass substrates (10 cm × 10 cm, 2.2 mm; 7 Ω square^{-1}) were purchased from Solaronix. The ITO target was purchased from Kurt J. Lesker Company. Methylammonium (MA^+) bromide and formamidinium (FA^+) iodide were purchased from Greatcellsolar Ltd. High-purity nitrogen (99.999%; $O_2 \leq 2$ ppm, $H_2O \leq 0.1$ ppm) was used in all operations whenever nitrogen is mentioned. High purity deionized water (Milli-Q; 18 MΩ cm) was used in all operations whenever water is mentioned.

4.2.2 Transparent quasi-interdigitated electrode fabrication

Patterened FTO-coated glass substrates were sequentially cleaned in an ultrasonic bath in a 1% Hellmanex solution, water and ethanol (each for 15 min). A 15 nm compact TiO_2 layer was deposited by the spray pyrolysis of a 1:19 (v/v) titanium-diisopropoxide bis(acetylacetonate)/isopropanol solution at 500 °C. After being sintered for 30 min and cooling to room temperature, the substrates were removed from the hotplate. A polymer

mask with the desired features was then produced by spin-coating a ~2 µm thick photoresist layer (AZ 1512SH, Clariant), keeping the substrates at 110 °C for 2 min, and then exposing to UV light (30.1 mW cm^{-2} at 365 nm) for up to 6 sec through a chrome photo-mask. The UV-exposed parts of the photoresist layer were removed by washing the substrate in a developer solution (AZ 726MIF mixed with water in a 3:1 v/v ratio) for up to 50 sec, leaving the desired pattern that was protected by the photoresist mask.

Following this, a 100 nm Al_2O_3 insulator layer was deposited using an electronbeam evaporator to protect the device from short-cicuiting. A 200 nm ITO layer was then deposited using an ITO target by radio frequency magnetron sputtering. The substrate deposition temperature was set to 100 °C. The deposition power was 300 W and the deposition time was 7.5 minutes. The argon gas atmosphere was produced by evacuating an Anatech USA sputtering system to $<10^{-6}$ Torr, followed by flowing argon at 30 sccm. The pressure during the electrode deposition was 7 mTorr.

Following the ITO deposition, the remainder of the polymer mask was removed by immersing the substrates in acetone (lift-off process) overnight, leaving the quasi-interdigitated ITO electrodes. To produce low-resistance transparent quasi-interdigitated electrodes, the prepared t-QIDEs were additionally annealed at 300 °C for 3 minutes in air.

4.2.3 Deposition of CuSCN layer

Prior to electrochemical deposition, all glassware was extensively cleaned by washing with water and acetone. The electrolyte solutions were freshly prepared for every experiment by mixing equal volumes of aqueous solutions of 36 mM ethylenediaminetetraacetic acid (EDTA), 36 mM $CuSO_4$ and 36 mM KSCN. All

depositions were undertaken with air-saturated solutions at room temperature without stirring.

Electrodeposition of CuSCN hole-transport layers onto the ITO electrodes of the t-QIDEs was undertaken using a Biologic VMP electrochemical workstation in a bi-potentiostat mode under ambient conditions at 24 ± 1 °C. High-surface area titanium wire was used as an auxiliary electrode, which was confined to a separate compartment behind a low-porosity glass frit. An Ag|AgCl|3.4 M KCl reference electrode (KZT-5, Innovative Instruments Inc.) was positioned within 5 mm of the surface of the t-QIDEs (working electrode). Deposition was undertaken at −350 mV vs. Ag|AgCl|3.4 M KCl for each individual t-QIDEs (there are 6 t-QIDEs per substrate), while the other electrodes remained disconnected. The TiO_2/FTO anode was maintained at a potential of 400 mV during deposition to avoid any possible formation of CuSCN on its surface.

4.2.4 Device fabrication

The multiple-cation mixed-halide perovskite layer was fabricated according to a previously published protocol by Saliba *et al.*[141-143] Perovskite precursor solutions were prepared in a N_2-filled glove box by dissolving FAI (172 mg, 1 mmol), PbI_2 (507 mg, 1.1 mmol), MABr (22.4 mg, 0.2 mmol) and $PbBr_2$ (80.7 mg, 0.22 mmol) in 800 µL of anhydrous dimethylformamide (DMF) and 200 µL dimethyl sulfoxide (DMSO). To obtain a nominal composition of approximately $Cs_{0.05}FA_{0.79}MA_{0.16}PbI_{2.49}Br_{0.51}$ in the precursor solution, 42 µL of a CsI solution (389 mg, 1.5 mmol, in 1 mL DSMO) was added to 1 mL of the lead-containing solution. The final precursor solution was deposited onto the substrate in a N_2-filled glove box by spin-coating using a two-step procedure: Step 1)

speed: 1000 rpm, acceleration: 1000 rpm s^{-1}, duration: 10 s; Step 2) speed: 6000 rpm, acceleration: 6000 rpm s^{-1}, duration: 20 s. During the second step, 200 μL of anhydrous chlorobenzene was deposited onto the spinning substrate 5 s prior to the end of the program. The substrates were then annealed under dark conditions at 100 °C for 1 h in N_2.

4.2.5 Characterization

Grazing-incidence XRD measurements were performed on a Rigaku SmartLab diffractometer with a rotating anode CuKα source (45kV, 200mA), equipped with a Hypix 3000 detector. The diffractometer was configured with 0.15 mm incidence slits and a beam limiting mask of 5 mm. Data were collected over a 10–90° 2θ range with a step size of 0.02° and a step rate of 1° per minute. ω was kept fixed at 0.4°, just above the critical angle for ITO. The incidence slit, beam limiting mask and ω setting combine to maintain a beam footprint of ~21 mm × ~6 mm on the sample. Analyses were performed on the collected XRD data using the Bruker XRD search match program EVA™4.2. Crystalline phases were identified using the ICDD-JCPDS powder diffraction database.

UV-Vis-NIR measurements of thin film ITO samples were obtained using a PerkinElmer Lambda 1050 spectrophotometer equipped with an integrating sphere attachment. Measurements of the ITO finger electrodes were obtained using the same instrument fitted with a small spot kit to limit illumination to the electrode only.

Photoelectron Spectroscopy in Air (PESA) measurements were undertaken using a Riken Kekei AC-2 spectrometer at a power intensity of 50 nW to obtain the work functions of the ITO films. A power intensity of 20 nW as employed to obtain the ionization potential of the perovskite and the CuSCN film. The data were fitted as the cube root (n = 0.33) of the emission yield. Resistances of the ITO thin films were measured using a Jandal 4-point

probe station. Scanning electron microscopy (SEM) images were obtained using a Zeiss Merlin 4 microscope operated at 5 kV and 120 pA.

J-V characteristics of the devices were measured in an inert atmosphere with a computer controlled Keithley 2400 Source meter. A 150 W Xenon lamp (Newport) coupled with an AM1.5G solar spectrum filter was used as the light source. Light was illuminated through a quartz window of the glove box and the intensity was calibrated and monitored using a secondary reference photodiode (Hamamatsu S1133, with KG-5 filter, 2.8 mm × 2.4 mm photosensitive area), which was calibrated using a certified reference cell (PV Measurements, certified by NREL) under 100 mW cm^{-2} AM1.5G illumination from an Oriel AAA solar simulator fitted with a 1000 W Xenon lamp. Devices were measured at the same position as the secondary reference cell. The active area of the solar cell was 0.08 cm^2, defined by the quasi-interdigitated device area. *J-V* curves were recorded by scanning the potential from 1.0 to −0.1 V (reverse scan) and then from −0.1 to 1.0 V (forward scan) at a scan rate of 0.2 V s^{-1}. The stabilized power output was measured for 140 s at the maximum power point as determined by the software.

4.2.6 Computational modelling

The simulation results presented in this work were carried out using a fully coupled 3D optoelectronic modelling routine described elsewhere.[136] Briefly, the optical responses of the system were generated using a Finite-Difference Time-Domain method (FDTD, Lumerical) using all the optical constants of the materials as input parameters. Next, 3D spatial information of the charge generation rate from the perovskite layer with different thicknesses was computed based on this optical modelling and was then used as inputs for

the electrical modelling. Then, the electrical responses were carried out by solving drift-diffusion transport equations using a Finite-Element method (DEVICE Multiphysics, Lumerical) and the pre-defined electrical properties of all materials involved in the structures (Table 4.1). Finally, the solar cell characteristics were then computed based on the output of this electrical modelling.

The optical constants of perovskite,[144] ITO,[145] Al_2O_3,[136] TiO_2,[136] and FTO[146] were taken from literature. For determining the potential of the t-QIDEs structure, we used $CH_3NH_3PbI_3$ as it is the most thoroughly investigated of the perovskite family and is representative as a benchmark standard.

Table 4-1. Physical parameters used in simulations.

Parameter	Material					
	$CH_3NH_3PbI_3$	CuSCN	ITO	Al_2O_3	TiO_2	FTO
E_G (eV) [a]	1.55	3.6	-	6.7	3.2	-
m_e [b]	0.104	2	0.26	0.4[147]	0.6[148]	0.26
m_h [b]	0.104	0.5	0.26	0.4[147]	0.6[148]	0.26
ε_{DC} [c]	6.5	5.1	9	9.34	9	9
χ (eV) [d]	3.9	5.1	4.8	4.02	3.92	4.4
τ_e (ns) [e]	200	1	-	1	5	-
τ_h (ns) [e]	200	5	-	1	1	-
N_A (cm^{-3}) [f]	-	2×10^{18}	2×10^{18}	-	-	-
N_D (cm^{-3}) [f]	2.8×10^{17}	-	-	-	5×10^{17}	2×10^{18}
R_S (Ω sqr^{-1}) [g]	-	-	16	-	-	16

[a] Effective electronic bandgap at 300 K that is modelled using Varshni's coefficient.
[b] Effective mass which is used to calculate the density of states (DOS) at valence and conduction band using the Fermi-Dirac statistics.

[c] Relative dielectric constant (relative permittivity) at zero frequency (DC).
[d] Work function (*vs*. vacuum level).
[e] Charge lifetime (for electron (τ_e) and hole (τ_h)) where the values are varied (with fixed mobility) to obtain different values of minority charge diffusion length (L_D); where $L_D = [(k_BT/q).\mu.\tau]^{1/2}$.
[f] Doping density for acceptor (N_A) and donor (N_D).
[g] Sheet resistance; we also incorporated a shunt resistance (R_{sh}) in the external circuit to be 10^5 Ω/cm2. For Au, the sheet resistance is calculated based on equivalent resistivity ranging across the different pitch sizes.

4.3 Results and discussion

4.3.1 ITO characterization

Creating a t-QIDE first required optimization of the deposition of ITO that replaced the opaque components in the original architecture. This was achieved by varying the following deposition parameters: substrate temperature, ITO target power, argon and oxygen flow rates, and post-deposition annealing conditions. The optimized process yielded ~200 nm ITO thin films with an optical transmittance of ca. 88% at 592 nm (Figure 4.2), and sheet resistances ranging from 25 to 35 Ω square^{-1}. Photoelectron spectroscopy in air (PESA) measurements confirmed the ITO had a work function (4.78 ± 0.08 eV) comparable to literature values (Table 4.2).[149]

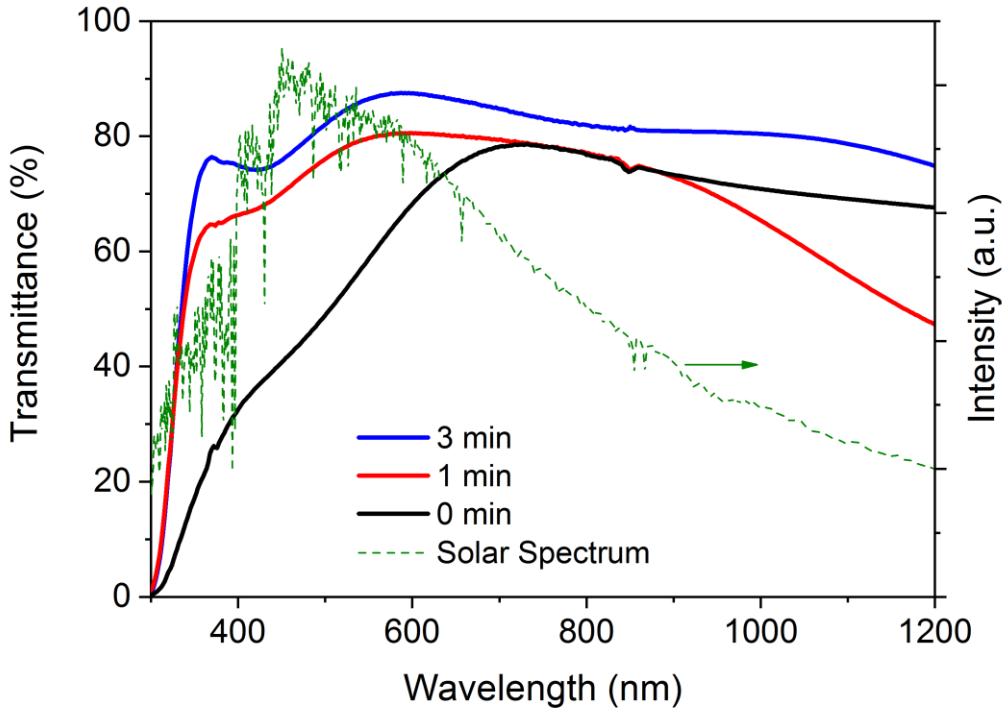

Figure 4-2. Comparison of the UV-Vis-NIR transmission spectra of ITO thin films on glass substrates annealed at 300 °C for 0 (black), 1 (red) or 3 min (blue) with the solar spectrum (green).

Table 4-2. PESA data for five independent ITO thin annealed for 3 min at 300 °C.

Sample	Ionization Potential (eV)	Gradient	Light Intensity (nW)
1	4.75	3.16	50
2	4.67	2.98	50
3	4.89	4.32	50
4	4.82	4.25	50
5	4.78	3.9	50
Average ± standard deviation	4.78 ± 0.08		

Post-deposition annealing for 3 minutes at 300 °C was required to enhance transmittance in the solar spectrum region (Figure 4.2). This accompanied the transformation of fully amorphous ITO to a highly crystalline phase, as evidenced by X-ray diffraction (XRD) measurements (Figure 4.3). In addition, post-deposition annealing resulted in a twenty-fold decrease in sheet resistance. While heating the substrate during ITO deposition is preferable to post-deposition annealing,[150, 151] the high temperatures required for the former process are not compatible with the photoresist used during t-QIDEs fabrication, therefore the sample required the post-annealing process.

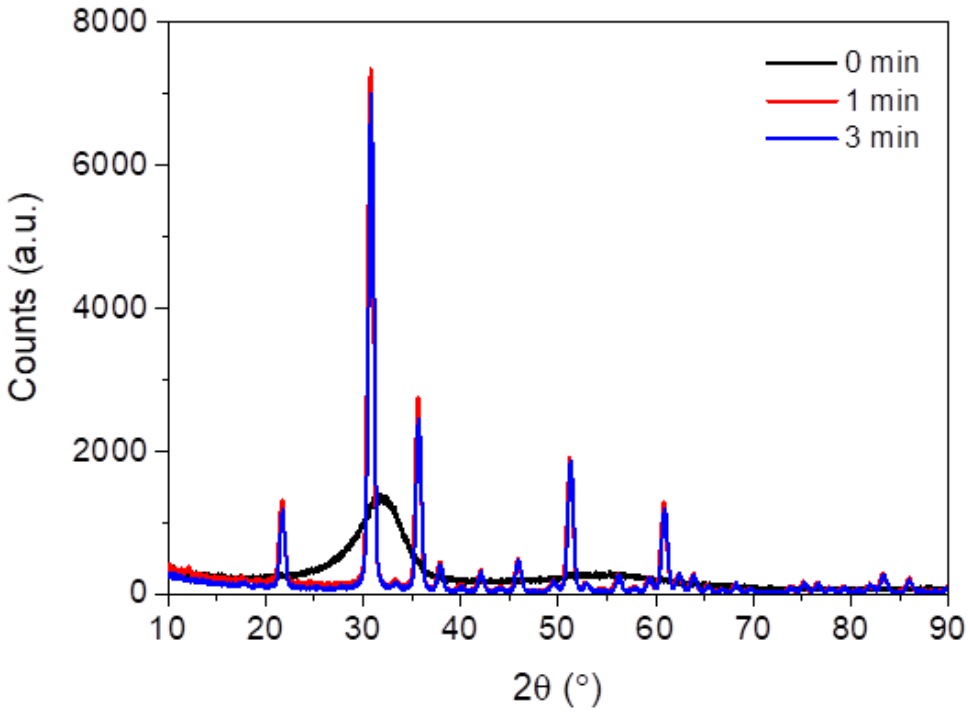

Figure 4-3. XRD patterns of an as-deposited ITO thin film on glass (black), and ITO thin films annealed at 300 °C for 1 (red) or 3 min (blue).

Once optimized, the deposition parameters were applied to the fabrication of ITO fingers for t-QIDEs. The initial electrode fabrication steps followed previously reported work,[138] where a photoresist served as the negative of the electrode pattern applied to a TiO_2/FTO stack on glass, followed by the deposition of an Al_2O_3 insulating layer to separate the anode and cathode. A continuous thin film of ITO was then deposited, and subsequent lift-off of the photoresist mask afforded ITO electrode fingers. Images taken following lift-off revealed the mask was completely removed and the ITO fingers were undamaged (Figure 4.4). After removing the photoresist mask, the electrodes were annealed, transforming the electrodes from light-brown to colorless (Figure 4.5). Finally, to ensure the electrodes have the necessary band energy alignment with a perovskite photoabsorber, a suitable hole transport material, copper (I) thiocyanate, was electrodeposited onto the ITO fingers prior to perovskite deposition.

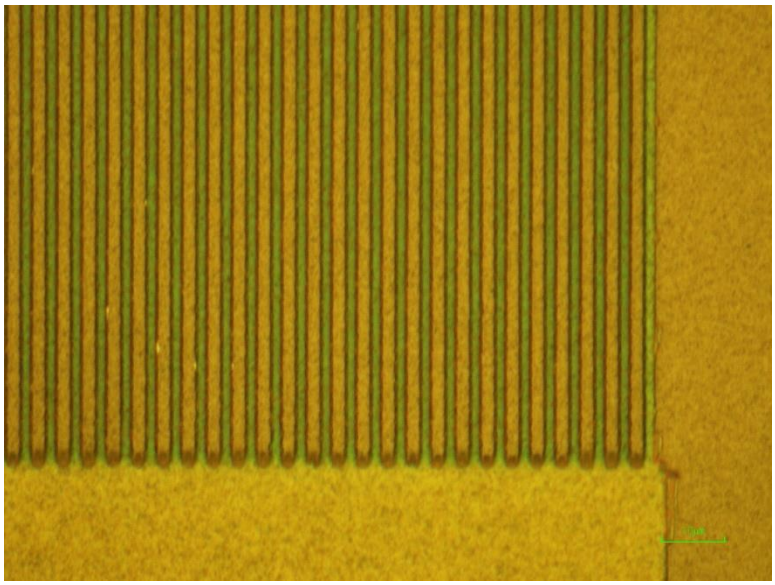

Figure 4-4. Visible light microscope image of ITO on Al2O3 fingers after polymer resist lift-off. Removal of the photoresist did not cause damage to the ITO fingers.

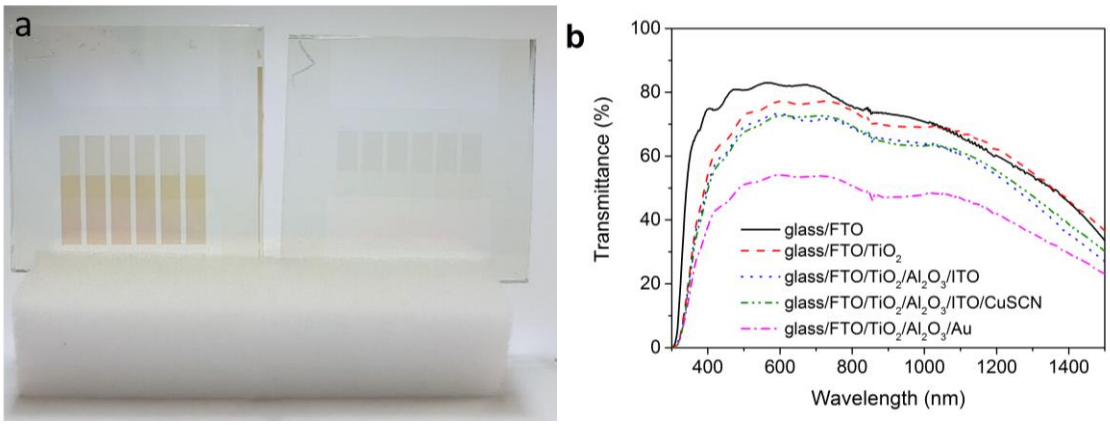

Figure 4-5. (a) Photograph of t-QIDEs before (left) and after annealing at 300 °C (right). (b) UV-Vis-NIR transmission spectra of the t-QIDEs at various stages of fabrication, and for QIDEs with a gold top electrode.

UV-Vis-NIR spectroscopy measurements were performed on the electrode stack at each stage of the fabrication process to determine the contribution of each component to the incident light absorption of the t-QIDEs (Figure 4.5b, Table 4.3). The pristine FTO-coated glass exhibited the highest transmittance, while TiO_2 deposition resulted in a slight drop in transmittance in the blue and visible regions of the spectrum. After depositing the Al_2O_3/ITO top electrode (quasi-interdigitated area), the overall transmittance decreased by approximately 15% and 10% relative to the FTO glass substrate and FTO/TiO_2 anode, respectively. This results mainly from the formation of additional interfaces (TiO_2/Al_2O_3 and Al_2O_3/ITO), which enhance the reflectance of the electrode assembly. The addition of the hole transport layer caused insignificant changes to the average transmittance (Figure 4.5b).

Table 4-3. UV-Vis-NIR transmission data for the various layers throughout the device and ITO thin film on glass.

Layer	%T (Average) (530–1100 nm)
FTO on glass	76
TiO_2:FTO on glass	73
ITO:Al_2O_3:TiO_2:FTO on glass	68
CuSCN:ITO:Al_2O_3:TiO_2:FTO on glass	68
Gold:Al_2O_3:TiO_2:FTO on glass	50
ITO film on 1.1 mm glass	81

The t-QIDE architecture is an ordinary reciprocal system that gives identical transmission through both sides, with insignificant differences probably arising from scattering (Figure 4.6). To demonstrate the transparency of the ITO fingers, identical measurements were performed on a device where ITO was replaced with a *ca.* 60 nm thick layer of gold. This substitution resulted in a significant decrease in transmission to *ca.* 50%, confirming that the relatively high transmittance of the t-QIDEs is due to the transparent nature of ITO (Figure 4.5b).

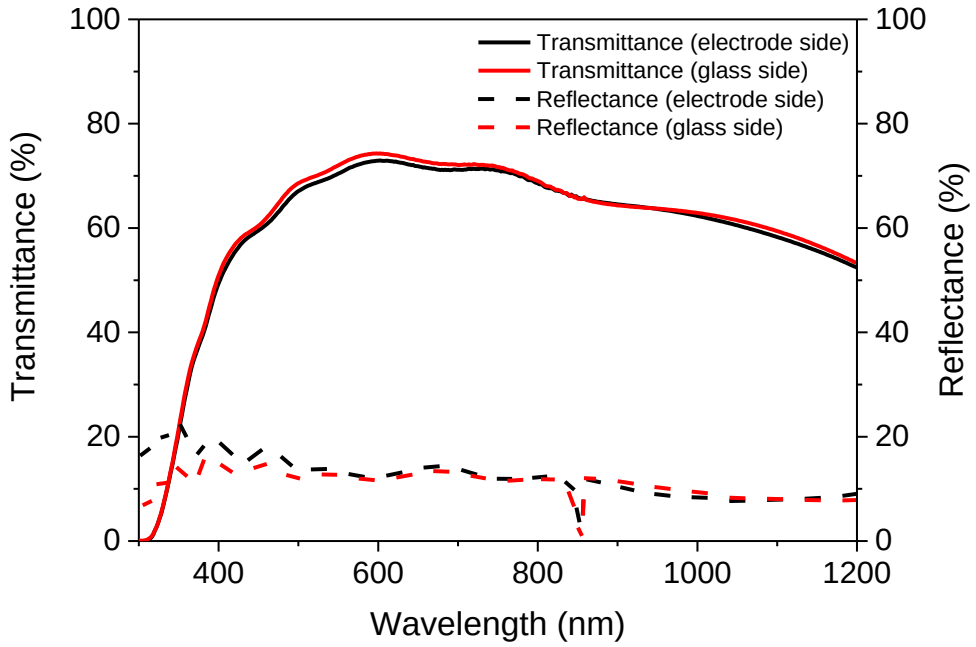

Figure 4-6. UV-Vis-NIR spectroscopy measurements in transmission and reflection modes for a CuSCN-modified t-QIDEs measured from the front (electrode) and rear (glass) side.

4.3.2 Perovskite characterization

While t-QIDEs could potentially be applied to a range of photoabsorber materials, CuSCN was applied to the ITO to provide a band energy alignment compatible with hybrid organic-inorganic perovskites (Figures 4.7-4.8). For this study we selected a multiple-cation mixed-halide perovskite with the nominal composition $Cs_{0.05}FA_{0.79}MA_{0.16}PbI_{2.49}Br_{0.51}$ as the photoabsorber, which has shown high photovoltaic efficiencies.[143]

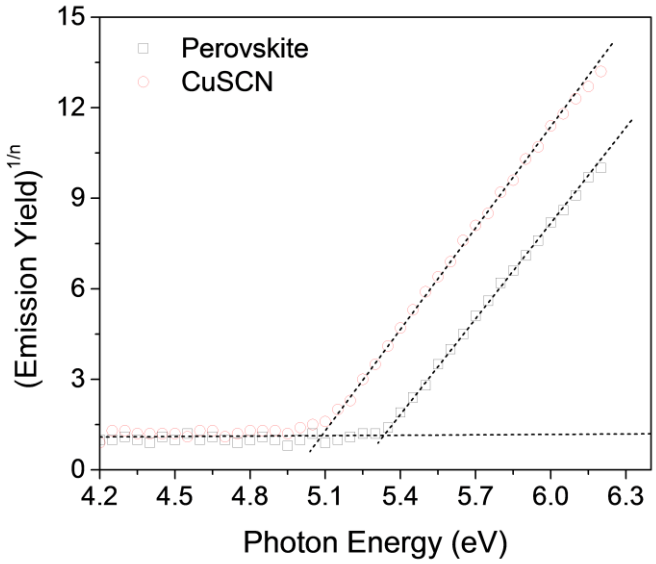

Figure 4-7. PESA measurement of the CuSCN and perovskite thin films deposited on t-QIDEs.

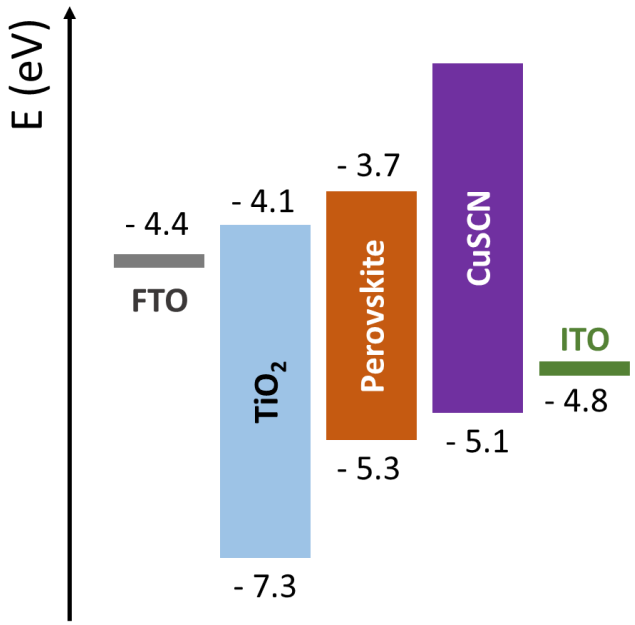

Figure 4-8. Band diagram for an n-i-p lateral PSC device with a t-QIDEs employing TiO_2 and CuSCN as charge selective layers. Valence band edge for perovskite and CuSCN as well as the work function of ITO were derived from PESA measurements (Table 4.2 and Figure 4.7).

Figure 4.9a presents a cross-sectional scanning electron micrograph of a back-contact PSC based on t-QIDEs. The back-scattered electron image of an individual finger reveals that a thin perovskite layer (~340 nm) uniformly covers the t-QIDE, which consists of a micro-structured cathode (~1.5 μm wide ITO/CuSCN fingers spaced every ~2.5 μm) on a continuous anode (FTO/TiO_2 on glass), separated by ~100 nm of Al_2O_3 (Figure 4.10). The micro-fingers of the cathode were trough shaped rather than perfectly flat, due to the polymer mask fabrication process where the edges of the grooves formed by the mask are imperfectly defined. A back-scattered electron cross-section image provides additional contrast to differentiate the functional device layers (Figure 4.9c).

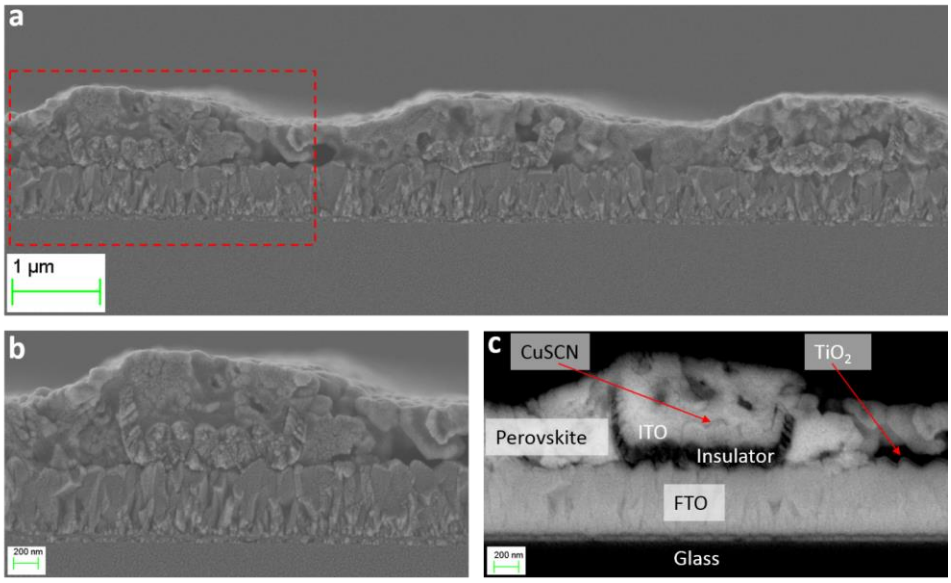

Figure 4-9. (a) Cross-sectional SEM image of the back-contact PSC based on the $Cs_{0.05}FA_{0.79}MA_{0.16}PbI_{2.49}Br_{0.51}$ photoabsorber and t-QIDE, (b) high magnification cross-sectional SEM image of the device (area enclosed with red rectangle in Figure 4.9a), (c) back-scattered SEM cross-sectional image of a finger of the device (area enclosed with red rectangle in Figure 4.9a).

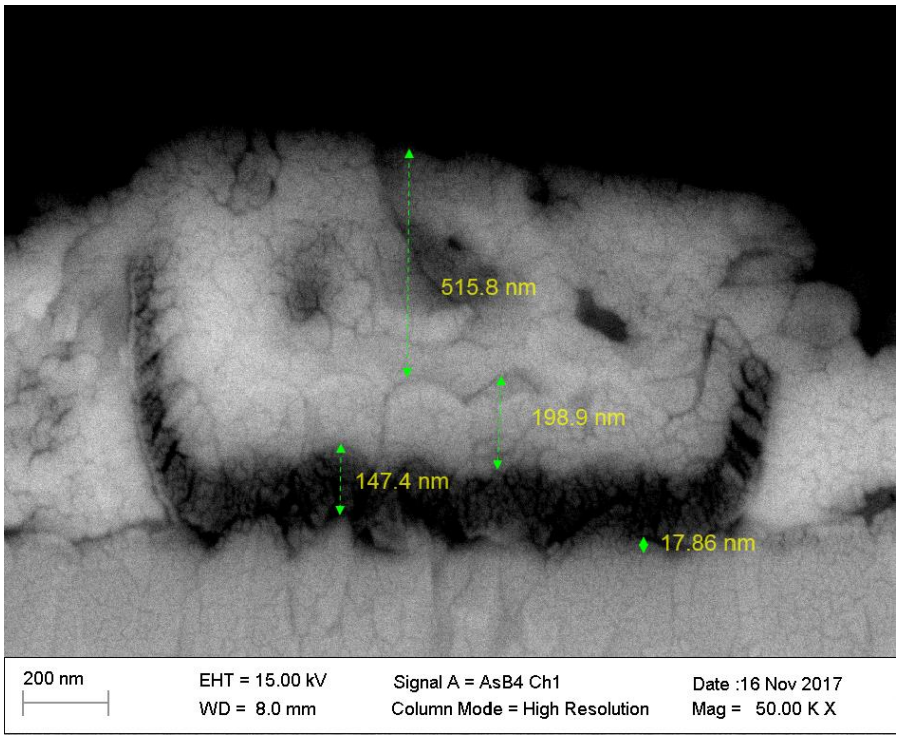

Figure 4-10. High magnification back-scattered electron cross sectional image of a back-contact PSC with t-QIDEs showing the thickness of its functional layers.

4.3.3 Photovoltaic performance of transparent back-contact perovskite solar cells

The *J-V* characteristics of BC-PSCs with t-QIDEs were recorded with both front (perovskite) and rear (glass) side illumination. Figure 4.11 shows *J-V* curves under 1 sun AM1.5G illumination and in the dark, while relevant photovoltaic parameters are summarized in Table 4.4. With front side illumination, values of 5.5 mA cm^{-2}, 0.84 V and 30% were recorded for short-circuit current density (J_{SC}), open-circuit voltage (V_{OC}) and fill factor (FF), respectively, yielding a PCE value of 1.4% for a reverse scan. For rear side illumination and reverse scan, a slightly higher PCE value of 1.7% was obtained, with J_{SC}, V_{OC} and fill factor being 5.6 mA cm^{-2}, 0.88 V and 34%, respectively.

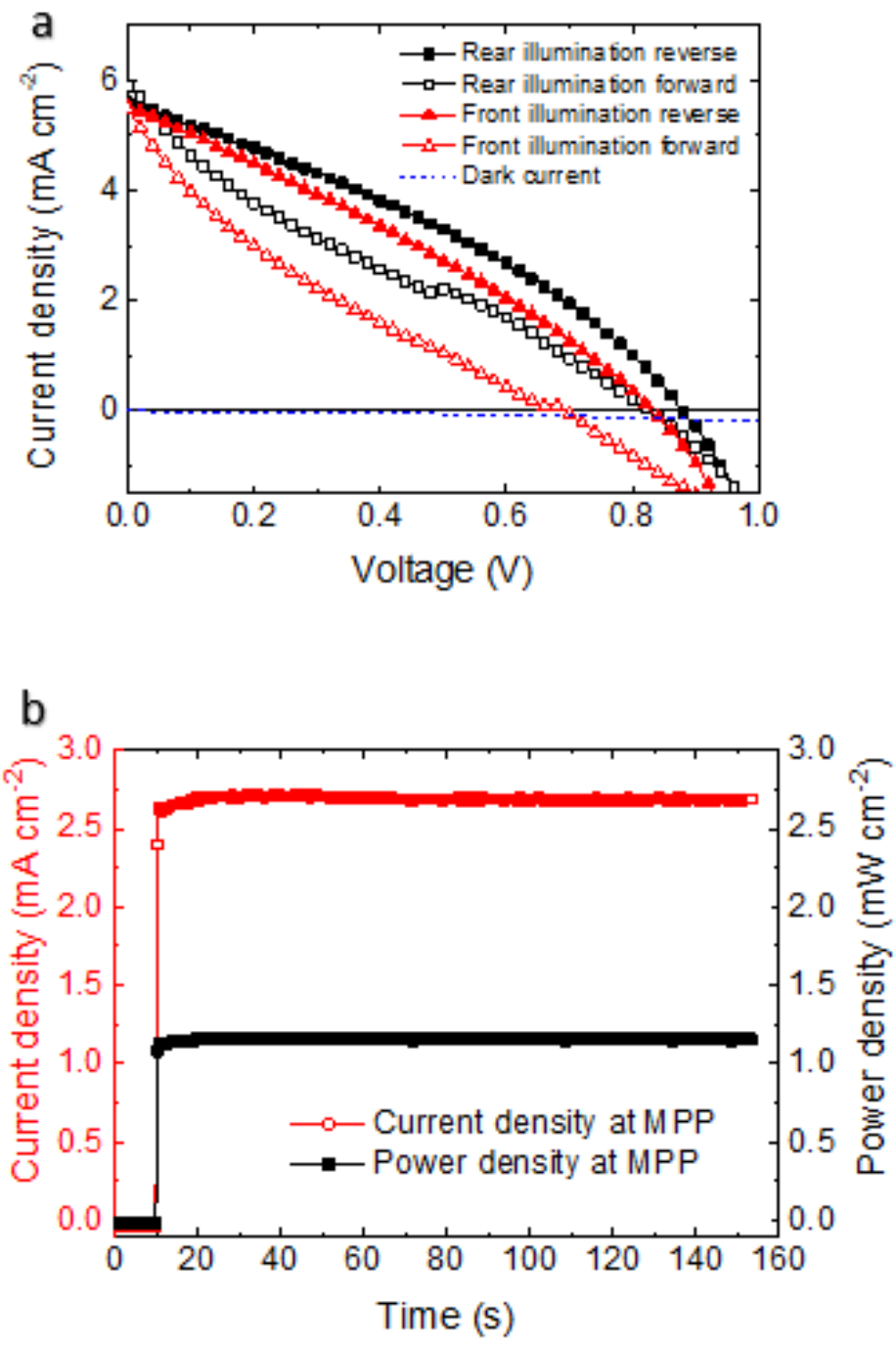

Figure 4-11. (a) J–V characteristics (scan rate 0.2 V s−1) of a BC-PSC based on the $Cs_{0.05}FA_{0.79}MA_{0.16}PbI_{2.49}Br_{0.51}$ light-absorber and a t-QIDE measured under 1 sun illumination from the front (perovskite) side and rear (glass) side, and in the dark. (b) Evolution of photocurrent and power density of the same BC-PSC at maximum power point under 1 sun irradiation from the rear side.

Table 4-4. Major photovoltaic parameters of back-contact PSCs with t-QIDEs.[a]

	V_{oc} (V)	J_{sc} (mA cm^{-2})	FF	PCE (%)
Rear illumination (reverse scan)	0.88	5.60	0.34	1.66
Rear illumination (forward scan)	0.82	5.89	0.23	1.11
Front illumination (reverse scan)	0.84	5.52	0.30	1.37
Front illumination (forward scan)	0.70	5.48	0.18	0.67

[a] Derived from *J*-*V* measurements (scan rate 0.2 V s^{-1}) under 100 mW cm^{-2} AM1.5G simulated illumination from the front (perovskite) and rear (glass) sides with forward and reverse scan directions.

As expected, excluding CuSCN from t-QIDEs resulted in lower device performance, demonstrating the advantages provided by having a hole-selective layer (Figure 4.12). The *J*-*V* curves exhibit hysteresis, which is typically assigned to ion migration and interfacial charge recombination.[152] The maximum power point (MPP) for the best-performing device irradiated with 1 sun from the rear showed a stable output with a PCE value of *ca* 1.2% maintained for at least 140 s (Figure 4.11b).

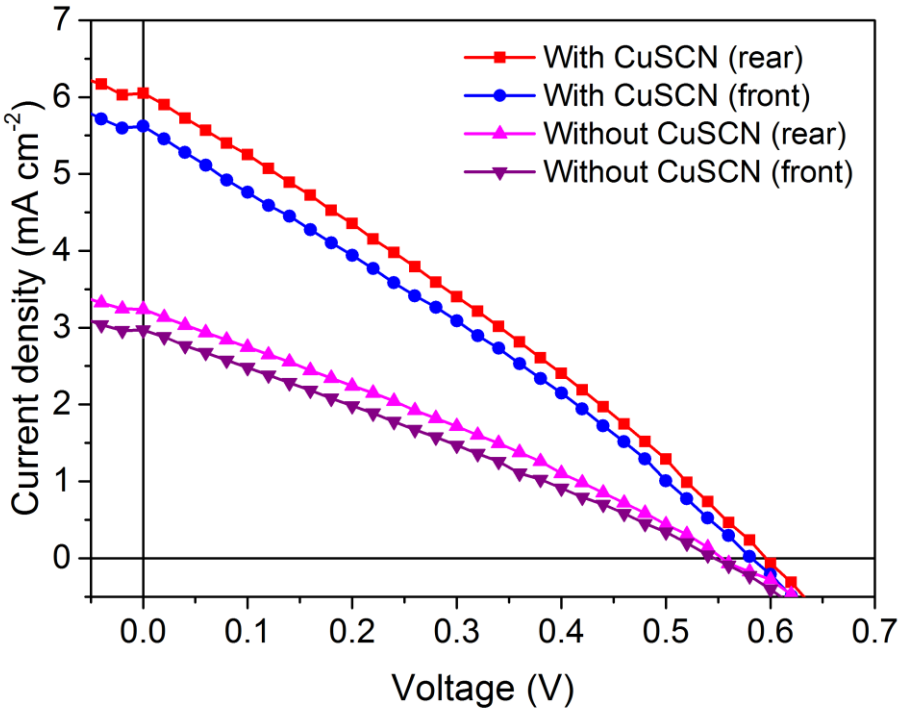

Figure 4-12. J-V curves of the BC-PSC devices with CuSCN (red and blue) and without CuSCN (pink and purple) when illuminated from the glass (rear) or perovskite (front) side of the device. Note the Voc, Jsc and FF of the device made with CuSCN are lower than the values reported for the champion device as they were made under non-optimized conditions. However, for comparison the device without CuSCN was made under the same conditions and originated from the same ITO batch.

A potential application of t-QIDEs is in semi-transparent perovskite solar cells. While the PCEs of the current devices are notably below the state-of-the-art for back-contact solar cells, future increases in efficiency are anticipated through increased perovskite grain sizes, a decreased sheet resistance of the transparent electrodes, and improved deposition procedures for the hole transport layer. To determine whether our device architecture could realistically reach the PCE and average visible transmission

(%AVT) of the previously reported semi-transparent solar cells,[153, 154] coupled optical and electrical simulations were performed using previously reported physical characteristics for key components (Table 4.1).[136]

The simulations, performed by collaborators at AMOLF-FOM, used a realistic quality of perovskite material with a minority carrier diffusion length of 500 nm. Figure 4.13a shows the simulated evolution of PCE as a function of perovskite layer thickness with a t-QIDE with optical and electrical properties as defined in this study. The simulations revealed an overall efficiency that is always higher when the cell is illuminated from the glass/electrode interface (rear-illumination) vs. the air/perovskite interface (front-illumination), which supports the experimental observations. A fluctuation in the PCE originates from a combination of thin-film interferences and drift-diffusion carrier transport, and becomes more pronounced with rear-illumination due to a higher number of modes evolved passing through the multilayer structure.[155] When the device is illuminated from the front or rear side, the simulated maximum efficiency is *ca.* 12% (at 750 nm perovskite thickness) or *ca.* 13% (at 650 nm perovskite thickness), respectively. Rear-illumination requires a ~50 nm thinner perovskite layer to reach a similar efficiency to front-illumination, which also suggests more efficient charge collection.

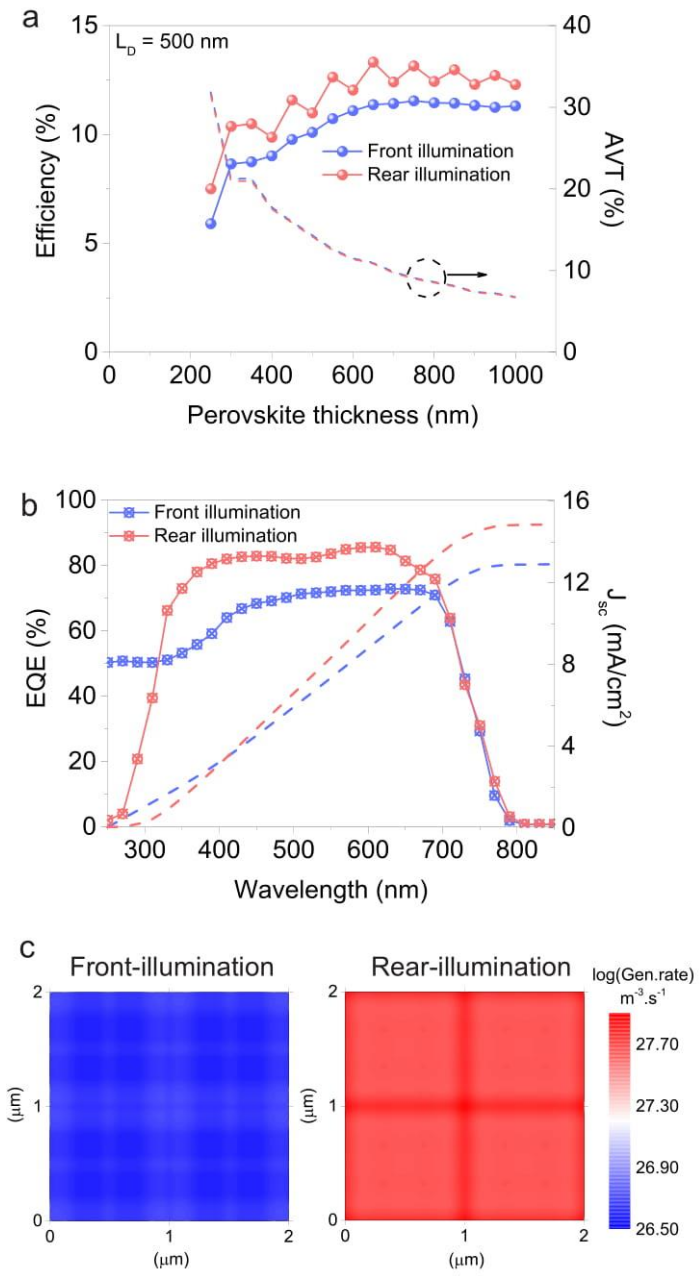

Figure 4-13. Simulated performance of a BC-PSC under front and rear illumination. (a) PCS and AVT as a function of perovskite thickness (the perovskite thickness cannot be below the thickness of the back-contact electrode, viz. 250 nm). (b) External quantum efficiency (EQE) at the optimum thickness of the perovskite layer (750 and 650 nm for front- and rear-illumination, respectively). (c) Charge generation rate of the perovskite layer in between the two back-contact electrodes. The generation rate is averaged over the thickness of the perovskite and leveled to the total thickness of the electrodes. The apparent interference fringes are due to optical modes created by the multi layered structure evolved. Simulations were based on AM 1.5 spectrum and a 500 nm minority-carrier diffusion length for the perovskite.

Figure 4.13a also demonstrates the potential of BC-PSCs to act as semi-transparent devices when thin layers of perovskite absorber are employed. The average visible transmittance (AVT) is calculated between 400 and 800 nm for comparison with reported work.[153, 154] For the thinnest perovskite layer needed for the PSC to be operational, *viz.* 250 nm, which is the thickness of the back-contact electrode, a potential AVT of 32% was calculated. Corresponding PCE values were predicted as 5.9 and 7.5% for the devices irradiated from the front and rear, respectively (Table 4.5). These values are comparable to previous reports for tandem organic photovoltaics.[156] At the maximum efficiencies, AVTs of 9.1% (front illumination, PCE = 12%) and 11% (rear illumination, PCE = 13%) were calculated, demonstrating potentially superior performance.[153, 154] The back-contact architecture also permits the application of an antireflective coating, light trapping, surface passivation, and photoluminescence out-coupling enhancements, which are expected to improve both the PCE and AVT of an optimized device.[136]

Table 4-5. Simulated PCE and AVT data for t-QIDEs-based back-contact PSCs.

	Front illumination					Rear illumination				
Perovskite layer thickness (nm)	AVT (%)	J_{SC} (mA/cm^2)	V_{OC} (V)	FF	PCE (%)	AVT (%)	J_{SC} (mA/cm^2)	V_{OC} (V)	FF	PCE (%)
250	31.86	5.87	1.17	0.86	5.91	31.54	7.42	1.17	0.86	7.50
650	10.97	12.70	1.06	0.84	11.37	10.88	14.83	1.06	0.84	13.32
700	9.86	12.93	1.06	0.84	11.42	9.72	14.02	1.06	0.84	12.41
750	9.11	13.25	1.06	0.82	11.54	9.01	15.05	1.06	0.82	13.15

To identify the contribution to charge collection efficiency across the spectrum, the external quantum efficiency (EQE) of a BC-PSC at the optimal conditions for front- and rear-illumination was simulated (Figure 4.13b). In the short wavelength range (up to 430

nm), front-illumination is more efficient due to the absence of any parasitic absorption layer (ITO) in the first optical path of the incoming photons. In contrast, with rear illumination, the collection efficiency is higher within the higher wavelength range (430–780 nm), resulting in an increased accumulated J_{sc}. This is partly due to better index-matching between the glass|ITO|perovskite interfaces than the air|perovskite interface, effectively creating an anti-reflective coating that minimizes total reflectance. This leads to increased absorption in the perovskite, and a higher charge photogeneration rate near the back-contact electrode (Figure 4.13c). An order of magnitude difference for the rear and front illumination conditions (Figure 4.13c) explains the experimentally observed difference in J_{sc} (Figure 4.11a).

Simulations undertaken herein suggest that further optimization of devices with t-QIDEs should be possible by minimizing parasitic losses. For example, this can be achieved by increasing the spacing gap size between the back-contact (for a fixed back-contact width), if possible with a better quality of perovskite material (*e.g.* with minority-carrier diffusion length $L_D > 10$ μm) (Figure 4.14a). Alternatively, increasing a filling fraction of the back-contact electrode is seen as a promising strategy for a realistic quality of perovskite ($L_D \approx 0.5$ μm). Unlike devices incorporating metal electrodes, the PCE is less sensitive to the width of the ITO back-contact finger (Figure 4.14b).[157]

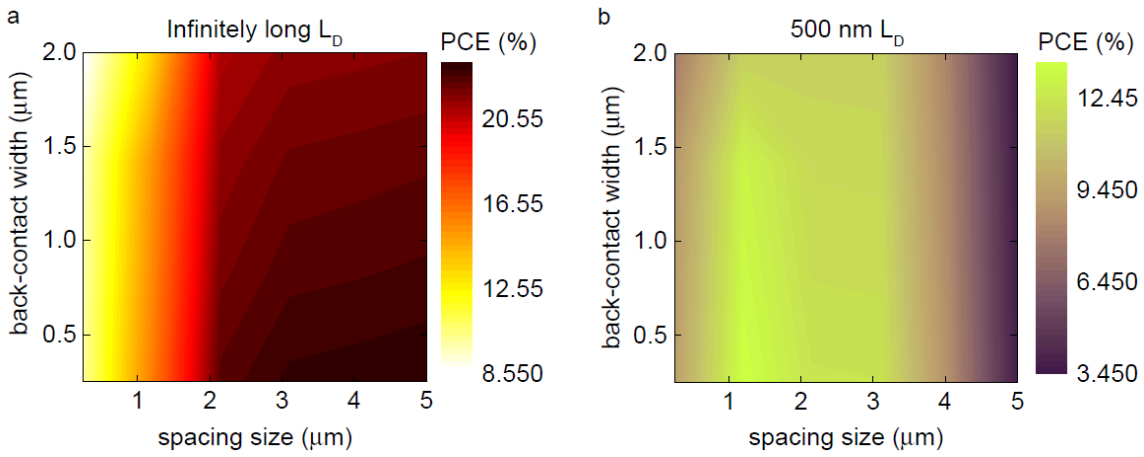

Figure 4-14. Simulated power-conversion-efficiency (PCE) map of the t-QIDEs-based back-contact PSCs as a function of back-contact width and gap size between the two back-contacts for (a) infinitely long and (b) 500 nm minority carrier diffusion length within the perovskite layer. The maps were constructed by simulating a pitch size of 0.25, 0.5, 1, 2, 3 and 5 μm, while simultaneously varying the contact width of 0.25, 0.5, 1 and 2 μm. The data between these input parameter values were calculated by linear interpolation. Note that the origin point of these two plots is at (0.25, 0.25).

4.4 Conclusion

In summary, the fabrication of a transparent back-contact electrode was achieved by replacing the opaque components of conventional QIDEs with ITO. These electrodes were used as substrates for the first semi-transparent back-contact perovskite solar cells with a modest PCE of 1.2%. Importantly, this new class of devices offers straightforward strategies for optimization that could significantly increase the efficiency. Simulations showed that if these improvements can be achieved, BC-PSCs incorporating t-QIDEs will offer a pathway to efficient semitransparent photovoltaic devices.

CHAPTER 5. DOPED-ITO FOR PEROVSKITE SOLAR CELLS

5.1 Introduction

Due to its high carrier concentration and wide optical band gap, ITO exhibits electrical (resistivity $<10^{-4}$ Ω cm) and optical (transmittance >85% in visible wavelengths)[158] properties that have made it ubiquitous in commercial optoelectronic applications, from liquid crystal displays to light emitting diodes[159-169]. Furthermore, because of the simplicity and cost-effectiveness[170, 171] of producing ITO on a large scale via direct current (DC) or radio frequency (RF) magnetron sputtering, the material is being widely studied for application in tandem solar cells[172]. Significant amount of work has gone into exploring the effects of doping ITO[173-176], and researchers have discovered many advantages, however this comes at a cost. Nakasa *et. al.* used a pyrolysis procedure to produce high work function, nickel-doped ITO, but an increase in sheet resistance by a factor of six was observed.[177] Kim *et. al.* noticed a large decrease in resistance, however there was also a decrease in transmittance and no change in work function by making a ITO/Ni/ITO sandwich.[178] Caricato *et. al.* observed an increase in transmittance doping ITO with chromium, however this was accompanied by a large increase in resistivity.[179] In this work, either the resistance or transmittance has been negatively affected, or the procedure is expensive or non-reproducible. Here, we explore a simple route to dope ITO, modifying the work function, while not disturbing the desirable properties of ITO. We use a co-deposition procedure, depositing ITO from a RF source and a metal dopant from a DC source in a sputtering tool. This procedure increased work functions up to 5.56 eV from

4.7-4.9 eV of undoped ITO, while maintaining resistances in the range of 9-19 Ω square^{-1} and transmittance in the range of 80-82% in the visible region.

5.2 Experimental section

5.2.1 Doped ITO preparation

Glass substrates were washed in detergent, water, acetone, and isopropyl alcohol (15 min ultrasonic bath with each solvent). The substrates were then dried with nitrogen gas and placed in the PVA TePla Plasma Asher for 10 minutes. Following this, the samples were placed in the Anatech USA sputtering system and evacuated to 1.00 X 10^{-6} Torr. The rotation plate was set to ~45%. The chamber was dosed with 100 sccm oxygen gas and 30 sccm argon gas for 5 minutes (1.8-1.9 mTorr). After the five minutes, the RF source was powered on at 100 W, and the gas supply was lowered to 0 sccm oxygen and 15 sccm argon. The RF Tune/Load read 16%/39%, respectively. ITO was deposited at room temperature for 30 minutes at 4.3-4.5 mTorr.

After the 30 minutes, the procedure was repeated. That is, the chamber was evacuated to 1.00 X 10^{-6} Torr, and then dosed with 100 sccm oxygen gas and 30 sccm argon gas for 5 minutes (1.8-1.9 mTorr). After the five minutes had elapsed, the RF source was powered on at 100 W, and the gas flow was lowered to 0 sccm oxygen and 15 sccm argon. The RF Tune/Load read 16%/39%, respectively. ITO was again deposited at room temperature for 30 minutes at 4.3-4.5 mTorr. The chamber was vented, and the samples were collected for initial analysis of the amorphous ITO. Following this procedure, the samples were either returned to the Anatech USA sputtering system for co-deposition of

ITO with a metal target; alternatively, they were placed in a nitrogen glovebox for annealing.

The samples used for interface doping were placed in a vacuum chamber which was evacuated to 1.00 X 10^{-6} Torr. The rotation plate was set to ~45%. The chamber was dosed with 100 sccm oxygen gas and 30 sccm argon gas for 5 minutes (1.8-1.9 mTorr). After five minutes had elapsed, the RF source and DC source were powered on at 100 W and 30 W (7.7-7.8 mTorr) respectively. The metal at the DC source was either nickel, tungsten, or titanium. The ITO was co-deposited with a metal at room temperature for varying times, namely 30 seconds, 60 seconds, or 120 seconds. The samples were then placed in the nitrogen glovebox alongside the un-doped ITO substrates. All samples were annealed in the nitrogen atmosphere for one hour. All targets were cleaned individually prior to co-deposition.

5.2.2 Characterization

Grazing-incidence XRD measurements were performed on a Rigaku SmartLab diffractometer with a rotating anode CuKα source (45kV, 200mA), equipped with a Hypix 3000 detector. The diffractometer was configured with 0.15 mm incidence slits and a beam limiting mask of 5 mm. Data were collected over a 10–90° 2θ range with a step size of 0.02° and a step rate of 1° per minute. The angel ω was kept fixed at 0.4°, just above the critical angle for ITO. The incidence slit, beam limiting mask and ω setting combine to maintain a beam footprint of ~21 mm × ~6 mm on the sample. Analyses were performed on the collected XRD data using the Bruker XRD search match program EVA™4.2. Crystalline phases were identified using the ICDD-JCPDS powder diffraction database.

UV-vis-NIR measurements of thin film ITO samples were obtained using a J.A. Woollam M-2000DI spectroscopic ellipsometer with a transmission stage attachment. Photoelectron Spectroscopy in Air (PESA) measurements were undertaken using a Riken Kekei AC-2 spectrometer at a power intensity of 50 nW to obtain the work functions of the ITO films. Resistances of the ITO thin films were measured using a Jandal 4-point probe station.

5.3 Results and discussion

5.3.1 ITO characterization

Following the initial deposition of ITO, sample electrical characteristics were measured using a Jandel RM-3000 four-point probe station. The acceptable resistance range for amorphous, un-annealed ITO is 20 to 40 Ω square^{-1}. Following the resistance check, an additional interlayer of ITO was co-deposited with a metal dopant (Ti, Ni, or W), or was directly annealed and for use in control un-doped ITO measurements. The process yielded ~200 nm ITO thin films with an optical transmittance of ca. 80-82% in the visible region (400-800 nm), and sheet resistances ranging from 9 to 19 Ω square^{-1}.

Photoelectron spectroscopy in air (PESA) measurements confirmed the un-doped ITO had a work function comparable to literature values (Table 5.1). Changes to the work function were apparent in the doped ITO, with the most favorable improvement seen in the Ni-doped ITO (Table 5.1). The work function of undoped ITO 4.7-4.9 eV was increased to 5.26 eV, 5.35 eV, and 5.56 eV by doping with titanium, tungsten and nickel respectively. The increase in work function is thought to be due to crystal growth and interface band

bending.[177] Through doping with nickel, the ionization potential of ITO aligns well with valence band of the methylammonium lead iodide perovskite film, which is ca. 5.5 eV.[180]

As evidenced by X-ray diffraction (XRD) measurements (Figure 5.1), crystalline phase ITO was achieved in all samples.; and the phase found in all samples was crystalline ITO in the space group Ia-3 (206). Lattice parameters varied only slightly between the 4 samples (Table 5.2), ranging from 10.108 Å to 10.114 Å.

Table 5-1. Ionization potential of the undoped and doped ITO.

Sample Number	Sample Name	Ionization Potential (eV)
1	0	0.00
2	Un-doped ITO	4.78
3	30 sec W-ITO	5.24
4	60 sec W-ITO	5.35
5	30 sec Ni-ITO	5.46
6	60 sec Ni-ITO	5.56
7	30 sec Ti-ITO	5.16
8	60 sec Ti-ITO	5.26

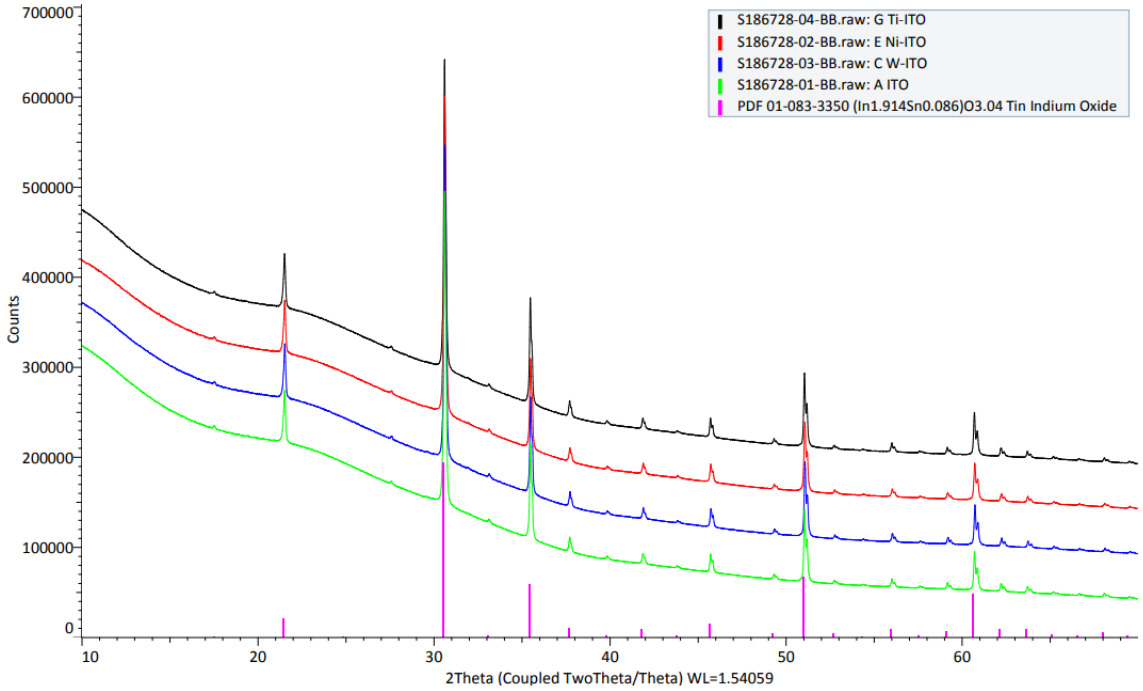

Figure 5-1. Diffraction pattern of undoped ITO and Ni-doped ITO

Table 5-2. Lattice parameter for the ITO and doped ITO phase.

Sample	a-parameter (Å) (±0.001)
Undoped ITO	**10.112**
Ni-Doped ITO	**10.110**
W-Doped ITO	**10.108**
Ti-Doped ITO	**10.114**

Due to the Ni-doped ITO work function aligning with the perovskite valence band, it was further investigated by transmittance spectroscopy. Very little changes were observed in the visible region, with an overall slight increase in the visible region (400-800 nm). However, a significant increase in transmittance was observed in the IR region. It is speculated that the doped sample has an altered refractive index, causing the electrode to also act as an anti-reflective coating. Further investigation with ellipsometry is necessary to confirm this hypothesis.

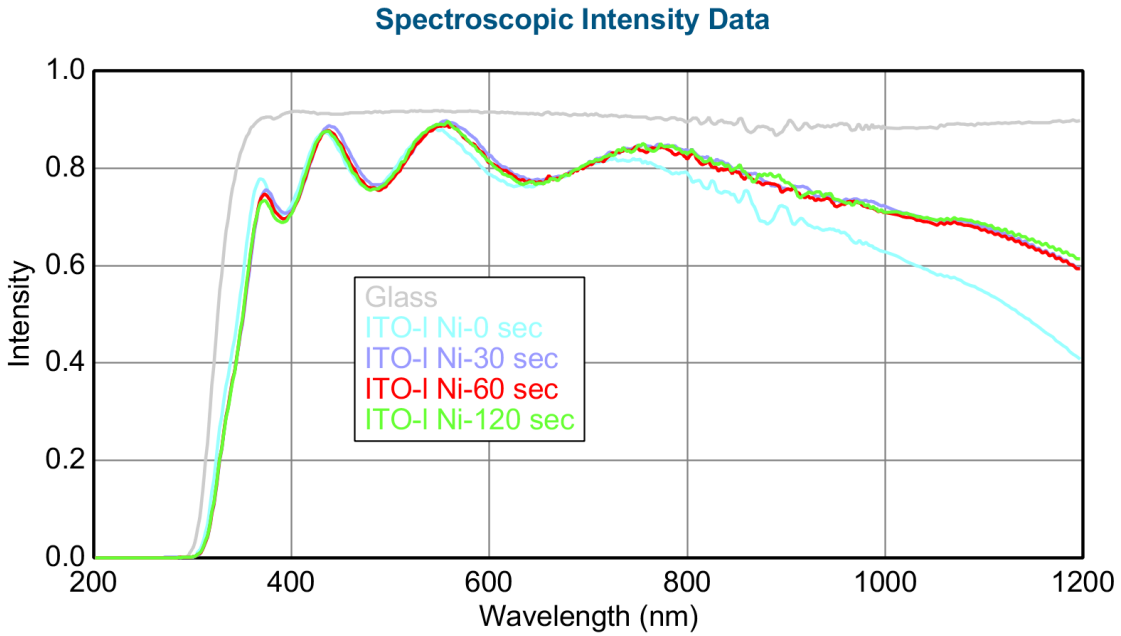

Figure 5-2. Transmittance of glass, undoped ITO, and Ni doped ITO

5.4 Conclusion and future direction

In summary, crystalline ITO electrodes were produced with ideal resistances and transmittances, comparable to commercially available ITO. However, the ITO doped with nickel had the advantage of a tuned work function, up to 5.6 eV. The transmittance of the electrodes were also improved in the IR region. The improvements to ITO's properties brings us to our future work. Recently, a hole-transport-layer-free device (Figure 5.3)[180] was fabricated with a power conversion efficiency of 20.0%. This was achieved by p-doping the perovskite film with 2,3,5,6-Tetrafluoro-7,7,8,8-tetracyanoquinodimethane (F4TCNQ). The high efficiency was credited to the improvement to the series resistance (Figure 5.4)[180], however and obvious band misalignment is still observed. For our future work, we will repeat fabricating the high efficiency devices, on high work function, doped ITO.

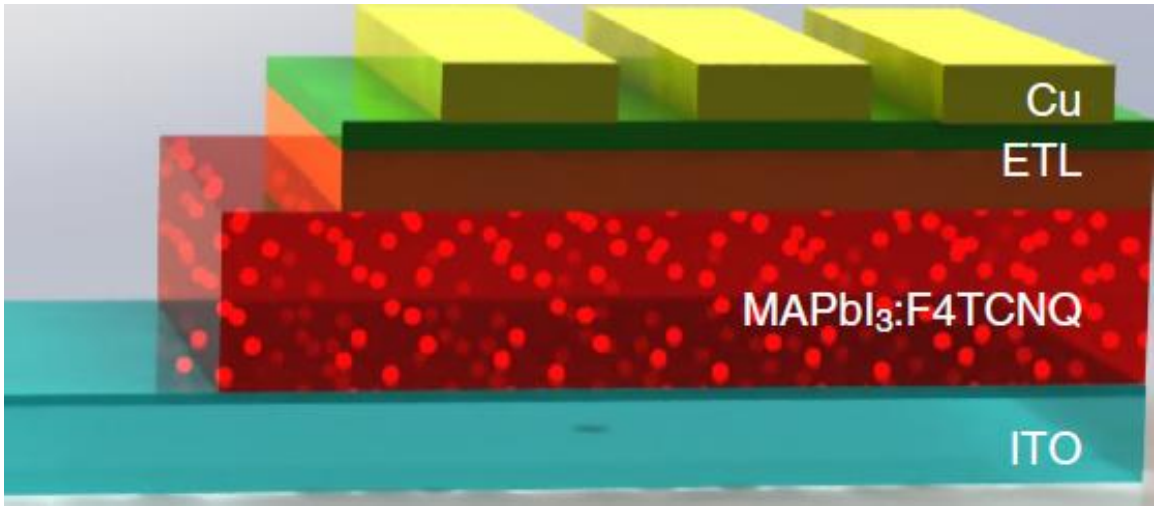

Figure 5-3. Hole-transport-layer-free device (republished with permission).[180]

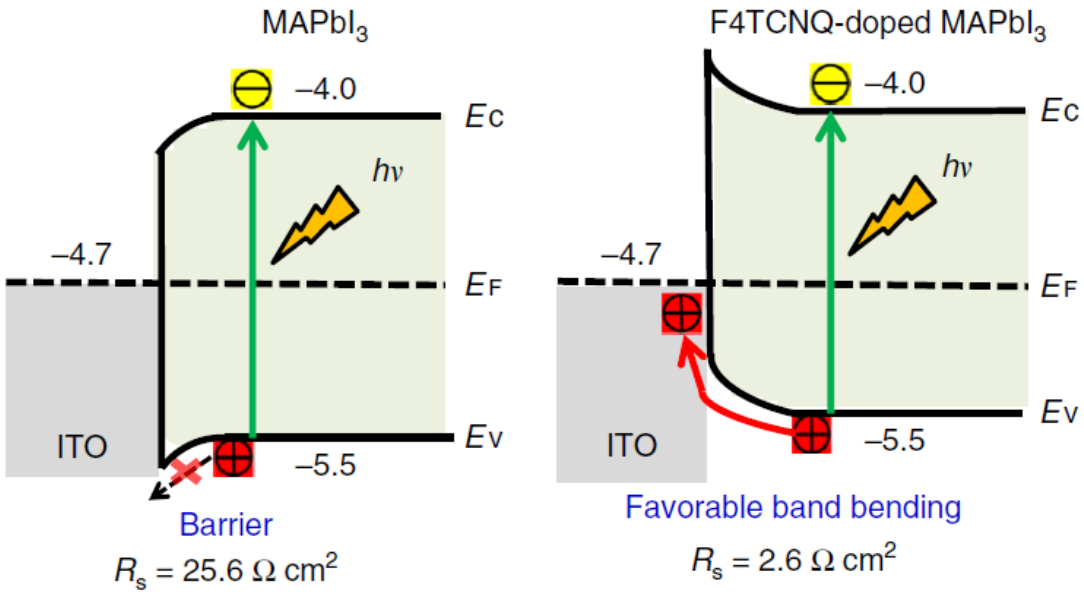

Figure 5-4. Interfacial hole transfer dynamics. Schematic illustrations of hole transfer at the ITO/$MAPbI_3$ and ITO/F4TCNQ-doped $MAPbI_3$ interface (republished with permission).[180]

5.4.1 Future direction

Successful fabrication of high-efficiency planar devices will then pave the way for inverted back-contact perovskite solar cells, which to this day has not been achieved. In addition, this work will also allow us to explore Ni-doped ITO as a top electrode for silicon solar cells due to the improvement of the transmittance in the IR region. Successful fabrication of this device will then allow for the integration of the perovskite solar cell to silicon solar cell, moving towards perovskite/silicon tandem solar cells. Further investigation into the doping of ITO with other metals will follow this work as well.

CHAPTER 6. CONCLUDING REMARKS AND FUTURE WORK

Methylammonium lead iodide perovskite ($MAPbI_3$), and its analogs, holds a lot of promise as a technologically relevant material for solar cell applications. Solar cell applications that use $MAPbI_3$, or similar perovskite materials, are reported with an optimistic frequency. This high-efficiency, promising material is prompting researchers to take a closer look at its application in a broad range of materials, from electronic textiles to perovskite-silicon tandem solar cells. Though researchers are already developing high-efficiency perovskite solar cells with efficiencies comparable to crystalline silicon, there are limitations to this work, specifically with respect to scalability, moisture sensitivity, hysteresis, and cost of production. Therefore, there is still a need for developing new methodologies for producing perovskite solar cells that would overcome the limitations of current approaches. This work explores possible routes to overcome some of the aforementioned limitations through interfacial, architectural, and solution-based strategies. The final products were extensively characterized with spectroscopic, microscopic, and electrical characterization techniques.

The two-step perovskite film fabrication method is thought to be a promising route for large scale production due to its easy-to-transfer method to a roll-to-roll process. Chapter 1 introduced the reader to this method. Chapters 2 and 5 of this Thesis introduced methods for producing perovskite films using the two-step spin coating procedure. In both Chapters, improvements were observed to the perovskite film. In the case of Chapter 2, a post-annealing technique was employed to the DMSO-PbI_2 film, causing a microporous network throughout the layer. An improvement to the conversion to PbI_2 from the

$PbI_2(DMSO)_2$ complex was also observed by XRD. This allowed for the complete conversion to $MAPbI_3$ perovskite crystal fabricated in ambient conditions. The simple technique presented here could be used to prepare large area perovskite solar cells in ambient conditions. Solar cells fabricated using this methodology exhibited power conversion efficiencies over 16% with negligible photocurrent hysteresis under ambient conditions with about 50% humidity.

Incorporation of polymeric materials (polyethylene glycol (PEG), phenethylamine, polyurethane, *etc.*) can lead to their application in flexible electronics. One such example, based on the incorporation of polyvinylpyrrolidone (PVP) into the perovskite matrix is described in Chapter 3. Here, the one-step spin coating technique was employed with the PVP polymer introduced directly into the precursor solution. First planar devices on glass were fabricated to determine the optimized conditions for the PVP-perovskite precursor solution. The 8 wt% PVP-perovskite samples were able to achieve reproducible efficiencies up to 17% in an atmosphere of 60% humidity. The devices maintained stable performance characteristics during exposure to the humid atmosphere for 600 hours. Following this, the 8 wt% PVP-perovskite solution was spun onto flexible substrates, which produced devices with efficiencies of ca. 15%. After bending 1000 times with a bending radius of 0.5 cm the devices were able to retain 73% of their efficiency.

Chapter 4 explored a novel architecture with the potential for applications in bifacial solar cells and tandem solar cells. Here, transparent back-contact perovskite solar cells were fabricated, and produced a modest efficiency of 1.7%. It was shown by coupled optical and electrical simulations, that there is a large potential to increase the power conversion efficiency, while maintaining a low average visible transmission. This new

class of devices offers straightforward strategies for optimization that could significantly increase the efficiency. The simulations showed that if these improvements can be achieved, BC-PSCs incorporating t-QIDEs will offer a pathway to efficient semitransparent devices. In addition, an efficiency of over 13% is possible for this architecture, which makes it a perfect candidate for a top cell in perovskite/silicon tandem solar cells. The advantage of using the back-contact architecture for tandem devices is due to the exposed perovskite surface, allowing for improvements through light-trapping, the application of an anti-reflective coating, new post-annealing techniques, surface passivation, and photoluminescence out-coupling. In the immediate future, this work will employ the technology from Chapter 6 to fabricate the first inverted back-contact perovskite, which will be discussed in more detail shortly.

Chapter 5 explored a route for tuning the work function of ITO for better band alignment with the perovskite layer in hole-transport-layer-free perovskite solar cells. Work functions going up to 5.56 eV were achieved by doping ITO with nickel, while maintaining resistances of 9-19 Ω square^{-1} and transmittance of 82% in the visible region. Improvements were also observed to the transmittance in the IR region. The next step is to make hole-transport-layer-free devices with the doped ITO and p-doped perovskite. Once high-efficiency devices are achieved, transparent, inverted back-contact perovskite solar cells will be fabricated. The advantage being the removal of an additional transport layer, therefor hopefully improving the overall average visible transmittance of the device. Following this, the devices will be coupled with silicon solar cells, with the intent of high-efficiency tandem solar cells.

6.1 Future direction

In our current work, we revisit the two-step deposition procedure, this time incorporating the additives (DMF and 1M HCl) directly into the MAI/IPA precursor solution and varying the loading time. This work was carried out to explore a more direct route to the large-scale fabrication of perovskite solar cells. With the correct amount of 1 M HCl and DMF added to the MAI/IPA solution, we were able to observe complete conversion to the perovskite crystal. This procedure did not require the anti-solvent technique or a post annealing technique. The next step is to make devices using the film with the optimized recipe. Once a working device is fabricated, we will move towards large area devices. Procedural adaptations will then be made in order to produce devices using a printing technique.

6.1.1 Introduction

Continuing off of the work from Chapter 2, a procedure that is more amenable for large-scale development/fabrication of perovskite solar cells was investigated. In this work, the post treatment annealing step was removed from the two-step deposition procedure. Instead, small aliquots of DMF were added to the MAI/IPA precursor solution. In addition, past work has demonstrated the advantage of chloride ion being introduced into the perovskite one-step solution to increase perovskite grain size, improve perovskite film crystallinity and surface coverage.[181-185] In the present study, small aliquots of 1 M HCl were added to the MAI/IPA and its advantages were investigated. We explore an optimized recipe for the perovskite layer using the two-step method with a simple additive approach.

Lastly, we will study how the MAI/IPA with DMF/HCl additive loading time length effect the device performance and stability.

6.1.2 Experimental section

6.1.2.1 $CH_3NH_3PbI_3$ film fabrication

The perovskite films were fabricated using a sequential deposition process, reproduced from Sample 1 of Chapter 2. PbI_2 (462 mg) was dissolved in anhydrous DMF at 70 °C, to form a 1 M PbI_2/DMF. The PbI_2/ DMF solution was deposited onto a FTO glass substrate by spin coating at 3000 rpm for 30 s, and the resultant film was then annealed for 10 min at 70 °C in the ambient to afford dense PbI_2 (d-PbI_2).

CH_3NH_3I was dissolved in 2-propanol (10 mg/mL) at 80 °C to afford 18 mL of solution with varying amounts of DMF and 1 M HCL (Table 6.1). This solution was loaded onto the d-PbI_2 coated substrate where it remained undisturbed for varying loading times (Table 6.1). The substrate was then spin coated at 4000 rpm for 30 s and annealed at 110 °C for 10 min, forming the dark perovskite layer. The operation was carried out under humid ambient conditions.

Table 6-1. Variables to the recipe for this work, including varying loading times.

GROUP	DMF (μL)	1mol HCl (μL)	Loading Time (s)		
1	0	0	30	60	90
		10			
		20			
		50			
2	10	0	30	60	90
		10			
		20			
		50			
3	20	0	30	60	90
		10			
		20			
		50			
4	50	0	30	60	90
		10			
		20			
		50			

6.1.2.2 Characterization

The perovskite film was identified by one-dimensional X-ray diffraction (1D XRD) (Model D/max 2550 V, Rigaku Co. Tokyo, Japan) by using Cu Kα (λ=1.5406 Å) radiation. Two-dimensional wide-angle X-ray diffraction (WAXD) analysis was conducted using a Bruker D8 Discover GADDS X-ray Diffractometer operating at 40 kV and 40 mA, Cu Kα radiation. The morphology of the resultant perovskite film was observed by using field-emission scanning electron microscopy (FESEM, Model S-4800, Hitachi, Japan). Steady-state photoluminescence (PL) spectra were acquired with a FLS920 transient optical spectrometer (Edinburgh Instruments, UK).

6.1.3 Results and discussion

Figure 6.1 presents the UV–vis absorption spectra of the perovskite crystal fabricated with varying loading times. The minimal absorbance observed for the perovskite film is attributed to the remaining PbI_2, as demonstrated XRD (Figure 6.2). The maximum

absorption was observed for samples that employed a 90 second loading time. This data was repeatable for two separate recipes.

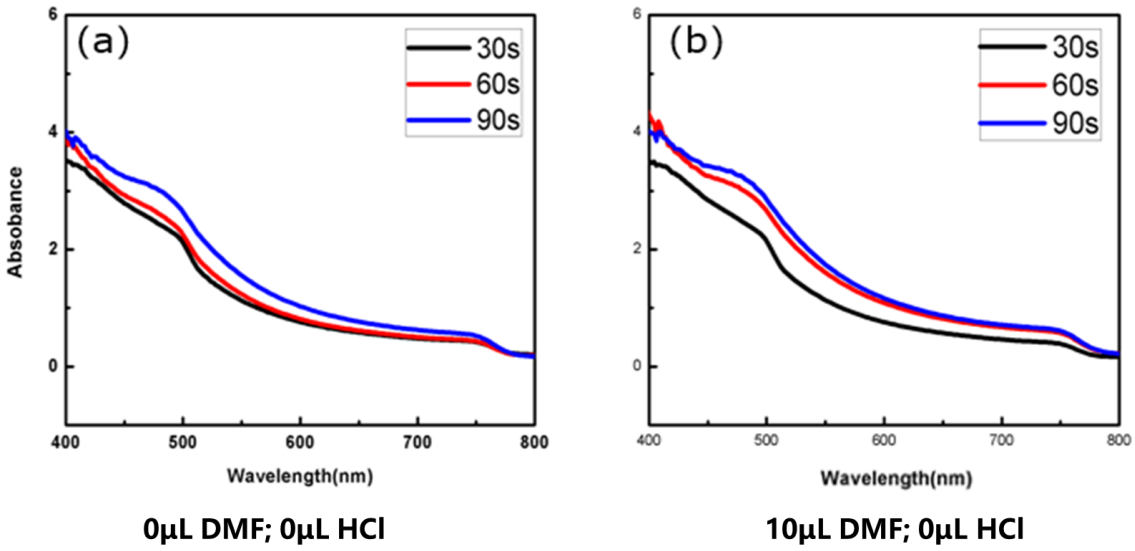

Figure 6-1. UV-visible absorption spectra of perovskite films on FTO glass made with varying loading times (30s, 60s, and 90s) of the MAI/IPA precursor solution.

The effect of loading time on the film was further studied using X-ray diffraction (Figure 6.2). Solutions containing varying amounts of additive were loaded onto the PbI_2 layer for 30s, 60s, and 90s. In each case, there was an observed decrease in the PbI_2 crystal diffraction pattern, demonstrating the conversion to $MAPbI_3$ perovskite crystal, as the loading time was increased.

To further explore the effects of loading time, photoluminescence (PL) studies were carried out (Figure 6.3). As mentioned earlier, $CH_3NH_3PbI_3$ is a highly luminescent material, which means that the quenching of its PL intensity can be used as a measure of the charge extraction ability of the perovskite layer. The perovskite PL spectra show the

characteristic peak at 770 nm (eV). However, for the samples with a 30s and 60s loading time, a blue-shift was observed. This change in absorbance is believed to be related to the presence of unreacted PbI_2. Another interesting phenomenon observed here was that the photoluminscence is significantly improved by the addition of 10 µL of DMF. The effects of DMF and 1M HCL will now be explored.

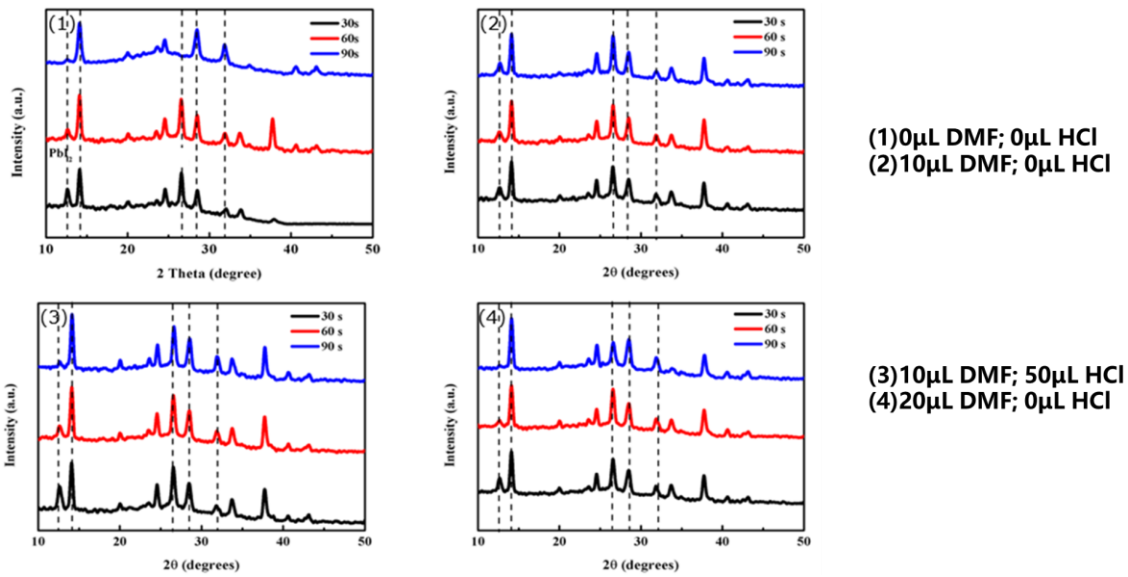

Figure 6-2. Diffraction pattern of perovskite films on FTO glass made with varying loading times (30s, 60s, and 90s) of the MAI/IPA precursor solution.

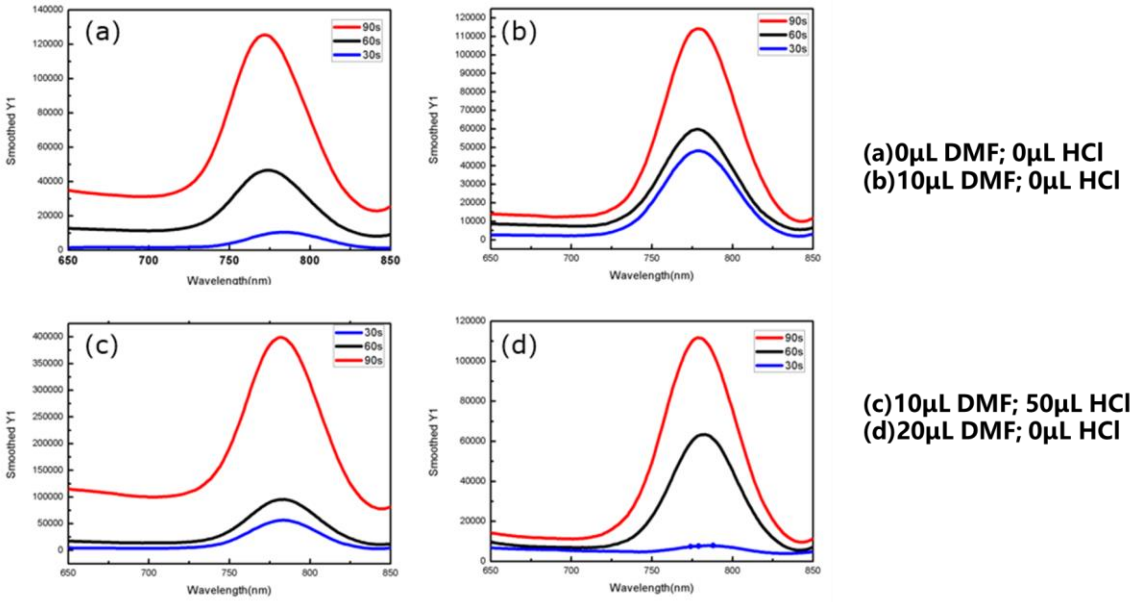

Figure 6-3. Photoluminescence study of perovskite films on FTO glass made with varying loading times (30s, 60s, and 90s) of the MAI/IPA precursor solution.

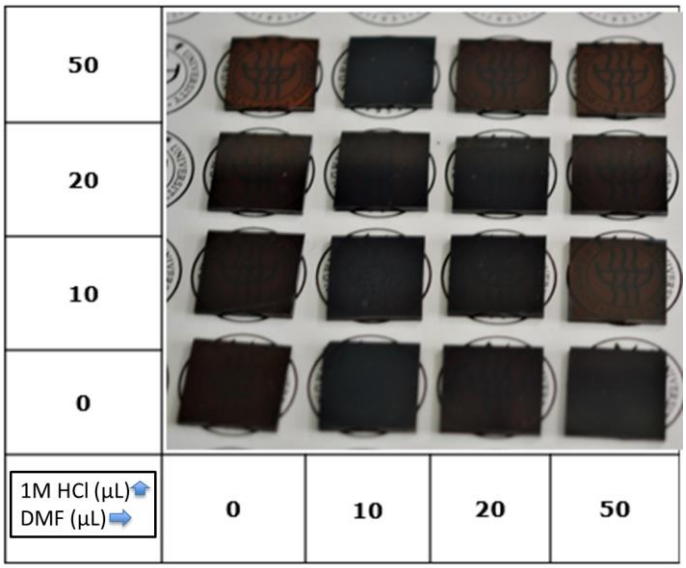

Figure 6-4. Photograph of perovskite films on FTO with varying amounts of additive in the MAI/IPA precursor solution.

For the rest of the work, we continued with the 90 second loading time of the MAI/IPA precursor solution. Figure 6.4 shows a photograph of the effect of varying the different additives for a 90 second loading time. The films produced with 10 µL of DMF in the precursor solution are visually the most dense and dark films, which was also demonstrated in PL, owing to the complete conversion of $MAPbI_3$ perovskite film. XRD data (Figure 6.5) demonstrated that in each case, the conversion of PbI_2 to the perovskite crystal increased with increasing 1M HCl, reaching optimal conversion with 50 µL 1 M HCl added to the MAI/IPA perovskite precursor solution.

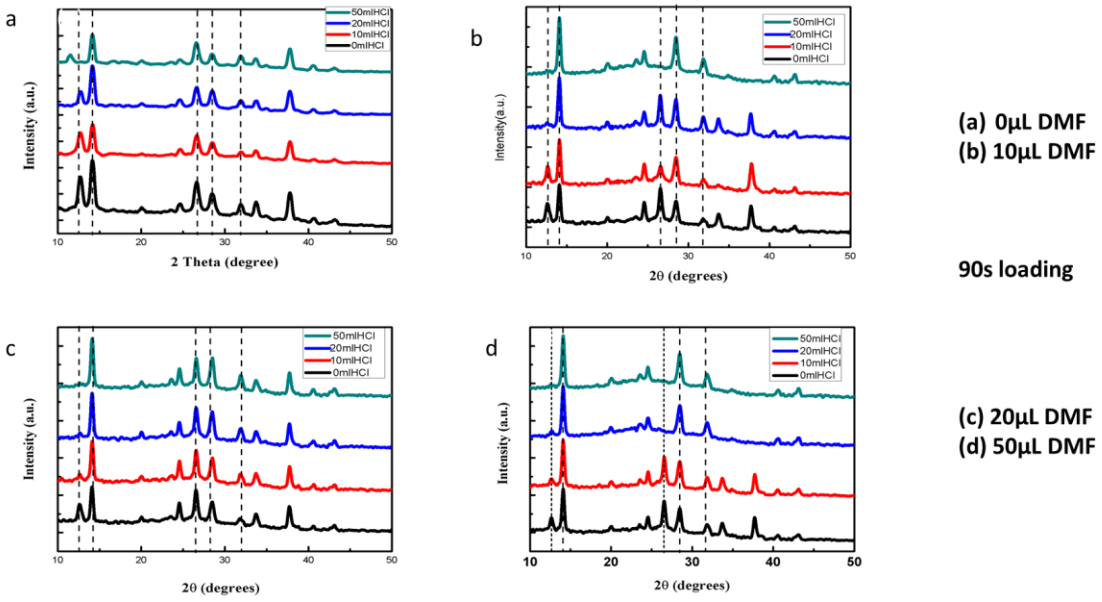

Figure 6-5 . Diffraction pattern of perovskite films on FTO with varying amounts of additive and a 90 second load time. (a) 0 µL DMF, (a) 0 µL DMF, (a) 0 µL DMF, and (a) 0 µL DMF. Black 0 µL 1M HCl, Red 10 µL 1M HCl, Blue 20 µL 1M HCl, and Green 50 µL 1M HCl.

A similar result was observed in the absorption spectra, except in the case where no DMF was added to the precursor solution. It is speculated that this occurred because DMF was able create a porous network, similar to the porous network observed in Chapter 2, for the MAI/IPA with HCl to completely infiltrate the PbI_2 layer. The ideal solution as observed by the photographs, UV-Vis and XRD is the MAI/IPA precursor solution containing 10 µL of DMF and 50 µL of 1 M HCl.

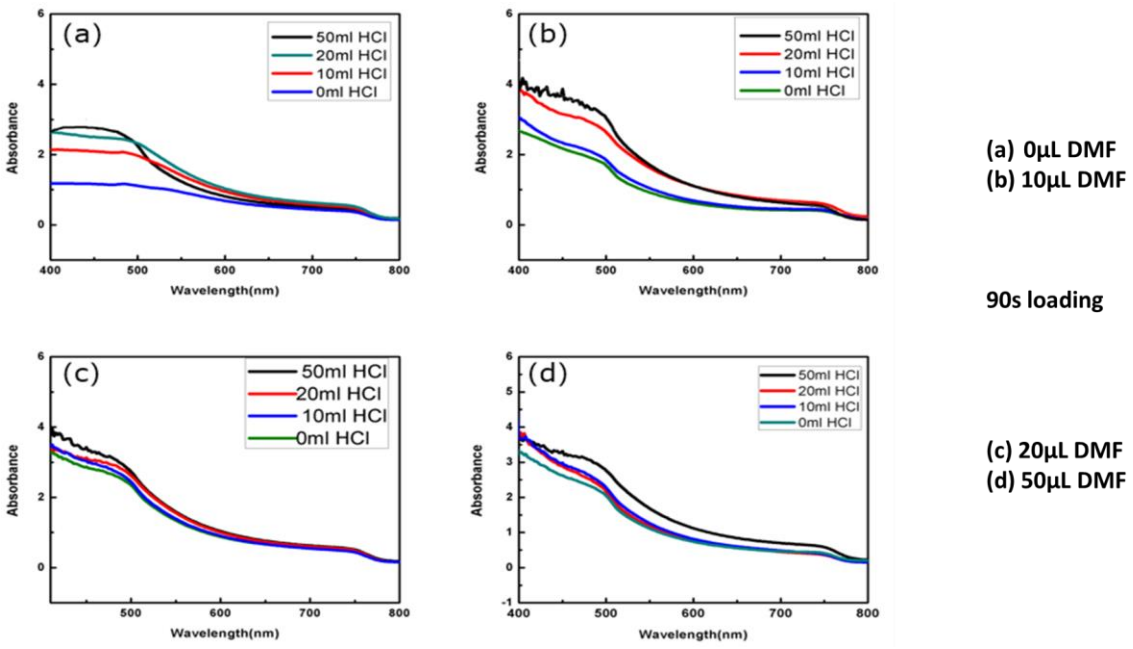

Figure 6-6. UV-Vis absorption spectra of perovskite films on FTO with varying amounts of additive and a 90 second load time. (a) 0 µL DMF, (a) 0 µL DMF, (a) 0 µL DMF, and (a) 0 µL DMF. Green 0 µL 1M HCl, Blue 10 µL 1M HCl, Red 20 µL 1M HCl, and Black 50 µL 1M HCl.

6.1.4 Conclusion and future direction

This work demonstrates the possible improvements that can be made to the perovskite film with a simple additive approach. The optimized film condition was observed with a 90 second loading time of the MAI/IPA solution, using 10 µL of DMF and 50 µL of 1 M HCl. The next step for this work is to make devices, and more specifically large area devices. Next, adaptations can be made to transfer this procedure to a roll-to-roll production procedure for large-scale, large-area perovskite solar cells.

REFERENCES

1. Gribbin, John. Hothouse earth: the greenhouse effect & Gaia. Bantam, 1990.

2. Halpin, S. M., and L. L. Grigsby. "The Electric Power Engineering Handbook." (2001).

3. Hoffman, Joe. "Potential Health and Environmental Effects of Hydrofracking in the Williston Basin, Montana." Retrieved February 5 (2012): 2017.

4. Ridlington, Elizabeth, and John Rumpler. "Fracking by the numbers: Key impacts of dirty drilling at the state and national level." Environment America Research & Policy Center 46 (2013).

5. C.G. Schneider, J.M. Banks, M. Tatsutani, C.A.T. Force. The toll from coal: An updated assessment of death and disease from America's dirtiest energy source: Clean Air Task Force; 2010.

6. Progress Toward Sustainable Energy: Global Tracking Framework 2015 Key Findings: World Bank Group, Energy Sector Management Assistance Program, & International Energy Agency; 2015.

7. Primeaux Jr, Walter J. "Some problems with natural monopoly." Antitrust Bull. 24 (1979): 63.

8. Ye, Ze, and Junda Peng. "The research on the AJ effect and the strategy of the power company under dynamic game of incomplete information." Electrical and Control Engineering (ICECE), 2011 International Conference on. IEEE, 2011.

9. Doll, Christopher NH, and Shonali Pachauri. "Estimating rural populations without access to electricity in developing countries through night-time light satellite imagery." Energy Policy 38.10 (2010): 5661-5670.

10. Crabtree, George W., and Nathan S. Lewis. "Solar energy conversion." Physics today 60.3 (2007): 37-42.

11. McEvoy, Augustin Joseph, Luis Castaner, and Tom Markvart. Solar cells: materials, manufacture and operation. Academic Press, 2012.

12. Polman, Albert, et al. "Photovoltaic materials: Present efficiencies and future challenges." Science 352.6283 (2016): aad4424.

13. Noufi, Rommel, and Ken Zweibel. "High-efficiency CdTe and CIGS thin-film solar cells: highlights and challenges." Photovoltaic Energy Conversion,

Conference Record of the 2006 IEEE 4th World Conference on. Vol. 1. IEEE, 2006.

14. Grätzel, Michael. "Dye-sensitized solar cells." Journal of Photochemistry and Photobiology C: Photochemistry Reviews 4.2 (2003): 145-153.

15. Wöhrle, Dieter, and Dieter Meissner. "Organic solar cells." Advanced Materials 3.3 (1991): 129-138.

16. National Renewable Energy Laboratory (NREL), Best Research-Cells Efficiencies Chart. 2018; https://www.nrel.gov/pv/assets/pdfs/pv- efficiencies-07-17-2018.pdf, [Online; accessed Sep-2018].

17. Snaith, Henry J. "Perovskites: the emergence of a new era for low-cost, high-efficiency solar cells." The Journal of Physical Chemistry Letters 4.21 (2013): 3623-3630.

18. Li, Dan, et al. "Recent progress on stability issues of organic–inorganic hybrid lead perovskite-based solar cells." RSC Advances 6.92 (2016): 89356-89366.

19. Frost, Jarvist M., et al. "Atomistic origins of high-performance in hybrid halide perovskite solar cells." Nano letters 14.5 (2014): 2584-2590.

20. Ma, Jie, and Lin-Wang Wang. "Nanoscale charge localization induced by random orientations of organic molecules in hybrid perovskite CH3NH3PbI3." Nano letters 15.1 (2014): 248-253.

21. Sadhanala, Aditya, et al. "Blue-green color tunable solution processable organolead chloride–bromide mixed halide perovskites for optoelectronic applications." Nano letters 15.9 (2015): 6095-6101.

22. Sadhanala, Aditya, et al. "Preparation of single-phase films of $CH_3NH_3Pb(I_{1-x}Br_x)_3$ with sharp optical band edges." The journal of physical chemistry letters 5.15 (2014): 2501-2505.

23. Brandt, Riley E., et al. "Identifying defect-tolerant semiconductors with high minority-carrier lifetimes: beyond hybrid lead halide perovskites." MRS Communications 5.2 (2015): 265-275.

24. Pasquarelli, Robert M., David S. Ginley, and Ryan O'Hayre. "Solution processing of transparent conductors: from flask to film." Chemical Society Reviews 40.11 (2011): 5406-5441.

25. Im, Jeong-Hyeok, Hui-Seon Kim, and Nam-Gyu Park. "Morphology-photovoltaic property correlation in perovskite solar cells: One-step versus two-step deposition of CH3NH3PbI3." Apl Materials 2.8 (2014): 081510.

26. Cui, Jin, et al. "Recent progress in efficient hybrid lead halide perovskite solar cells." Science and technology of advanced materials 16.3 (2015): 036004.

27. DeLuca, Giovanni, et al. "Transparent Quasi-Interdigitated Electrodes for Semitransparent Perovskite Back-Contact Solar Cells." ACS Applied Energy Materials 1.9 (2018): 4473-4478.

28. Tong, Chuan-Jia, et al. "Uncovering the veil of the degradation in perovskite $CH_3NH_3PbI_3$ upon humidity exposure: a first-principles study." The Journal of Physical Chemistry Letters 6.16 (2015): 3289-3295.

29. Yang, Jinli, et al. "Investigation of $CH_3NH_3PbI_3$ degradation rates and mechanisms in controlled humidity environments using in situ techniques." ACS nano 9.2 (2015): 1955-1963.

30. Wu, Bo, et al. "Charge Accumulation and Hysteresis in Perovskite-Based Solar Cells: An Electro-Optical Analysis." Advanced Energy Materials 5.19 (2015): 1500829.

31. Baena, Juan Pablo Correa, et al. "Highly efficient planar perovskite solar cells through band alignment engineering." Energy & Environmental Science 8.10 (2015): 2928-2934.

32. Lim, Kyung-Geun, et al. "Boosting the power conversion efficiency of perovskite solar cells using self-organized polymeric hole extraction layers with high work function." Advanced Materials 26.37 (2014): 6461-6466.

33. Jeng, Jun-Yuan, et al. "Nickel oxide electrode interlayer in CH3NH3PbI3 perovskite/PCBM planar-heterojunction hybrid solar cells." Advanced materials 26.24 (2014): 4107-4113.

34. Jeng, Jun-Yuan, et al. "CH3NH3PbI3 perovskite/fullerene planar-heterojunction hybrid solar cells." Advanced Materials 25.27 (2013): 3727-3732.

35. Abrusci, Agnese, et al. "High-performance perovskite-polymer hybrid solar cells via electronic coupling with fullerene monolayers." Nano letters 13.7 (2013): 3124-3128.

36. Ryu, Seungchan, et al. "Voltage output of efficient perovskite solar cells with high open-circuit voltage and fill factor." Energy & Environmental Science 7.8 (2014): 2614-2618.

37. Zhou, Huanping, et al. "Interface engineering of highly efficient perovskite solar cells." Science 345.6196 (2014): 542-546.

38. Zhang, Hengzhong, and Jillian F. Banfield. "Understanding polymorphic phase transformation behavior during growth of nanocrystalline aggregates: insights from TiO2." The Journal of Physical Chemistry B 104.15 (2000): 3481-3487.

39. Ho, Ching-Yuan, et al. "Investigation of post-annealing indium tin oxide for future electro-optical device application." Proceedings of the 10th WSEAS international conference on Telecommunications and informatics and microelectronics, nanoelectronics, optoelectronics, and WSEAS international conference on Signal processing. World Scientific and Engineering Academy and Society (WSEAS), 2011.

40. Kwak, Dong-Joo, et al. "Comparison of transparent conductive indium tin oxide, titanium-doped indium oxide, and fluorine-doped tin oxide films for dye-sensitized solar cell application." Journal of Electrical Engineering and Technology 6.5 (2011): 684-687.

41. Hsu, Shao-Hui, et al. "Platinum-free counter electrode comprised of metal-organic-framework (MOF)-derived cobalt sulfide nanoparticles for efficient dye-sensitized solar cells (DSSCs)." Scientific reports 4 (2014): 6983.

42. Yin, Wan-Jian, et al. "Halide perovskite materials for solar cells: a theoretical review." Journal of Materials Chemistry A 3.17 (2015): 8926-8942.

43. Li, Chonghea, et al. "Formability of ABX_3 (X= F, Cl, Br, I) Halide Perovskites." Acta Crystallographica Section B: Structural Science 64.6 (2008): 702-707.

44. Baikie, Tom, et al. "Synthesis and crystal chemistry of the hybrid perovskite (CH_3NH_3) PbI_3 for solid-state sensitized solar cell applications." Journal of Materials Chemistry A 1.18 (2013): 5628-5641.

45. Stoumpos, Constantinos C., Christos D. Malliakas, and Mercouri G. Kanatzidis. "Semiconducting tin and lead iodide perovskites with organic cations: phase transitions, high mobilities, and near-infrared photoluminescent properties." Inorganic chemistry 52.15 (2013): 9019-9038.

46. D'Innocenzo, Valerio, et al. "Excitons versus free charges in organo-lead tri-halide perovskites." Nature communications 5 (2014): 3586.

47. Yang, Woon Seok, et al. "High-performance photovoltaic perovskite layers fabricated through intramolecular exchange." Science 348.6240 (2015): 1234-1237.

48. Kim, Hui-Seon, et al. "Lead iodide perovskite sensitized all-solid-state submicron thin film mesoscopic solar cell with efficiency exceeding 9%." Scientific reports 2 (2012): 591.

49. Liu, Mingzhen, Michael B. Johnston, and Henry J. Snaith. "Efficient planar heterojunction perovskite solar cells by vapor deposition." Nature 501.7467 (2013): 395.

50. Lee, Michael M., et al. "Efficient hybrid solar cells based on meso-superstructured organometal halide perovskites." Science (2012): 1228604.

51. Kojima, Akihiro, et al. "Organometal halide perovskites as visible-light sensitizers for photovoltaic cells." Journal of the American Chemical Society 131.17 (2009): 6050-6051.

52. Saliba, Michael, et al. "Cesium-containing triple cation perovskite solar cells: improved stability, reproducibility and high efficiency." Energy & environmental science 9.6 (2016): 1989-1997.

53. Wang, Yuan-qiang, et al. "A facile in situ synthesis route for $CuInS_2$ quantum-dots/In_2S_3 co-sensitized photoanodes with high photoelectric performance." ACS applied materials & interfaces 5.22 (2013): 11858-11864.

54. Rui, Yichuan, et al. "Size-tunable TiO_2 nanorod microspheres synthesized via a one-pot solvothermal method and used as the scattering layer for dye-sensitized solar cells." Nanoscale 5.24 (2013): 12574-12581.

55. Ko, Hyun-Seok, Jin-Wook Lee, and Nam-Gyu Park. "15.76% efficiency perovskite solar cells prepared under high relative humidity: importance of PbI_2 morphology in two-step deposition of $CH_3NH_3PbI_3$." Journal of Materials Chemistry A 3.16 (2015): 8808-8815.

56. Gangishetty, Mahesh K., Robert WJ Scott, and Timothy L. Kelly. "Effect of relative humidity on crystal growth, device performance and hysteresis in planar heterojunction perovskite solar cells." Nanoscale 8.12 (2016): 6300-6307.

57. Yang, Jinli, et al. "Investigation of $CH_3NH_3PbI_3$ degradation rates and mechanisms in controlled humidity environments using in situ techniques." ACS nano 9.2 (2015): 1955-1963.

58. Gangishetty, Mahesh K., Robert WJ Scott, and Timothy L. Kelly. "Effect of relative humidity on crystal growth, device performance and hysteresis in planar heterojunction perovskite solar cells." Nanoscale 8.12 (2016): 6300-6307.

59. You, Jingbi, et al. "Moisture assisted perovskite film growth for high performance solar cells." Applied Physics Letters 105.18 (2014): 183902.

60. Xiao, Zhengguo, et al. "Solvent annealing of perovskite-induced crystal growth for photovoltaic-device efficiency enhancement." Advanced Materials 26.37 (2014): 6503-6509.

61. Liu, Jiang, et al. "Improved crystallization of perovskite films by optimized solvent annealing for high efficiency solar cell." ACS applied materials & interfaces 7.43 (2015): 24008-24015.

62. Wu, Yongzhen, et al. "Retarding the crystallization of PbI_2 for highly reproducible planar-structured perovskite solar cells via sequential deposition." Energy & Environmental Science 7.9 (2014): 2934-2938.

63. Zhang, Yi, et al. "PbI_2–HMPA complex pretreatment for highly reproducible and efficient $CH_3NH_3PbI_3$ perovskite solar cells." Journal of the American Chemical Society 138.43 (2016): 14380-14387.

64. Liu, Tanghao, et al. "Mesoporous PbI_2 scaffold for high-performance planar heterojunction perovskite solar cells." Advanced Energy Materials 6.3 (2016): 1501890.

65. Burschka, Julian, et al. "Sequential deposition as a route to high-performance perovskite-sensitized solar cells." Nature 499.7458 (2013): 316.

66. Im, Jeong-Hyeok, et al. "Growth of $CH_3NH_3PbI_3$ cuboids with controlled size for high-efficiency perovskite solar cells." Nature nanotechnology 9.11 (2014): 927-932.

67. Wu, Yongzhen, et al. "Retarding the crystallization of PbI_2 for highly reproducible planar-structured perovskite solar cells via sequential deposition." Energy & Environmental Science 7.9 (2014): 2934-2938.

68. Liang, Po-Wei, et al. "Additive enhanced crystallization of solution-processed perovskite for highly efficient planar-heterojunction solar cells." Advanced materials 26.22 (2014): 3748-3754.

69. Tashiro, Kohji, Sono Sasaki, and Masamichi Kobayashi. "Structural investigation of orthorhombic-to-hexagonal phase transition in polyethylene crystal: the experimental confirmation of the conformationally disordered structure by X-ray diffraction and infrared/Raman spectroscopic measurements." Macromolecules 29.23 (1996): 7460-7469.

70. Ran, Shaofeng, et al. "Novel image analysis of two-dimensional X-ray fiber diffraction patterns: example of a polypropylene fiber drawing study." Journal of applied crystallography 33.4 (2000): 1031-1036.

71. Kory, Max J., et al. "Gram-scale synthesis of two-dimensional polymer crystals and their structure analysis by X-ray diffraction." Nature chemistry 6.9 (2014): 779.

72. Brezesinski, Torsten, et al. "Ordered mesoporous α-MoO_3 with iso-oriented nanocrystalline walls for thin-film pseudocapacitors." Nature materials 9.2 (2010): 146.

73. Li, Wenzhe, et al. "Controllable grain morphology of perovskite absorber film by molecular self-assembly toward efficient solar cell exceeding 17%." Journal of the American Chemical Society 137.32 (2015): 10399-10405.

74. Baibarac, M., et al. "On the optical properties of micro-and nanometric size PbI_2 particles." Journal of Physics: Condensed Matter 16.13 (2004): 2345.

75. Lee, Sangchul, Joshua Feldman, and Stephanie S. Lee. "Nanoconfined Crystallization of $MAPbI_3$ to Probe Crystal Evolution and Stability." Crystal Growth & Design 16.8 (2016): 4744-4751.

76. Oku, Takeo. "Crystal structures of $CH_3NH_3PbI_3$ and related perovskite compounds used for solar cells." Solar Cells-New Approaches and Reviews. InTech, 2015.

77. Kumar, Y., et al. "Effect of heat treatment on the electrical properties of perovskite solar cells." Solar Energy Materials and Solar Cells 157 (2016): 10-17.

78. Zhang, Zhirong, et al. "High reproducibility of perovskite solar cells via a complete spin-coating sequential solution deposition process." Solar Energy 122 (2015): 97-103.

79. Yamada, Yasuhiro, et al. "Spontaneous defect annihilation in $CH_3NH_3PbI_3$ thin films at room temperature revealed by time-resolved photoluminescence spectroscopy." The journal of physical chemistry letters 6.3 (2015): 482-486.

80. Jacobsson, T. Jesper, et al. "Unreacted PbI_2 as a double-edged sword for enhancing the performance of perovskite solar cells." Journal of the American Chemical Society 138.32 (2016): 10331-10343.

81. Mali, Sawanta S., et al. "In situ processed gold nanoparticle-embedded TiO_2 nanofibers enabling plasmonic perovskite solar cells to exceed 14% conversion efficiency." Nanoscale 8.5 (2016): 2664-2677.

82. de Quilettes, Dane W., et al. "Impact of microstructure on local carrier lifetime in perovskite solar cells." Science 348.6235 (2015): 683-686.

83. Tress, Wolfgang, et al. "Understanding the rate-dependent J–V hysteresis, slow time component, and aging in $CH_3NH_3PbI_3$ perovskite solar cells: the role of a compensated electric field." Energy & Environmental Science 8.3 (2015): 995-1004.

84. Sun, Chen, et al. "Amino-Functionalized Conjugated Polymer as an Efficient Electron Transport Layer for High-Performance Planar-Heterojunction Perovskite Solar Cells." Advanced Energy Materials 6.5 (2016): 1501534.

85. Xiao, Manda, et al. "A fast deposition-crystallization procedure for highly efficient lead iodide perovskite thin-film solar cells." Angewandte Chemie International Edition 53.37 (2014): 9898-9903.

86. Pecchia, Alessandro, et al. "Role of ferroelectric nanodomains in the transport properties of perovskite solar cells." Nano letters 16.2 (2016): 988-992.

87. Li, Guijun, et al. "Identifying the Optimum Morphology in High-Performance Perovskite Solar Cells." Advanced Energy Materials 5.9 (2015): 1401775.

88. Price, Michael B., et al. "Hot-carrier cooling and photoinduced refractive index changes in organic–inorganic lead halide perovskites." Nature communications 6 (2015): 8420.

89. Yang, Woon Seok, et al. "Iodide management in formamidinium-lead-halide–based perovskite layers for efficient solar cells." Science 356.6345 (2017): 1376-1379.

90. De Wolf, Stefaan, et al. "Organometallic halide perovskites: sharp optical absorption edge and its relation to photovoltaic performance." The journal of physical chemistry letters 5.6 (2014): 1035-1039.

91. Niu, Shanyuan, et al. "Bandgap control via structural and chemical tuning of transition metal perovskite chalcogenides." Advanced Materials 29.9 (2017): 1604733.

92. Yusoff, Abd Rashid bin Mohd, et al. "Ambipolar triple cation perovskite field effect transistors and inverters." Advanced Materials 29.8 (2017): 1602940.

93. Chen, Tianran, et al. "Origin of long lifetime of band-edge charge carriers in organic–inorganic lead iodide perovskites." Proceedings of the National Academy of Sciences 114.29 (2017): 7519-7524.

94. Jeon, Nam Joong, et al. "Solvent engineering for high-performance inorganic–organic hybrid perovskite solar cells." Nature materials 13.9 (2014): 897.

95. Back, Hyungcheol, et al. "Interfacial modification of hole transport layers for efficient large-area perovskite solar cells achieved via blade-coating." Solar Energy Materials and Solar Cells 144 (2016): 309-315.

96. Ciro, John, Mario Alejandro Mejía-Escobar, and Franklin Jaramillo. "Slot-die processing of flexible perovskite solar cells in ambient conditions." Solar Energy 150 (2017): 570-576.

97. Mathies, Florian, et al. "Multipass inkjet printed planar methylammonium lead iodide perovskite solar cells." Journal of Materials Chemistry A 4.48 (2016): 19207-19213.

98. Zhou, Huanping, et al. "Interface engineering of highly efficient perovskite solar cells." Science 345.6196 (2014): 542-546.

99. Xie, Li-Qiang, et al. "Understanding the cubic phase stabilization and crystallization kinetics in mixed cations and halides perovskite single crystals." Journal of the American Chemical Society 139.9 (2017): 3320-3323.

100. Li, Wenzhe, et al. "Enhanced UV-light stability of planar heterojunction perovskite solar cells with caesium bromide interface modification." Energy & Environmental Science 9.2 (2016): 490-498.

101. Wang, Jacob Tse-Wei, et al. "Efficient perovskite solar cells by metal ion doping." Energy & Environmental Science 9.9 (2016): 2892-2901.

102. Saliba, Michael, et al. "Incorporation of rubidium cations into perovskite solar cells improves photovoltaic performance." Science 354.6309 (2016): 206-209.

103. Kaltenbrunner, Martin, et al. "Flexible high power-per-weight perovskite solar cells with chromium oxide–metal contacts for improved stability in air." Nature materials 14.10 (2015): 1032.

104. Li, Xiong, et al. "Improved performance and stability of perovskite solar cells by crystal crosslinking with alkylphosphonic acid ω-ammonium chlorides." Nature chemistry 7.9 (2015): 703-711.

105. Xiong, Hao, et al. "Hydrophobic coating over a $CH_3NH_3PbI_3$ absorbing layer towards air stable perovskite solar cells." Journal of Materials Chemistry C 4.28 (2016): 6848-6854.

106. Zhao, Yicheng, et al. "A polymer scaffold for self-healing perovskite solar cells." Nature communications 7 (2016): 10228.

107. Wang, Feng, et al. "Phenylalkylamine Passivation of Organolead Halide Perovskites Enabling High-Efficiency and Air-Stable Photovoltaic Cells." Advanced Materials 28.45 (2016): 9986-9992.

108. Huang, Zengqi, et al. "Nucleation and Crystallization Control via Polyurethane to Enhance the Bendability of Perovskite Solar Cells with Excellent Device Performance." Advanced Functional Materials 27.41 (2017): 1703061.

109. Manshor, Nurul Ain, et al. "Humidity versus photo-stability of metal halide perovskite films in a polymer matrix." Physical Chemistry Chemical Physics 18.31 (2016): 21629-21639.

110. Guo, Yunlong, et al. "Polymer stabilization of lead (II) perovskite cubic nanocrystals for semitransparent solar cells." Advanced Energy Materials 6.6 (2016): 1502317.

111. Chaudhary, Bhumika, et al. "Poly (4-Vinylpyridine)-Based Interfacial Passivation to Enhance Voltage and Moisture Stability of Lead Halide Perovskite Solar Cells." ChemSusChem 10.11 (2017): 2473-2479.

112. Di Giacomo, Francesco, et al. "Progress, challenges and perspectives in flexible perovskite solar cells." Energy & Environmental Science 9.10 (2016): 3007-3035.

113. Banerjee, A. N., et al. "Poole–Frenkel effect in nanocrystalline SnO_2: F thin films prepared by a sol–gel dip-coating technique." physica status solidi (a) 201.5 (2004): 983-989.

114. Nie, Wanyi, et al. "High-efficiency solution-processed perovskite solar cells with millimeter-scale grains." Science 347.6221 (2015): 522-525.

115. Frost, Jarvist M., et al. "Atomistic origins of high-performance in hybrid halide perovskite solar cells." Nano letters 14.5 (2014): 2584-2590.

116. Perry, Anthony J., Václav Valvoda, and David Rafaja. "X-ray residual stress measurement in TiN, ZrN and HfN films using the Seemann-Bohlin method." Thin Solid Films 214.2 (1992): 169-174.

117. Huang, Jianxi, et al. "An infrared spectroscopy study of PES PVP blend and PES-g-PVP copolymer." Polymer Testing 59 (2017): 212-219.

118. Liu, Shilin, Wen Zeng, and Ting Chen. "Synthesis of hierarchical flower-like NiO and the influence of surfactant." Physica E: Low-dimensional Systems and Nanostructures 85 (2017): 13-18.

119. Gao, B., et al. "Poly (acrylamide-co-acrylic acid)/Poly (vinyl pyrrolidone) Polymer Blends Prepared by Dispersion Polymerization." Journal of Macromolecular Science®, Part B: Physics 47.3 (2008): 544-554.

120. Tripathi, Brijesh, et al. "Temperature induced structural, electrical and optical changes in solution processed perovskite material: Application in photovoltaics." Solar Energy Materials and Solar Cells 132 (2015): 615-622.

121. Qiu, Jianhang, et al. "All-solid-state hybrid solar cells based on a new organometal halide perovskite sensitizer and one-dimensional TiO_2 nanowire arrays." Nanoscale 5.8 (2013): 3245-3248.

122. Lindblad, Rebecka, et al. "Electronic structure of $CH_3NH_3PbX_3$ perovskites: dependence on the halide moiety." The Journal of Physical Chemistry C 119.4 (2015): 1818-1825.

123. Dong, Qingshun, et al. "Energetically favored formation of SnO_2 nanocrystals as electron transfer layer in perovskite solar cells with high efficiency exceeding 19%." Nano Energy 40 (2017): 336-344.

124. Ryu, Seungchan, et al. "Voltage output of efficient perovskite solar cells with high open-circuit voltage and fill factor." Energy & Environmental Science 7.8 (2014): 2614-2618.

125. Busacca, C., et al. "Electrochemical performance investigation of electrospun urchin-like V_2O_3-CNF composite nanostructure for vanadium redox flow battery." Electrochimica Acta 230 (2017): 174-180.

126. Kim, Young Chan, et al. "Beneficial effects of PbI_2 incorporated in organo-lead halide perovskite solar cells." Advanced Energy Materials 6.4 (2016): 1502104.

127. Cho, Kyung Taek, et al. "Highly efficient perovskite solar cells with a compositionally engineered perovskite/hole transporting material interface." Energy & Environmental Science 10.2 (2017): 621-627.

128. Liu, Qin, et al. "Enhanced Stability of Perovskite Solar Cells with Low-Temperature Hydrothermally Grown SnO_2 Electron Transport Layers." Advanced Functional Materials 26.33 (2016): 6069-6075.

129. Jiang, Qi, et al. "Enhanced electron extraction using SnO_2 for high-efficiency planar-structure $HC(NH_2)_2PbI_3$-based perovskite solar cells." Nature Energy 2.1 (2017): 16177.

130. Alsari, Mejd, et al. "Degradation Kinetics of Inverted Perovskite Solar Cells." Scientific reports 8.1 (2018): 5977.

131. Im, Jeong-Hyeok, et al. "Growth of $CH_3NH_3PbI_3$ cuboids with controlled size for high-efficiency perovskite solar cells." Nature nanotechnology 9.11 (2014): 927-932.

132. Wu, Xiaoxi, et al. "Trap states in lead iodide perovskites." Journal of the American Chemical Society 137.5 (2015): 2089-2096.

133. Fakharuddin, Azhar, et al. "Vertical TiO_2 nanorods as a medium for stable and high-efficiency perovskite solar modules." ACS nano 9.8 (2015): 8420-8429.

134. Ryu, UnJin, et al. "Nanocrystalline Titanium Metal–Organic Frameworks for Highly Efficient and Flexible Perovskite Solar Cells." ACS nano 12.5 (2018): 4968-4975.

135. Yoshikawa, Kunta, et al. "Silicon heterojunction solar cell with interdigitated back contacts for a photoconversion efficiency over 26%." Nature Energy 2.5 (2017): 17032.

136. Adhyaksa, Gede WP, Eric Johlin, and Erik C. Garnett. "Nanoscale back contact perovskite solar cell design for improved tandem efficiency." Nano letters 17.9 (2017): 5206-5212.

137. Xiong, Hao, et al. "Solvent vapor annealing of oriented PbI_2 films for improved crystallization of perovskite films in the air." Solar Energy Materials and Solar Cells 166 (2017): 167-175.

138. Jumabekov, A. N., et al. "Back-contacted hybrid organic–inorganic perovskite solar cells." Journal of Materials Chemistry C 4.15 (2016): 3125-3130.

139. Lu, Guilin, et al. "Development of back-junction back-contact silicon solar cells based on industrial processes." Progress in Photovoltaics: Research and Applications 25.6 (2017): 441-451.

140. Hartnagel, Hans, et al. Semiconducting transparent thin films. Bristol: Institute of Physics, 1995.

141. Li, Xiong, et al. "Improved performance and stability of perovskite solar cells by crystal crosslinking with alkylphosphonic acid ω-ammonium chlorides." Nature chemistry 7.9 (2015): 703-711.

142. Lu, Jianfeng, et al. "Diammonium and Monoammonium Mixed-Organic-Cation Perovskites for High Performance Solar Cells with Improved Stability." Advanced Energy Materials 7.18 (2017): 1700444.

143. Saliba, Michael, et al. "Cesium-containing triple cation perovskite solar cells: improved stability, reproducibility and high efficiency." Energy & environmental science 9.6 (2016): 1989-1997.

144. Löper, Philipp, et al. "Complex refractive index spectra of $CH_3NH_3PbI_3$ perovskite thin films determined by spectroscopic ellipsometry and spectrophotometry." The journal of physical chemistry letters 6.1 (2014): 66-71.

145. Holman, Zachary C., et al. "Infrared light management in high-efficiency silicon heterojunction and rear-passivated solar cells." Journal of Applied Physics 113.1 (2013): 013107.

146. Ball, James M., et al. "Optical properties and limiting photocurrent of thin-film perovskite solar cells." Energy & Environmental Science 8.2 (2015): 602-609.

147. Perevalov, Timofei Viktorovich, et al. "Electronic structure of α-Al_2O_3: Ab initio simulations and comparison with experiment." JETP Letters 85.3 (2007): 165-168.

148. Enright, Brendan, and Donald Fitzmaurice. "Spectroscopic determination of electron and hole effective masses in a nanocrystalline semiconductor film." The Journal of Physical Chemistry 100.3 (1996): 1027-1035.

149. Helander, M. G., et al. "Chlorinated indium tin oxide electrodes with high work function for organic device compatibility." Science 332.6032 (2011): 944-947.

150. Yan, L. T., and R. E. I. Schropp. "Changes in the structural and electrical properties of vacuum post-annealed tungsten-and titanium-doped indium oxide films deposited by radio frequency magnetron sputtering." Thin Solid Films 520.6 (2012): 2096-2101.

151. Gupta, R. K., et al. "High mobility W-doped In_2O_3 thin films: Effect of growth temperature and oxygen pressure on structural, electrical and optical properties." Applied Surface Science 254.6 (2008): 1661-1665.

152. Calado, Philip, et al. "Evidence for ion migration in hybrid perovskite solar cells with minimal hysteresis." Nature communications 7 (2016): 13831.

153. Roldan-Carmona, Cristina, et al. "High efficiency single-junction semitransparent perovskite solar cells." Energy & Environmental Science 7.9 (2014): 2968-2973.

154. Della Gaspera, Enrico, et al. "Ultra-thin high efficiency semitransparent perovskite solar cells." Nano Energy 13 (2015): 249-257.

155. Brongersma, Mark L., Yi Cui, and Shanhui Fan. "Light management for photovoltaics using high-index nanostructures." Nature materials 13.5 (2014): 451.

156. Chen, Chun-Chao, et al. "High-performance semi-transparent polymer solar cells possessing tandem structures." Energy & Environmental Science 6.9 (2013): 2714-2720.

157. Knight, Mark W., et al. "Soft imprinted Ag nanowire hybrid electrodes on silicon heterojunction solar cells." Nano Energy 30 (2016): 398-406.

158. Hartnagel, Hans, et al. “Semiconducting transparent thin films.” Bristol: Institute of Physics, 1995.

159. Choi, K. H., et al. "ITO/Ag/ITO multilayer films for the application of a very low resistance transparent electrode." Thin solid films 341.1-2 (1999): 152-155.

160. Kido, Junji, Masato Kimura, and Katsutoshi Nagai. "Multilayer white light-emitting organic electroluminescent device." Science 267.5202 (1995): 1332-1334.

161. Shen, Zilan, et al. "Three-color, tunable, organic light-emitting devices." Science 276.5321 (1997): 2009-2011.

162. Friend, R. H., et al. "Electroluminescence in conjugated polymers." Nature 397.6715 (1999): 121.

163. Baldo, M. A., M. E. Thompson, and S. R. Forrest. "High-efficiency fluorescent organic light-emitting devices using a phosphorescent sensitizer." Nature 403.6771 (2000): 750.

164. Müller, C. David, et al. "Multi-colour organic light-emitting displays by solution processing." Nature 421.6925 (2003): 829.

165. Sun, Yiru, et al. "Management of singlet and triplet excitons for efficient white organic light-emitting devices." Nature 440.7086 (2006): 908.

166. Reineke, Sebastian, et al. "White organic light-emitting diodes with fluorescent tube efficiency." Nature 459.7244 (2009): 234.

167. Sun, Yiru, and Stephen R. Forrest. "Enhanced light out-coupling of organic light-emitting devices using embedded low-index grids." Nature photonics 2.8 (2008): 483.

168. Sekitani, Tsuyoshi, et al. "Stretchable active-matrix organic light-emitting diode display using printable elastic conductors." Nature materials 8.6 (2009): 494.

169. Koo, Won Hoe, et al. "Light extraction from organic light-emitting diodes enhanced by spontaneously formed buckles." Nature Photonics 4.4 (2010): 222.

170. Liu, Wei-Sheng, et al. "Indium tin oxide with titanium doping for transparent conductive film application on CIGS solar cells." Applied Surface Science 354 (2015): 31-35.

171. Exarhos, Gregory J., and Xiao-Dong Zhou. "Discovery-based design of transparent conducting oxide films." Thin solid films 515.18 (2007): 7025-7052.

172. Irwin, Michael D., et al. "p-Type semiconducting nickel oxide as an efficiency-enhancing anode interfacial layer in polymer bulk-heterojunction solar cells." Proceedings of the National Academy of Sciences 105.8 (2008): 2783-2787.

173. Minami, Tadatsugu, et al. "Transparent conducting zinc-co-doped ITO films prepared by magnetron sputtering." Thin Solid Films 373.1-2 (2000): 189-194.

174. Ali, H. M. "Characterization of a new transparent-conducting material of ZnO doped ITO thin films." physica status solidi (a) 202.14 (2005): 2742-2752.

175. Mishra, Satyendra K., Samta Rani, and Banshi D. Gupta. "Surface plasmon resonance based fiber optic hydrogen sulphide gas sensor utilizing nickel oxide doped ITO thin film." Sensors and Actuators B: Chemical 195 (2014): 215-222.

176. Kang, Y. M., et al. "Properties of Ce-doped ITO films deposited on polymer substrate by DC magnetron sputtering." Thin Solid Films 518.11 (2010): 3081-3084.

177. Nakasa, Akihiko, et al. "Fabrication of nickel oxide and Ni-doped indium tin oxide thin films using pyrosol process." Thin Solid Films 498.1-2 (2006): 240-243.

178. Kim, J. C., et al. "Investigation of conductive and transparent ITO/Ni/ITO multilayer films deposited by a magnetron sputter process." Nuclear Instruments and Methods in Physics Research Section B: Beam Interactions with Materials and Atoms 268.2 (2010): 131-134.

179. Caricato, A. P., et al. "Electrical and optical properties of ITO and ITO/Cr-doped ITO films." Applied Physics A 101.4 (2010): 753-758.

180. Wu, Wu-Qiang, et al. "Molecular doping enabled scalable blading of efficient hole-transport-layer-free perovskite solar cells." Nature communications 9.1 (2018): 1625.

181. Fan, Lin, et al. "Elucidating the role of chlorine in perovskite solar cells." Journal of Materials Chemistry A 5.16 (2017): 7423-7432.

182. Chen, Qi, et al. "The optoelectronic role of chlorine in CH 3 NH 3 PbI 3 (Cl)-based perovskite solar cells." Nature communications 6 (2015): 7269.

183. Yu, Hui, et al. "The Role of Chlorine in the Formation Process of “CH3NH3PbI3-xClx” Perovskite." Advanced Functional Materials 24.45 (2014): 7102-7108.

184. Oku, Takeo, Kohei Suzuki, and Atsushi Suzuki. "Effects of chlorine addition to perovskite-type CH3NH3PbI3 photovoltaic devices." Journal of the Ceramic Society of Japan 124.3 (2016): 234-238.

185. Quarti, Claudio, et al. "Chlorine incorporation in the CH3NH3PbI3 perovskite: small concentration, big effect." Inorganic chemistry 56.1 (2016): 74-83.